FAKULTÄT FÜR BAUINGENIEUR-
UND VERMESSUNGSWESEN

Precise GNSS Clock-Estimation for Real-Time Navigation and Precise Point Positioning

Dissertation
von

André Hauschild

TECHNISCHE UNIVERSITÄT
MÜNCHEN

Technische Universität München

Institut für Astronomische und Physikalische Geodäsie

Precise GNSS Clock-Estimation for Real-Time Navigation and Precise Point Positioning

André Hauschild

Vollständiger Abdruck der von der Fakultät für Bauingenieur- und Vermessungswesen der Technischen Universität München zur Erlangung des akademischen Grades eines

Doktor – Ingenieurs

genehmigten Dissertation.

Vorsitzender:		Univ.-Prof. Dr.-Ing. U. Stilla
Prüfer der Dissertation:	1.	Univ.-Prof. Dr. phil. nat. U. Hugentobler
	2.	Priv.-Doz. Dr. rer. nat. habil. O. Montenbruck
	3.	Prof. Dr. R. B. Langley University of New Brunswick, Kanada

Die Dissertation wurde am 27.04.2010 bei der Technischen Universität München eingereicht und durch die Fakultät für Bauingenieur- und Vermessungswesen am 28.06.2010 angenommen.

Summary

In this dissertation, a complete system for GNSS clock offset estimation in real-time has been developed and implemented. The thesis begins with an overview of the atomic standards on board of GNSS satellites. A brief review of the historic GPS satellites is followed by a more detailed summary of the currently active satellites. The clock performance is analyzed and compared among the different clock types and an outlook is provided to future satellites.

The real-time network, which provides the measurements for the real-time clock estimation, is presented. The existing techniques for real-time dissemination of GNSS measurements are introduced with a short overview and discussion of existing data formats. Next, the stations selected for processing are introduced and the measurement performance is characterized. An overview of the COoperative Network for Giove Observations (CONGO) is provided, which is the first receiver network for global observations of the GIOVE satellites.

The REal-TIme CLock Estimation (RETICLE) system, which has been developed in the course of this thesis, is introduced in the next chapter. A general overview of the system, is followed by the description of the models used for GPS and GIOVE observations and the design of the Kalman filter, which is the core algorithm of the system. The solution for satellite clock jump detection and mitigation is described. Finally, the effect of orbit errors on the clock estimation is analyzed and mitigation methods are described.

The analysis section starts with orbit determination results obtained with real flight data from the TerraSAR-X satellite in simulated near real-time orbit determination scenarios. The orbit accuracies for a reduced-dynamics and a kinematic orbit determination are shown. A real-time capable navigation algorithm is also analyzed to demonstrate the potential performance if the RETICLE clock estimates would be broadcast via geostationary relay satellites for on-board use.

An overview of the IGS real-time pilot project is presented in the following chapter. The RETICLE clocks have been submitted as a contribution to the project for more than a year. The statistics derived by the analysis center coordinator from orbit and clock comparisons with respect to the IGS Rapid product are presented.

Results for the GIOVE real-time clock estimation are presented. The chapter briefly introduces the real-time processing of the observations from the dedicated GIOVE tracking network and the generation of the combined GPS/GIOVE orbit and clock product. The quality of the GIOVE real-time clocks is analyzed and results for single-point-positioning and precise point positioning with GPS and GIOVE are shown for a selected test case.

Contents

1. Introduction

1.1 Overview and Problem Statement

The Global Positioning System has been the most widely used satellite navigation system for decades. The range of applications is manifold and reaches far beyond navigation and time transfer, which have been the original purposes of the system. Many scientific applications of GPS require precise orbit and clock offset information. One specific example, which will be discussed in further detail in this dissertation, is the precise orbit determination (POD) of satellites in low Earth orbit (LEO). A growing number of satellite missions requires the satellite orbit to be determined shortly after the ground station pass, because it is the foundation for consequent data analysis of the satellite's payload. The observations of the LEO satellite's GPS receiver are available shortly after the data dump to the ground station, but for positioning with these data, precise orbit and clock data of the complete GPS constellation is also required with the same low latency. Predictions of clock offset and drift, which are provided for example in the predicted part of the IGS ultra-rapid orbits or the broadcast ephemerides, deviate quickly from the true values by several decimeters or even meters. This degradation is due to the fact that rubidium and cesium atomic standards of the GPS satellites are subject to clock noise and frequency variations, which can originate from a variety of effects and are hard to forecast. Thus, products with extrapolated clocks become unusable for precise point positioning (PPP) applications, when a carrier-phase-based positioning accuracy down to centimeter level is desired. The solution to this problem is the use of clock offsets, which have been estimated in (near-) real-time from GPS measurements originating from a network of sensor stations. These sensor stations are connected to the internet and disseminate their measurements to the users in real-time, typically with a latency of only 2-3 seconds. Enabled by the growing availability of broadband internet connections, the reception of data from a global network of about 30-40 stations can be easily accomplished.

To fulfill the needs of the LEO-POD applications, the following main requirements must be met by the real-time clock product:

- contain globally valid orbits and clocks for all healthy satellites
- follow short term characteristics of the different atomic standards
- meet latency for processing of payload data

The global validity of the product is a key requirement, since a space-borne GPS receiver tracks the complete GPS constellation in a single LEO orbit period of about 90-100 minutes. Therefore, clock and orbit corrections, which have been derived from

a regional network, are not useful for this task. The clocks have to represent the short term characteristics of the atomic frequency standards (AFS), which deviate significantly from a linear or quadratic behavior as a result of the clock noise. In order to achieve the desired accuracy of the positioning solution for PPP with carrier-phase observations, the satellite clock offsets must be estimated precisely at a sufficiently high rate to avoid interpolation errors. Last, a timeliness constraint must be met. In the particular application of LEO-POD though, this constraint is relaxed compared to other real-time applications. In general, the contact times to LEO satellites are limited, since a global coverage of downlink-stations cannot be reached. Satellites on a polar orbit can achieve contacts every orbit with only one downlink station at high latitudes. Many Earth observation missions use this cost-efficient approach. After the downlink, the LEO satellite's raw-data must be pre-processed before it is available for POD. If the GPS orbits and clocks, on the other hand, are computed by a sequential filter, the latency of these products is only limited by the latency of the GPS observations and the processing time of the filter. With the use of global real-time tracking stations, the latency of the GPS products can be brought down to a few seconds, which is well below the latency of the LEO satellite's data.

In the course of this Ph. D. thesis, a REal-TIme system for CLock Estimation (RETICLE) has been set up at German Space Operations Center (GSOC) of DLR. It will be demonstrated that precise clock estimation can be performend in real-time using the existing real-time tracking stations of the International GNSS Service (IGS). The system implies a Kalman filter, which estimates, among other parameters, the clock states. It will be shown that the accuracy requirements for LEO POD missions are met with these products. However, the applicability of RETICLE is not only limited to this task, but can also be used for all applications where precise real-time clocks are required. Among these applications are PPP as well as integrity monitoring for navigation systems. To demonstrate the potential of the latter, a straightforward method to detect clock discontinuities has been implemented and an analysis of the clock jumps is presented. Finally, the clock estimation is extended to GIOVE-A and -B, which are test satellites for Europe's future navigation system Galileo. Based on the data from a dedicated tracking network, the first real-time clock product for GIOVE has been generated in the course of this thesis.

1.2 Current State of the Art

The Jet Propulsion Laboratory (JPL) has undoubtedly the longest experience with real-time GPS orbit and clock corrections. Already in 1996, JPL started to set up a network of GPS receivers all over the US, which transmit their dual-frequency measurements in real-time with an update-rate of 1 Hz. The raw-measurements are encoded into the SOC-format, a binary data-format developed by JPL, which allows a high data compression and enables the transmission of the measurements over the open internet. A processing center computes differential range corrections from these observations. Users within the continental US could achieve positioning accuracies of a few decimeters when applying these corrections [Bertiger et al., 1998]. Already in 2000, the network had been expanded to a global network with 18 stations and laid the foundation for

NASA's Global Differential GPS System (GDGPS), which is today one of the largest real-time networks with about 100 stations. A real-time capable version of JPL's precise GPS processing software (Real-Time GIPSY (RTG)) is used to process the dual-frequency measurements from the ground network and compute precise GPS orbits and clock-offset estimates [JPL, 2010]. The precise GPS ephemerides are then disseminated as corrections to the broadcast orbits and clocks [Muellerschoen et al., 2000]. The products can be accessed via the internet or via direct land line connections. Mobile users can receive the corrections from the Iridium satellite constellation. Users in space have access to the products transmitted by the Tracking and Data Relay Satellite System (TDRSS) [Bar-Sever et al., 2004].

Tests have shown that users of the GDGPS corrections achieve real-time kinematic positioning accuracies of a few decimeters with dual-frequency receivers [Kechine et al., 2004] and sub-meter accuracies with single-frequency receivers [Gao and Chen, 2005] for ground navigation. Orbit determination results using the GDGPS orbits and clocks with dual-frequency measurements from a LEO satellite exhibited decimeter 3D position errors [Bock et al., 2009; Hauschild and Montenbruck, 2009]. The GDGPS corrections have been freely available to users during the development phase of the system, but it was turned into a commercial service upon finalization.

The International GNSS Service as a non-profit provider of high-quality GNSS data joined the pursuit of (near) real-time GPS orbits and clocks already in 1999. During the IGS analysis center workshop in La Jolla, the first initiative was taken to reduce the latency of the production of GPS orbits and clocks, and already one year later, a new IGS product line has been set up. The new product was entitled IGS Ultra Rapid, emphasizing its short latency compared to the IGS final and rapid products [Fang et al., 2001]. Tab. 1.1 lists all current orbit and clock products from IGS. The IGU product was initially updated twice a day. In 2004, the update rate was increased to four times a day. The GPS observations originate from a subset of IGS stations, which are configured to submit their measurements every hour or every 15 minutes with short latency. The IGU product covers an interval of 48 hours, divided into the observed half and the predicted half. The IGS states the accuracy of the orbits to be approximately 10 centimeters for the predictions and less than 5 centimeters for the observed part. The accuracy of the clocks in the observed half of the products is on the order of 0.2 nanoseconds, which corresponds to approximately 6 centimeters. However, it should be noted that the accuracy only refers to the clock values at 15-min-intervals. If a smaller step size is required, significant interpolation errors will degrade the positioning performance [Montenbruck et al., 2005a]. The error of the clock predictions rapidly grows over time and has already reached the level of broadcast ephemeris errors after the latency of 3 hours. The remarkable performance of the orbit predictions cannot be achieved, since especially the older GPS satellite clocks have stochastic behavior and are affected by thermal changes in the satellite, which cannot be modeled reliably [Ray and Griffiths, 2008].

For completeness, the offline-products of the IGS are also listed in Tab. 1.1. The orbits of the Rapid product do not show a significant improvement, but the clock errors are reduced to approximately 3 centimeters. Unfortunately, the Rapid product is only delivered with 5-min-spacing, which introduces interpolation errors again if a smaller spacing is required. The update rate of the product is once per day and the latency

Tab. 1.1: Overview of current IGS products and planned Real-Time products [International GNSS Service, 2009]

IGS Products		Accuracy	Latency	Updates	Sampling
Real-Time	orb clk	- ∼0.3 ns	10 sec	every 10 sec	10 sec
Ultra-Rapid (IGU) pred.	orb clk	∼10 cm ∼5 ns	0 h	every 6 h	15 min
Ultra-Rapid (IGU) obser.	orb clk	<5 cm ∼ 0.2 ns	3 h	every 6 h	15 min
Rapid (IGR)	orb clk	<5 cm 0.1 ns	17 h	every day	15 min 5 min
Final (IGS)	orb clk	<5 cm <0.1 ns	∼ 13 days	every week	15 min 5 min / 30 sec

is 17 hours. However, the orbit and clock solutions of the individual analysis centers used for the combination are available with a shorter latency. The rapid product of the Center for Orbit Determination in Europe (CODE) is usually available after 8.5 hours. The Final IGS product has the longest latency. The largest improvement over the Rapid product is gained in the clock offset estimation, which is expected to be lower than 0.1 ns or 3 centimeters. Contrary to the other products, a version with 30-sec-sampling is offered, which provides the necessary stepsize for most high accuracy applications.

After the quick realization of the Ultra-Rapid products, the next steps towards real-time took much longer. A real-time working group was formed within IGS already in 2001. During the next years until 2005, the foundation for a real-time tracking network consisting of 36 IGS stations was laid. The prototype real-time network used UDP connections for data transmission and the RTIGS-protocol to transport observations and meta-data. In parallel, a second streaming technique called Networked Transport of RTCM via Internet Protocol (NTRIP) has been developed [Weber et al., 2005] and a growing number of IGS real-time stations are transmitting their measurements with this protocol. In October 2007, a real-time pilot project (RTPP) was started [IGS Real Time Pilot Project, 2009]. There have been three main objectives defined for the pilot project: First, it was necessary to further extend and maintain the real-time tracking network. At the beginning, the global station distribution was highly asymmetric. Additionally, the two co-existing data transmission protocols were not compatible and as a result, users could only access half of the network, depending on which protocol they used. The second objective is to produce and monitor real-time products. Since September 2008, orbits and clocks derived from the real-time data are compared with respect to the IGS rapid products in an offline process. ESA/ESOC, Natural Resources Canada (NRCan) and DLR/GSOC were the first real-time analysis centers to submit products for comparisons. Bundesamt für Kartographie und Geodäsie (BKG) joined shortly afterwards. Since the beginning of February 2009, the offline products are combined into a combined clock product. At the time of writing, progress towards a true real-time combination and dissemination of the clock product is made, which is the third objective of the pilot project. Once it is implemented, the combined IGS clocks will be available as a data-stream with a latency of 10 seconds. Additionally, the first groups are starting with the implementation of ionospheric monitoring and the derivation of global TEC-maps with short latency.

All four analysis centers submitting to the RTPP have adopted the strategy to separate the orbit and clock estimation processes. The orbits are estimated in a batch estimation process and then predicted for the real-time clock estimation. ESA's Real-Time Navigation System (RETINA) estimates and predicts the GPS satellite orbits every two hours. The clock estimates are computed by a Kalman filter, which estimates satellite and station clock offsets, tropospheric zenith delays and carrier-phase ambiguities [Agrotis et al., 2008]. NRCan performs batch orbit determination-runs and predictions every hour. The clock estimation system is based on a least-squares sequential filter [Agrotis, 2008]. BKG utilizes the RTnet software [Weber et al., 2007], which comprises a Square-Root-Information-Filter for the sequential clock estimation. Contrary to the information in the cited reference, BKG's solution has now also been expanded to a global solution. Absolute clock estimates are computed instead of time-differenced clocks, which were not compatible in the direct comparison of the analysis centers. Besides these agencies, groups at GMV, Spain, and Geo++, Germany, are also working on real-time clock estimation products.

The applications for precise real-time orbits and clocks are already manifold today and it can be expected to grow rapidly in the near future, when more sources for these products become available. An application of special interest for this work is the precise orbit determination of LEO satellites with short latency. The main driver behind the push towards real-time in LEO POD are missions with payloads for observing GPS occultations. These satellites are equipped with zenith-pointing navigation antennas as well as occultation antennas, pointed towards the horizon of the Earth. A special occultation receiver tracks satellites from the zenith-pointing antenna for navigation as well as signals from the occultation antenna(s), which have travelled through the atmosphere and have therefore been retarded and bent. The bending angle can be computed from the phase shift and doppler shift of the GPS signal. It relates to temperature, pressure and water vapor in the atmosphere. The computation of the bending angle requires the LEO velocity error to be less than 0.1 mm/s [Rocken et al., 2000]. The data derived from occultation measurements are used for meteorological studies of the Earth's atmosphere, but also for near real-time weather predictions, which explains the timeliness constraint on the POD. After having first been proposed in 1988 [Yunck et al., 1988] and for the first time demonstrated with the GPS/MET experiment on the small satellite MicroLab 1 [Ware et al., 1996], radio occultation payloads have been employed on several satellite missions like Champ, SAC-C, GRACE, COSMIC/FORMOSAT, MetOp and TerraSAR-X [Wickert et al., 2007]. The COSMIC/FORMOSAT mission and the MetOp mission already require near real-time data processing. For MetOp, a dedicated ground support network has been established to compute GPS orbit and clock products from a network of 20-40 stations, which transmit their measurements with short latency. GPS orbits and clocks are produced in batch processing and updated every 15 minutes [Zandbergen et al., 2006].

A second type of mission with a near real-time orbit determination requirement is ESA's Sentinel-3 mission. This future mission is designed for oceanographic observations. Its payload comprises a radar altimeter, which measures the sea surface height. In this case, a near real-time orbit determination requirement of less than 10 cm for the radial orbit component has been defined [Bock et al., 2009].

Finally, remote-sensing missions for disaster monitoring could also have near real-time orbit determination requirements. For the derivation of quick-look products a quick and precise geo-location of the payload data is necessary and requires a precise and timely orbit determination of the satellite. These examples for space missions demonstrate that precise orbit determination with short latency are required for many satellites already today and will become more and more important in the future.

1.3 Thesis Overview

The thesis starts with an overview of the atomic standards on board GNSS satellites in Chap. 2. A brief overview of the historic GPS satellites is followed by a more detailed summary of the currently active satellites. The clock performance is analyzed and compared among the different clock types. Additionally the clock of the new test satellites for the future European global satellite navigation system Galileo are introduced. Finally, an outlook is provided into the future satellites for GPS and Galileo.

The real-time network, which provides the measurements for the real-time clock estimation, is introduced in Chap. 3. The existing techniques for real-time dissemination of GNSS measurements are summarized, including a short overview and discussion of existing data formats. Next, the stations selected for processing are introduced and the measurement performance is characterized. Finally, an overview of the COoperative Network for Giove Observations (CONGO) is provided, which is the first receiver network for global observations of the GIOVE satellites.

The REal-TIme CLock Estimation (RETICLE) system, which has been developed in the course of this thesis, is introduced in Chap. 4. A general overview of the system is followed by the description of the used models for GPS and GIOVE observations and the design of the Kalman filter, which is the core algorithm of the system. The solution for satellite clock jump detection and mitigation is described. Finally, the effect of orbit errors on the clock estimation is analyzed and mitigation methods are described.

The first analysis section (Chap. 5) presents orbit determination results obtained with real flight data from the TerraSAR-X satellite in simulated near real-time orbit determination scenarios. Achievable orbit accuracies for a reduced-dynamics and a kinematic orbit determination are shown. Finally, a real-time capable navigation algorithm is also analyzed to demonstrate the potential performance if the RETICLE clock estimates would be broadcast via geostationary relay satellites for on-board use.

An overview of the IGS real-time pilot project is presented in Chap. 6. The RETICLE clocks have been submitted as a contribution to the project for more than a year. The statistics derived by the analysis center coordinator from orbit and clock comparisons with respect to the IGS Rapid product are presented.

Next, results for the GIOVE real-time clock estimation are presented in Chap. 7. The chapter briefly introduces the real-time processing of the observations from the dedicated GIOVE tracking network and the generation of the combined GPS/GIOVE orbit and clock product. The quality of the GIOVE real-time clocks is analyzed and results for single-point-positioning and precise point positioning with GPS and GIOVE are shown for a selected test case.

Finally, Chap. 8 provides a summary of the key findings. Furthermore, suggestions for future research work in the field of GNSS real-time clock estimation are made.

1.4 Research Contributions

In this thesis, a complete system for GNSS clock offset estimation in real-time has been developed and implemented. The system provides clock offsets not only for the complete GPS constellation, but also for the new Galileo test satellites. The estimated GPS clock offsets are provided to the IGS Real-Time pilot project and will be a part of the future combined real-time clock product. The products are furthermore used for demonstrations of near real-time precise orbit determination performance. RETICLE products are internally used for the TerraSAR-X satellite by the German Space Operations Center of DLR [Wermuth et al., 2009], for a study with Jason-2 [Andres et al., 2009] by EUMETSAT and for the MetOP-A satellite.

A clock jump detection algorithm has been implemented for the RETICLE system. This algorithm prevents the clock estimation from being corrupted by large discontinuities of satellite clocks. The algorithm's suitability is proven on the example of three recent clock discontinuities. Furthermore, the effect of orbit errors on the clock estimation has been analyzed. It could be shown that constant orbit errors in the along-track component of the orbits lead to growing biases in the clock estimation, an effect which could actually be observed in the RETICLE system. A mitigation method is introduced, which does not require an improvement of the orbit predictions.

Finally, the first real-time clock estimates of the GIOVE satellites have been produced in the course of this thesis. The measurements stem from a dedicated global tracking network for GIOVE-A and GIOVE-B. Valuable insights are gained from processing new signals and multiple satellite systems in real-time, for example about the proper handling of inter-signal- and inter-system biases.

The RETICLE system provides a basis not only for real-time clock estimation, but also for other real-time processing activities. Due to its versatility and flexibility, new navigation systems like Galileo or QZSS can easily be incorporated.

2. The Atomic Standards of GNSS Satellites

In the following sections, a brief historical overview of the different GPS satellite block types is presented, followed by a short description of the GIOVE satellites, which are test satellites for the future Galileo constellation. The atomic frequency standards (AFS) used on the different satellites are introduced. Emphasis is put on the description of the currently active satellites. An overview of the performance of the atomic clocks is presented.

2.1 Historic GPS Satellites

2.1.1 Block I Satellites

The first eleven satellites of the GPS constellation were the Block I satellites built by Rockwell International. The first satellite was launched on February, 22nd, 1978, the last on October, 9th, 1985. One out of the eleven launches failed. The first constellation was intended for verification of the GPS concepts and subsequent spacecrafts have been modified based on the experience from the earlier launches. The navigation payload of the first Block I satellites contained rubidium atomic frequency standards (RAFS) exclusively. In 1983, the first cesium atomic frequency standard (CAFS) was implemented into SVN 8. Contrary to the RAFS, a long development time and problems in the space qualification prohibited the employment of cesium clocks in the GPS system at the very beginning. The last four Block I satellites, however, were equipped with one cesium clock and two rubidiums [Dieter and Hatten, 1995]. Until today, two different types of atomic clocks are foreseen in every GPS satellite, to avoid being dependent on the successful and timely development, testing and qualification of a single technology. The design life-time of a Block I satellite was 5 years, but the average life-time of the ten satellites was 9.5 years. In November 1995, the last remaining Block I satellite was decommissioned [Kaplan, 2006].

2.1.2 Block II Satellites

The Block II satellites were developed as the first satellites of the operational GPS constellation. Therefore they contained several modifications of the satellite bus as well as the navigation payload to fulfill the operational requirements for GPS. The major modification of the satellite bus included radiation hardening of sensitive components as well as an automated momentum dumping procedure to eliminate the need for ground assistance over longer time intervals. The navigation payload was extended with the “Selective Availability“-feature, which allowed an accuracy reduction of the positioning solution for standard (civilian) users [Georgiadou and Doucet, 1990].

The first launch of a Block II spacecraft took place in February 1989 and by October of the following year all nine satellites were put in orbit. Two cesium atomic frequency standards and two rubidium atomic frequency standards were employed on each spacecraft. It should be noted, however, that only one clock is active and used for the generation of the navigation signals. The remaining clocks are kept for redundancy in case the active clock fails to perform according to the specifications or is lost completely [Dieter and Hatten, 1995]. The design lifetime of a Block II satellite was 7.5 years, however, the average lifetime of the Block II satellite was about 12 years [Kaplan, 2006]. The last Block II spacecraft was excluded from the operational constellation as late as November 2006.

2.2 Current GPS Satellites

2.2.1 Block IIA Satellites

The Block IIA satellites are modified versions of the Block II type. Their usage began with the first launch in November 1990, and by November 1997 all 19 spacevehicles were launched. The modifications mainly improved the on-board-autonomy of the satellite bus and payload, to allow for longer operations without ground control station involvement. The layout of the Block IIA timing system is identical to its predecessor, so again two CAFS and two RAFS were implemented. Tab. 2.1 provides on overview of the GPS constellation as of June, 2009. At the time of writing, 12 Block IIA satellites are active in the current GPS constellation. Seven of these spacecraft are operated on cesium clocks, all others use rubidium clocks.

2.2.2 Block IIR/IIR-M Satellites

The Block IIR satellites are the latest generation of satellites which are currently active in the constellation. The launches of the replenishment satellites began in January 1997. Since September 2005, a modernized version of this satellite type is employed, which offers additional signals like the military M-Code and a new civil signal (L2C) on the L2 frequency. At the time of writing, approximately two-thirds of the GPS constellation consists of Block IIR/IIR-M satellites. Both the conventional and the modernized satellites have a completely new design of the timekeeping system (TKS) of the navigation payload. Contrary to the previous satellites, only rubidium frequency standards are used, since the cesium clocks did not pass the space qualification tests [Wu and Feess, 1999]. The timing signal originates from a voltage controlled crystal oscillator (VCXO), whose frequency is controlled by a rubidium atomic clock. Two additional rubidium clocks are present as back-up devices. A phase meter compares the phase output of both devices and the measured error in the relative phase is used in a control algorithm to adjust the frequency of the VCXO. Additionally, the TKS monitors the relative phase error and detects phase jumps of either the RAFS or the VCXO. The newly designed IIR timekeeping system exhibits a significantly improved clock stability over longer time intervals [Petzinger et al., 2002].

For the assessment of the stability of an oscillator, the Allan deviation (ADEV) is commonly used. It is a measure of a clock's stability in terms of sample differences over

Tab. 2.1: Overview of current GPS constellation (June 2009)

PRN	SVN	Block-Type	Launch Date	AFS	Orbit Plane
01	49	IIR-M	2009/03/24	Rb	B2
02	61	IIR	2004/11/06	Rb	D1
03	33	IIA	1996/03/28	Cs	C2
04	34	IIA	1993/10/26	Rb	D4
05	-	-	-	-	-
06	36	IIA	1994/03/10	Rb	C5
07	48	IIR-M	2008/03/15	Rb	A6
08	38	IIA	1997/11/06	Cs	A3
09	39	IIA	1993/06/26	Cs	A1
10	40	IIA	1996/07/16	Cs	E3
11	46	IIR	1999/10/07	Rb	D2
12	58	IIR-M	2006/11/17	Rb	B4
13	43	IIR	1997/07/23	Rb	F3
14	41	IIR	2000/11/10	Rb	F1
15	55	IIR-M	2007/10/17	Rb	F2
16	56	IIR	2003/01/29	Rb	B1
17	53	IIR-M	2005/09/26	Rb	C4
18	54	IIR	2001/01/30	Rb	E4
19	59	IIR	2004/03/20	Rb	C3
20	51	IIR	2000/05/11	Rb	E1
21	45	IIR	2003/03/31	Rb	D3
22	47	IIR	2003/12/21	Rb	E3
23	60	IIR	2004/06/23	Rb	F4
24	24	IIA	1991/07/04	Cs	D5
25	25	IIA	1992/02/23	Rb	A5
26	26	IIA	1992/07/07	Rb	F5
27	27	IIA	1992/09/09	Cs	A4
28	44	IIR	2000/07/16	Rb	B3
29	57	IIR-M	2007/12/20	Rb	C1
30	30	IIA	1996/09/12	Cs	B2
31	52	IIR-M	2006/09/25	Rb	A2
32	23	IIA	1990/11/26	Rb	E5

varying sample intervals [Allan, 1983]. Assuming that a number of N clock samples is present with the minimum spacing of τ_0. The Allan variance, which is the square of the Allan deviation, is then computed as the mean of the differences of adjacent slopes [Audoin and Guinot, 2001]:

$$\sigma^2(\tau) = \frac{1}{2\tau^2(N-3n+1)} \sum_{i=1}^{N-3n+1} \left[(x_{i+2n} - 2x_{i+n} + x_i)^2\right] \tag{2.1}$$

where the time intervals τ are integer multiples of the fundamental interval $\tau = n\tau_0$. When plotting the values for the Allan deviation over the sample size τ on a log-log graph, different noise types are distinguishable depending on the slope of the curve. White phase noise and the Flicker phase noise exhibit a slope of τ^{-1}, white frequency noise varies with $\tau^{-\frac{1}{2}}$, Flicker frequency noise stays constant with varying τ and random walk noise of the frequency varies with $\tau^{\frac{1}{2}}$. A limitation of the Allan deviation is that white phase noise and Flicker phase noise cannot be distinguished. For that purpose, the modified Allan deviation is defined, which resolves this ambiguity by averaging over

adjacent samples. On the log-log plot of the modified Allan deviation over the time interval τ, white phase noise of the clock has a steeper slope for the modified Allan deviation and varies with $\tau^{-\frac{3}{2}}$, whereas the Flicker phase noise exhibits τ^{-1} dependency. All other noise dependencies remain the same as previously described. The modified Allan deviation (MDEV) is computed according to [Allan, 1987]:

$$\mathrm{Mod}\,\sigma^2(\tau) = \frac{1}{2\tau^2 n^2 (N-3n+1)} \sum_{j=1}^{N-3n+1} \left[\sum_{i=j}^{n+j-1} (x_{i+2n} - 2x_{i+n} + x_i)^2 \right] \tag{2.2}$$

Fig. 2.1 depicts the modified Allan deviations of the clocks used in the current GPS constellation. The clocks are grouped into the four different types Block IIA rubidium, Block IIA cesium, Block IIR and Block IIR-M. Final CODE clocks with a 5 second spacing have been used to compute the Allan deviation over time intervals τ from 5 seconds to 9000 seconds. It becomes obvious that the clocks exhibit characteristic behavior depending on the block type. The Allan deviation of the Block IIA rubidium clocks (blue) ranges from approximately $2 \cdot 10^{-12}$ at 10 seconds intervals to $2 \cdot 10^{-13}$ at 1000 seconds. The Allan deviation varies with $\tau^{-0.5}$, which corresponds to a random walk noise process in the clock phase. In a range from several tens of seconds up to several 100 seconds, these clocks have the best stability and even outperform the newer Block IIR rubidium clocks.

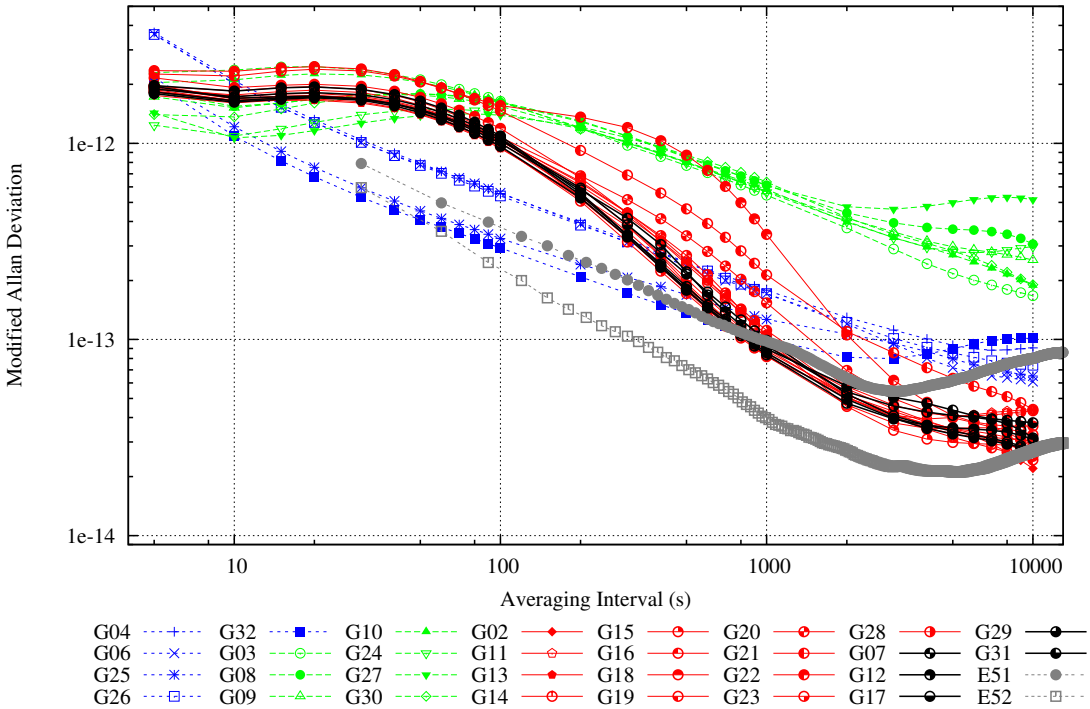

Fig. 2.1: Modified Allan deviations of the current GPS satellite clocks based on CODE final clocks with 5 second spacing from May 17th to May 29th 2009. Blue color indicates Block IIA Rb, green is Block IIA Cs, red indicates Block IIR (all Rb) and black depicts Block IIR-M (all Rb). The Allan deviation of the rubidium clock of GIOVE-A (E51) and the passive hydrogen maser of GIOVE-B (E52) is based on final clock solutions from IAPG/TUM for July 4th and 5th, respectively [Hugentobler et al., 2010].

The Block IIR and Block IIR-M clocks are plotted in red and black, respectively. The Allan deviation of these clocks varies as τ^{-1} for τ between 100 s and 2000 s, which corresponds to Flicker phase noise. This behavior is caused by the noise of the phase meter, which controls the frequency of the VCXO and degrades the stability in the short-term regime. Long term stability, however, is dominated by the rubidium standard [Petzinger et al., 2002]. For time intervals longer than 2000 s, the Block IIR/IIR-M clocks have the best performance of all GPS clocks and their Allan deviation varies as $\tau^{-0.5}$. It can also be seen that all Block-IIR/IIR-M rubidiums show an unexpected behavior for time intervals shorter than 100 s, where the Allan deviation flattens with decreasing τ. This is a typical behavior of the Allan deviation if data averaging is applied, for example in a phase comparator [van Baak, 2009]. A possible explanation could be that this effect is due to internal smoothing in the phase meter of the TKS. The Block IIA cesium clocks (green color) show the worst stability compared to all other clocks from averaging times of 100 seconds upwards. The power law dependency in this region corresponds to a random walk noise process in the clock phase similar to the rubidium clocks. For shorter averaging times, however, the cesium clocks exhibit a behavior similar to the Block IIR rubidium clocks. This is an unexpected result, since no indication for a coupling of VCXO and AFS for the cesium atomic frequency standards has been found in the literature. However, Emmer and Watts [1997] present the Allan deviation for a prototype of a cesium atomic frequency standard, which exhibits similar characteristics for short time intervals. It is therefore likely that this performance is also typical for Block IIA cesium clocks. The degraded stability of the cesium clocks compared to the IIA rubidiums is not surprising, since the advantage of this clock type is the high stability over time intervals on the order of days, which exceeds the scale of Fig. 2.1.

2.3 Future GPS Satellites

2.3.1 Block IIF Satellites

The Block IIF (follow-on) satellites were originally planned to be launched beginning in 2001, but the long lifetime of the current GPS satellites did not raise a pressing need for additional launches. The most important feature of the new satellites for civil users is the addition of a new signal in the new L5 frequency band. Furthermore, the design criteria for the AFS design have been tightened to achieve a higher stability and predictability of the on-board clock. The satellites will carry one cesium and two rubidium clocks. The rubidium clocks performance has been improved by employing a phase meter with a much higher measurement precision, which will significantly improve the short term stability. Tests show that the Allan deviation for the improved RAFS with be at $5 \cdot 10^{-13}$ for averaging intervals of 5 seconds and $2 \cdot 10^{-14}$ for averaging intervals of 1000 seconds [Dass et al., 2002]. The cesium atomic standard is an advancement of the Block II/IIA cesium clocks. The clock will be digitally controlled and have an improved stability and lifetime. The Allan deviation of the CAFS for averaging intervals of 5 seconds is at $8 \cdot 10^{-12}$ and $8 \cdot 10^{-13}$ for averaging intervals of 1000 seconds. Tests of clock prototypes indicate that the stability of the rubidium clock will exceed that of the cesium clock by

approximately one order of magnitude for averaging intervals between 10 seconds and 10000 seconds [Emmer and Watts, 1997].

2.3.2 Block III Satellites

The next generation of GPS satellites, Block III, is currently under development. Besides new military and civil signals, the satellites will offer autonomous integrity monitoring to guarantee the reliability of the GPS signals and the resulting navigation solution. Furthermore, the desired ranging accuracy of the next generation satellites has been reduced to sub-meter level [Martin, 2008]. This ambitious goal also requires advances in the atomic clock technologies to achieve the required stability of the clocks. Possible candidates are an optically pumped cesium clock [Lutwak et al., 2002], an advanced digital rubidium clock, a linear ion trap clock or a hydrogen maser [Wu and Feess, 1999]. All of these advanced or newly developed clocks are expected to have a stability, which is increased by at least one order of magnitude and will therefore enable excellent clock error predictions on the order of centimeters over several hours [Wu and Feess, 1999].

It should be noted however, that most of the GPS satellites exceeded their design lifetime by far. Therefore, the first launch of the Block III satellite generation may start in the middle of the next decade. It can be expected that it will take another decade until a sufficient number of next generation satellites are in operation and the user can benefit from the improved clocks. Until then, older satellites with badly predictable clocks will degrade precise point positioning accuracy unless precise clock offset corrections are available.

2.4 GIOVE Satellites

In order to test the new technologies and to reserve the frequencies to be used for the navigation signals of the operational constellation, two test satellites have been launched, which now form the Galileo In-Orbit Validation Element (GIOVE). The first satellite GIOVE-A was launched on December 28th, 2005, on a Soyuz Rocket from Baikonur. The first navigation signals from the satellite were received on January 12th, 2006. The dimensions of the spacecraft structure without the solar-panels is approximately 1.3 m by 1.3 m by 1.8 m with a total mass of 610 kg at the beginning of the mission. The satellite's navigation payload is capable of generating signals on the three Galileo frequencies, however, only two signals can be sent at a time. Therefore, the satellite is either transmitting signals on the E1- and E5-band or the E1- and E6-band. From February 2006 to October 2008, the E1E5-signal combination was transmitted during 65% of the time and the E1E6-combination had been active 24% of the time. During the remaining periods, the signal transmission was discontniued or experiments with other signals have been performed [Surrey Satellite Technology Ltd., 2008]. The satellite is equipped with two rubidium atomic frequency standards. One of these RAFS is used as the source of the timing signal used for the navigation payload, the other serves as a redundant unit. The nominal GIOVE-A mission ended in March 2008, however, the mission was extended for another 12 months. At the time of writ-

ing, the spacecraft is still operational and continues to transmit signals. However, since the satellite is significantly exceeding its planned lifetime, the propability of failures of bus-components, which are mission-critical, are more likely to occur. Therefore, its orbit has been raised by 35 km in October and September 2009 to a graveyard orbit in order to provide space for the future operational Galileo satellites. The spacecraft is depicted in Fig. 2.2.

The clock performance of the GIOVE-A RAFS is also depicted in Fig. 2.1. The plot of the Allan deviation is based on data from IAPG/TUM for July 4th, 2009 [Hugentobler et al., 2010]. It becomes obvious that the Allan variation varies as $\tau^{-0.5}$, which corresponds to white frequency noise from time intervals between 30 seconds until 2000 seconds. For larger time intervals, the Allan deviation increases again with $\tau^{0.5}$, which would indicate random frequency walk. The results show that the GIOVE-A RAFS shows comparable performance to the rubidium clocks of GPS, except for the increase in the Allan deviation for larger τ. Waller et al. [2009] also provide a comparison of the GIOVE clocks with GPS clocks for November of 2008. Though the results for GIOVE-A are in general comparable with the plot in Fig. 2.1 and also show the increase in the Allan deviation at 2000 seconds, the GIOVE-A clock performance exceeds the performance of the GPS clocks in their analysis for τ smaller than 4000 seconds.

Fig. 2.2: ESA's GIOVE-A test satellite (imagery courtesy of ESA)

Fig. 2.3: ESA's GIOVE-B test satellite (imagery courtesy of ESA)

The second test satellite, GIOVE-B, was launched on April 27th, 2008. The first navigation signal have been broadcast on May 7th, 2008. The mass of this satellite was approximately 530 kg and the dimension of 0.95 m by 0.95 m by 2.4 m. Similar to its predecessor, GIOVE-B is also only capable of providing two out of the three planned Galileo signals at a time. The timing source for the navigation signals can be either one of the two rubidium frequency standards or the Passive Hydrogen Maser (PHM). The latter clock type has never been flown in space before and is planned to be used for the future Galileo constellation. Several assessment campaigns have shown that the stability of the PHM exceeds the stability of all other atomic frequency standards currently used in other GNSSs [Robertson et al., 2009]. The GIOVE-B satellite is depicted in Fig.2.3. It becomes obvious, that the satellite-bus design differs significantly from GIOVE-A. Also, the broadcast navigation signals from the two spacecraft differ on the E1-frequency. Whereas GIOVE-A still transmits the BOC(1,1)-modulation, the newer

CBOC-modulation has been implemented for GIOVE-B. The latter modulation type is also planned for the operational Galileo-constellation and is expected to enable a better multipath mitigation.

The results for the Allan deviation of the PHM of GIOVE-B are also shown in Fig. 2.1 and are based on data provided by IAPG/TUM [Hugentobler et al., 2010] for July 5th, 2009. It becomes obvious that the GIOVE-B clock exceeds the stability of all GPS clocks for time intervals larger than 60 seconds and smaller than 10^4 seconds. The Allan deviation starts to increase again for τ larger than 5000 seconds, which is consistent with the results presented in Waller et al. [2009]. It is interesting to note that for longer time intervals, which are depicted in the cited reference, the Allan deviation starts to decrease again. Therefore, the PHM is also one of the most stable clocks over longer time intervals.

3. Real-Time Tracking Network

This chapter will focus on the description of the real-time tracking network which is used by RETICLE. It will start with the overall network architecture and currently used formats followed by a brief overview of site characteristics. Finally, the dedicated GIOVE real-time tracking network is introduced.

3.1 Network Architecture

In the past, observations have been collected at the reference station and then transferred in batches in hourly or daily intervals to a central server, where they could be accessed by users. Many reference stations all over the world have been recently transformed into real-time tracking stations, which transmit their measurements via the internet using a protocol called "Networked Transport of RTCM via Internet Protocol (NTRIP)". This protocol has been developed by the Federal Agency for Cartography and Geodesy (BKG) [Weber et al., 2005]. It is based on the Hypertext Transfer Protocol (HTTP), which is used for the transmission of website contents on the internet. The basic schematic in Fig. 3.1 depicts the main elements of an NTRIP network. The stream content usually originates from GNSS receivers, also referred to as stream-servers. The data is sent to a caster, which is the central distribution point of the streams. Special formats have been defined for the purpose of streaming GNSS observations, GNSS ephemerides and station meta-data. A low data-rate is achieved by compression and binary encoding of the data. This way, even users with a slow internet connection, like mobile users, can access the data streams. Furthermore, the reception of data from many stations, as required for orbit or clock determination, is possible with high-speed internet access.

The most widely used format is RTCM 3.x, which has been developed by the Radio Technical Commission for Maritime Services. This format is implemented in many recent geodetic receivers. Currently, 69% of the streams offered at the global NTRIP-caster "www.igs-ip.net" are encoded in RTCM3. The format allows the transmission of dual frequency measurements for pseudorange, carrier-phase and carrier-to-noise-ratio for the GPS and the GLONASS system. The resolution for the pseudorange measurements is limited to 2 cm and the carrier-phase observations are resolved down to 0.5 mm. In addition to observations, the format has messages to transmit GPS and GLONASS broadcast ephemerides and station meta-data like the reference position and antenna information [RTCM, 2006]. Recently proposed extensions to the format will incorporate the transmission of the new Galileo signals. Furthermore, a set of state-space-messages has been defined to disseminate orbit and clock corrections in real-time [Wübbena, 2008]. The broad acceptance and implementation among the receiver man-

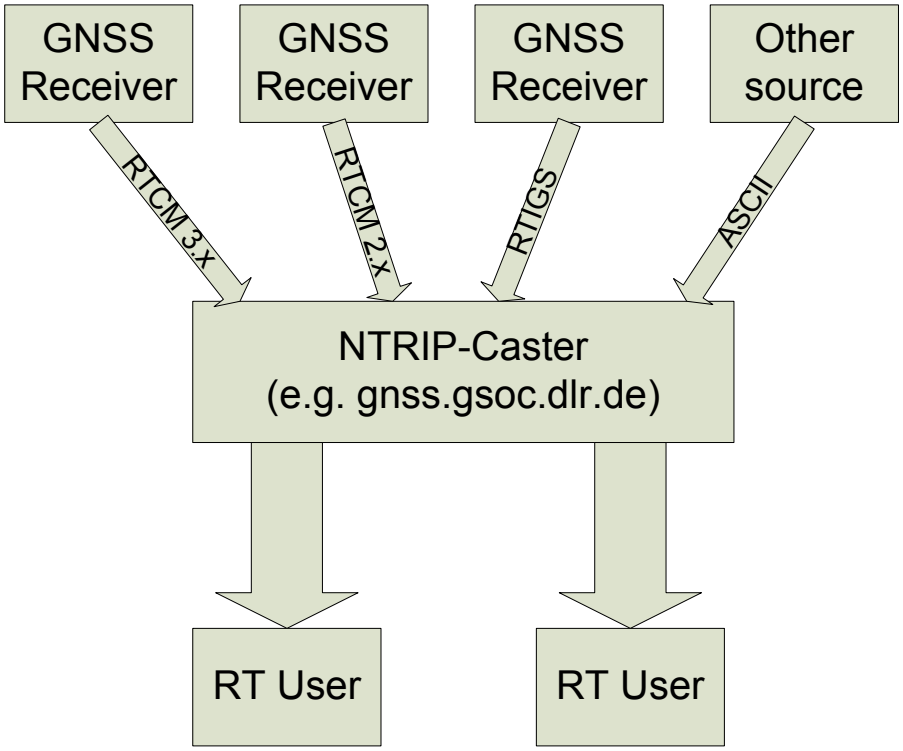

Fig. 3.1: Schematic of an NTRIP network

ufacturers is certainly one of the main advantages of this data format. The drawback on the other hand is the limitation to transmit only one signal type per frequency for the current GPS and GLONASS message types.

The format RTCM 2.x is the predecessor of RTCM 3 and still used by 13% of the stations transmitting to the caster “www.igs-ip.net”. The format allows the transmission of pseudorange and carrier-phase observations for GPS and GLONASS. Again, it is limited to one signal per frequency. The resolution of the pseudorange observable is 2 cm. Carrier-phase measurements can be resolved down to 1/256 cycles, which corresponds to approximately 1 mm. Antenna information and station positions can also be transmitted [RTCM, 2001].

The RTIGS format is currently used by 16% of the stations at “www.igs-ip.net”. It comprises four basic messages types: station information, GPS observations, broadcast ephemerides and meteorological data. The observation messages contain the GPS observations in SOC format, which has been developed by JPL [Muellerschoen et al., 2000]. The format allows the transmission of the C/A, P1 and P2 pseudorange observations and the L1 and L2 carrier-phases. Furthermore, carrier-to-noise ratios for C/A-, P1- and P2-pseudoranges are included. The pseudorange resolution is 1 mm and the carrier-phases are discretized to 0.02 mm. The advantage of this format compared to the RTCM-formats is the transmission of both C/A- and P1-code and the improved resultion of the observations. The drawbacks are that this format is not implemented in receiver firmware and thus the data stream must be created by seperate software. Furthermore, message definitions for future GNSS like Galileo or messages for real-time

clock and orbit corrections are currently not available. [IGS Real Time Working Group, 2009].

The users of the real-time data connect to the caster using an authorization with username and password and can request one or multiple data streams. The caster then routes the data flow from the data source to the user. NTRIP users and servers must of course handle interruptions of the stream and reconnect to the caster. The bandwidth for a NTRIP-stream in binary format is usually less than 5 kbits/s and the average delay in the data transmission from the remote locations is 2-3 seconds. The content of the NTRIP-streams is not limited to the three formats, which have been described previously. The protocol can carry data-streams in any format. This flexibility allows the transmission of proprietary formats, for example the raw-output of GNSS receivers without RTCM-support. Also, other sources than GNSS receivers can be connected to a caster. For example, the output of the RETICLE system is offered as real-time streams in RTCM3 and plain ASCII SP3 format.

Fig. 3.2 shows a map with the real-time stations used by RETICLE for the generation of the clock products. The colorscale indicates the depth-of-coverage (DOC). The DOC indicates the number of stations, which are able to simultaneously track a GPS satellite at a certain sub-satellite-point (SSP) on the map. The sub-satellite-point corresponds to the pierce point of the satellite's position vector (originating in the center of the Earth) with the Earth's surface. A bright color in the plot indicates a high DOC and dark colors indicate areas which are sparsely covered. It can be seen that the coverage in the areas around North America, Europe and Australia is highly redundant. However, a large part of the Pacific Ocean and smaller areas in Africa and Asia exhibit low coverage with only 4 or 5 stations per satellite. Naturally, a low DOC causes a reduced robustness of the clock estimation procedure for GPS satellites in these areas, since less redundant measurements are available and station outages have a higher impact. All data streams from the stations depicted in Fig. 3.2 contain dual frequency (GPS L1/L2) observations at a data rate of 1 Hz.

The majority of the real-time tracking stations of the RETICLE network are part of the IGS tracking network. Only five stations are not part of this network. The advantage of the IGS stations is the compliance with certain professional standards for operations and maintenance of the equipment. Furthermore, data from these stations are also processed by many other users also for offline products. This ensures that station outages are detected in a timely manner and feedback about the station data quality is provided by a larger group of analysts. Finally, the IGS station operators will inform the user community about equipment changes at the stations. Precise knowledge of the station position is crucial for the real-time clock estimation. The coordinates for most of the IGS stations are available from weekly updated solutions and provided in the Solution (Software/technique) INdependent EXchange Format (Sinex) [International Earth Rotation and Reference Systems Service, 2009]. The station positions are computed by the IGS analysis centers from post-processed observations of the complete IGS tracking network and they are tied to the IGS reference frame. The Sinex-files are also the source of the stations' meta data, which comprises receiver and antenna information, for example.

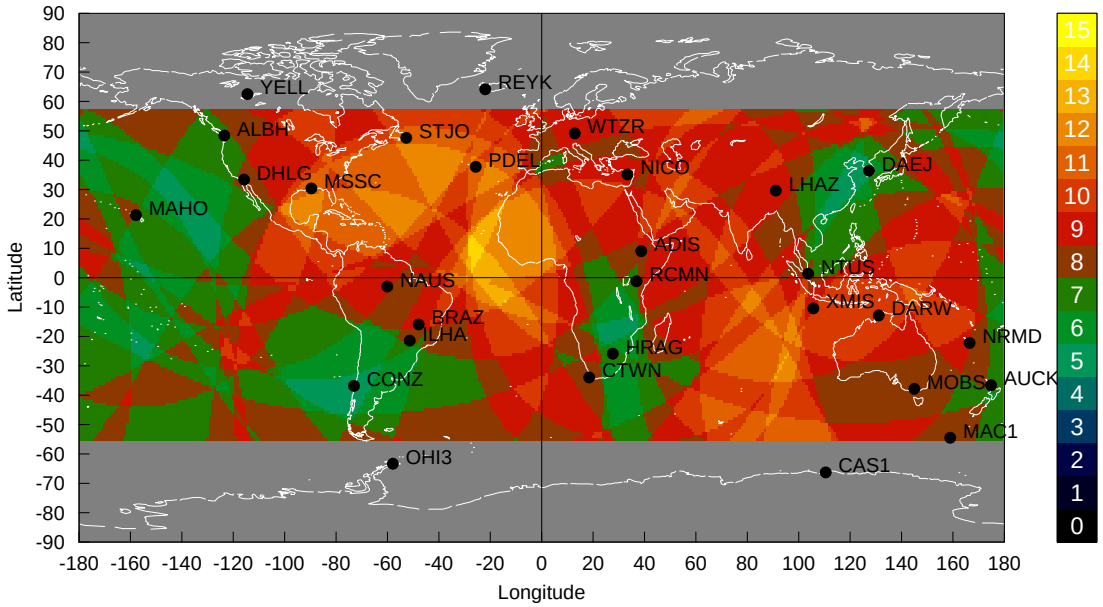

Fig. 3.2: Global NTRIP real-time station network used for RETICLE. The colorcode indicates the depth of coverage (DOC), which is the amount of stations able to simultaneously track a GPS satellite depending on its sub-satellite-point. An elevation mask of 10° is used in this plot.

The RETICLE-system can use data-streams provided in RTCM3, RTCM2 and RTIGS format, which are the three major formats in the NTRIP network. Additionally, decoding of some proprietary receiver-raw-formats is supported. Out of the 29 stations of the network shown in Fig. 3.2, 22 stream their measurements in RTCM 3 format, 2 stations use the older RTCM 2 format, 4 stations use the RTIGS format and 2 stations transmit the Javad raw format. As already mentioned, the RTCM-formats bring the significant disadvantage to transmit only one signal per frequency. Since all RTCM-stations transmit the C/A-code signal on L1 for single frequency users, the P1-code signal is omitted. This poses a problem in the processing, since the clocks in the IGS are based on the P1-P2 combination and biases exist between C/A-code and P1-code. Therefore, corrections must be applied during processing in order to remove the biases between the C/A-code and P1-code and to allow consistent processing with stations providing P1 and P2. The bias corrections will be discussed in more detail in Sec. 4.2.6.

It is also important to note, that a significant part of the tracking-network of the IGS has already been equipped with L2C-capable receivers, namely Trimble's NETRS or NETR5 and Leica's GRX1200GGPRO. These receivers are able to track the new civil signal of the Block IIR-M satellites on L2 (see Sec. 2.2.2). Four RETICLE stations have L2C-capable receivers, which are configured to transmit the C2-code in the data stream. Due to the RTCM3-format limitations, the P2-code is omitted in this case. Similar to the C/A-code and P1, there exists also a bias between the C2 and P2 observations, which must be regarded during processing. However, at the time of writing, these corrections are not yet routinely provided by an IGS analysis center. As a result, the observations of the Block IIR-M satellites of these station are omitted, which reduces the effective network coverage.

3.2 Site Characteristics

This section shows results from a network analysis, which has been performed in order to detect incorrectly configured real-time stations transmitting corrupt data. This analysis of the stations' measurement quality using the real-time streams directly is important, since the offline observation data does not necessarily originate from the same output stream of the receiver. Therefore, configuration problems may not be detectable for users of the offline measurements.

A straightforward method for data quality and integrity assessment is to perform a precise point positioning (PPP) using recorded Rinex files from the real-time network and post-processed precise GPS satellite clocks. The RMS of the pseudorange and carrier-phase residuals also give an indication of the combined effect of multipath errors and measurement noise at each station. In order to assure the comparability of the residuals among the stations, identical settings for data editing have been used. Tab. 3.1 summarizes the pseudorange and carrier-phase measurement residuals for the stations used for RETICLE.

Tab. 3.1: Overview of pseudorange and carrier-phase residuals for RETICLE stations

Station	PR [m]	CP [mm]	Receiver Type
ALBH	0.86	6	AOA Benchmark ACT
STJO	1.00	7	
YELL	1.11	6	AOA SNR-12 ACT
CTWN	0.77	9	Trimble NetR5
SMR5	0.85	7	
AZU1	1.15	9	Trimble NetRS
BRAZ	0.95	12	
KOUC	0.86	10	
NAUS	0.90	12	
NRMD	0.90	10	
SUWN	0.76	12	
CAS1	0.30	8	Leica GRX1200GGPRO
CONZ	0.90	6	
DARW	0.46	10	
FUNC	0.30	7	
ILHA	0.28	10	
MOBS	0.44	9	
NICO	0.34	8	
NTUS	0.38	10	
PDEL	0.30	10	
RCMN	0.32	9	
WTZR	0.63	9	
XMIS	0.34	10	
KIRO	0.80	9	JPS EGGDT
CEDU	1.06	8	Ashtech UZ-12
KARR	1.17	8	
MSSC	1.90	12	
DHLG	0.94	7	Ashtech Z-XII3
RIO2	1.12	7	
LHAZ	1.44	8	TPS E_GGD
REYK	1.46	9	

Stations which do not appear in Tab. 3.1 but are depicted in the plot of the network in Fig. 3.2 were affected by extended outages during the period of the network analysis and have therefore been omitted. The carrier-phase residuals for most stations amount to about 1 cm, only very few stations exhibit a better performance with 5-6 mm residuals. The pseudorange residuals on the other hand exhibit a large variation between the different stations. For the majority of the stations, the pseudorange residuals are between 0.9 m and 1.9 m. A group of stations exhibit significantly reduced residuals between 0.3 m and 0.4 m. All Leica GRX1200GGPRO receivers and one Trimble NetRS receiver belong to this group. For these receivers, an internal carrier-phase smoothing is apparently performed on the pseudorange observations, which reduces receiver noise and also multipath-errors to a certain extent.

The plots of the C/A code multipath combination in Fig. 3.3 show the difference between unsmoothed and smoothed pseudoranges. The stations NAUS and ILHA in Brazil have been selected, since they provide comparable observation conditions for PRN 24. The plot shows a complete pass of the satellite, which starts at approximately 5° elevation and rises up to more than 80° in both cases.

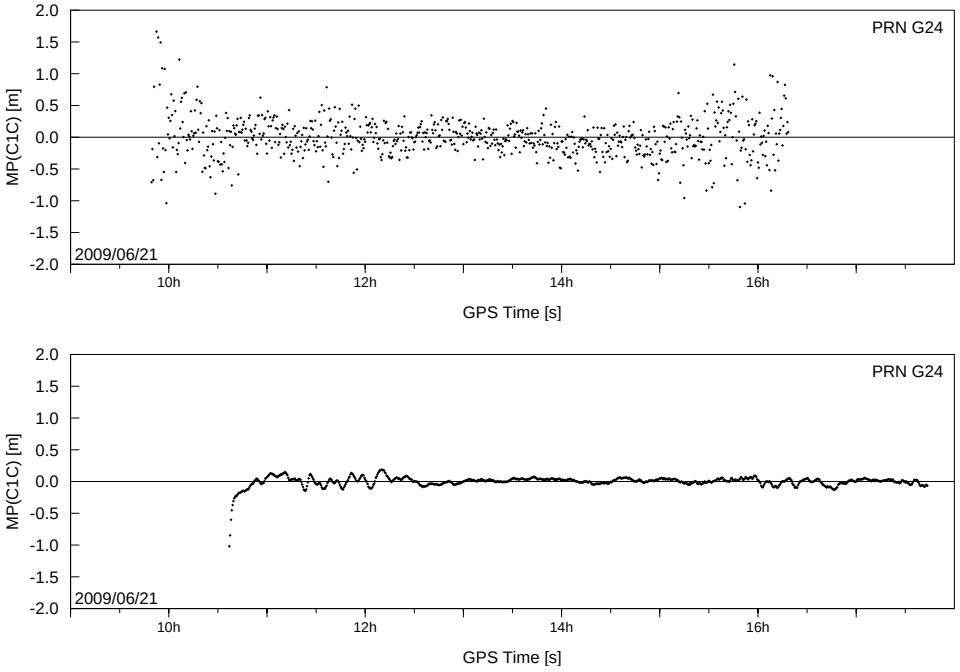

Fig. 3.3: C/A code noise and multipath for stations NAUS (top) and ILHA (bottom). The receiver at NAUS is a Trimble NetRS, ILHA employs a Leica GRX1200GGPRO with carrier-phase smoothing

It becomes obvious that NAUS streams the unsmoothed pseudorange observations. The amplitude of the measurement noise extends from about 1 m at low elevations to approximately 0.25 m at high elevations. The noise of the pseudorange for ILHA, on the contrary, does not exhibit a comparable elevation-dependency. The amplitude of the multipath combination stays well below 0.25 m for almost the entire pass. At the beginning of the pass, the smoothed pseudorange exhibits a notable bias of 1 m, which dissolves within several minutes. This problem could be caused by the systematic nature of the multipath-errors, which prevents a proper convergence of the smoothing

filter. At the beginning of the pass, when the satellite has just been acquired and hence carrier-phase measurements are only available from a limited interval, the smoothing duration is shorter than the variations of the multipath. Consequently, the smoothed pseudoranges are biased. At the end of the tracking interval, carrier-phases from a sufficient time interval are available to effectively reduce multipath. In order to avoid that biased pseudoranges are processed, an elevation limit should be used to omit potentially degraded measurements.

The carrier-to-noise density ratio is also an important observable for the assessment of the station performance. The two most widely used receivers have been selected as examples in Fig. 3.4 and Fig. 3.5, which show the carrier-to-noise density ratio over elevation and the semi-codeless tracking losses. Fig. 3.4 depicts the station BRAZ, which uses a Trimble NetRS receiver. The C/N_0 for the C/A-code in the left plot (S1C) varies from approximately 35 dB-Hz at low elevations to about 50 dB-Hz at the zenith. The C/N_0 for P2 (S2W) is significantly reduced due to the semi-codeless tracking losses and varies between 17 dB-Hz and 40 dB-Hz. The carrier-to-noise ratio of the L2C signal (S2C) can be tracked directly and is therefore not affected by losses. The L2C-C/N_0 almost reaches up to the values for the C/A-code. The right plot depicts the semi-codeless tracking losses with respect to the C/A-code on the y-axis. The abscissa provides the carrier-to-noise density ratio of the reference. The P2-code is clearly affected by increasing losses for a decreasing C/N_0 of the C/A-code. The line indicates the relation which would be expected for Z-tracking in case of identical L1 and L2 signal levels and antenna gains. It is furthermore obvious that no losses exist for the direct L2C-code tracking, however, frequency-dependent sensitivities of the antenna may cause a certain variation.

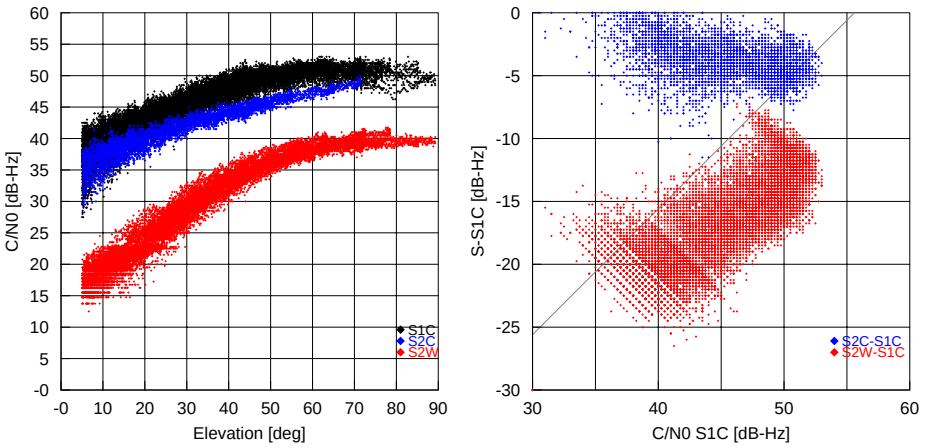

Fig. 3.4: C/N_0 over elevation (left) and semi-codeless tracking losses (right) for station BRAZ, Trimble NetRS

Fig. 3.5 depicts the same type of plot for Leica's GRX1200GGPR0 used at the station WTZR. The receiver is not set up for L2C-tracking, thus only the C/A-code and the P2-code and their corresponding carrier-to-noise density ratios are reported. The C/N_0 for the C/A-code varies from about 40 dB-Hz to 50 dB-Hz. The carrier-to-noise density ratio for P2 starts at 32 dB-Hz for low elevations and rises up to 48 dB-Hz at the zenith. The reported C/N_0 for both observables varies significantly from the Trimble

receiver. This difference becomes clearly visible in the right plot of Fig. 3.5 for the semi-codeless tracking losses. A similar pattern can be found for all Leica-receivers in the network. It can be attributed to the fact that Novatel as well as Leica receivers report non-standard values for the C/N_0.

The analysis of the C/N_0-plots is useful to identify incorrectly configured receivers or hardware deficiencies. For example, due to software incompatibilities, the L2C-observations of several receivers in the RTPP-network where erroneously flagged as P2-observations. This causes problems during processing due to the aforementioned satellite- and receiver-specific differential code biases. The L2C-observations could be identified from their untypically high C/N_0-values. In a second case, the carrier-to-noise ratios of a receiver for P2-observations where too low and most measurements where rejected during data editing. Ultimately, this receiver had to be replaced.

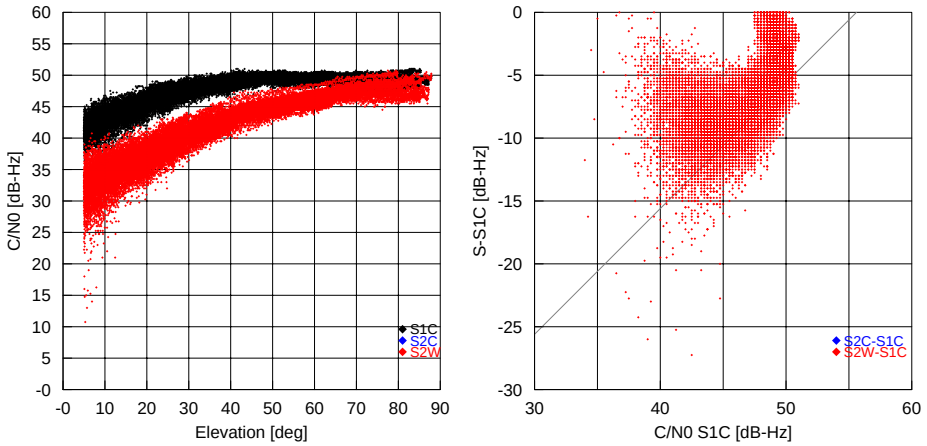

Fig. 3.5: C/N_0 over elevation (left) and semi-codeless tracking losses (right) for station WTZR, Leica GRX1200GGPRO

3.3 GIOVE Tracking Network

Each station in the IGS real-time tracking network provides measurements for GPS satellites. A smaller subset of these stations additionally transmits observables of the GLONASS satellites, depending on the receiver used at the station. For the observation of the satellites of ESA's Galileo In-Orbit Validation Element (GIOVE), the IGS network neither has suitable receivers nor do the authorized data formats currently support the transmission of Galileo measurements. In order to make these observations available to the scientific community, a dedicated GIOVE tracking network has been established as a joint effort by several institutions. The network is therefore called CO-operative Network for Giove Observation (CONGO). The first step in its employment has been taken by DLR/GSOC with the relocation of a Septentrio GeNeRx receiver to Sydney (Australia) in January 2008. Shortly afterwards, two additional GeNeRx receivers have been set-up by the Bundesamt für Karthografie und Geodäsie (BKG) in Wettzell (Germany) and Concepcion (Chile). During the following year until January 2010, additional stations have been added to the network by BKG and DLR. In July

2009, a global tracking coverage of the GIOVE satellites was possible for the first time. Since January 2010, a network of ten stations is operational, as depicted in Fig. 3.6.

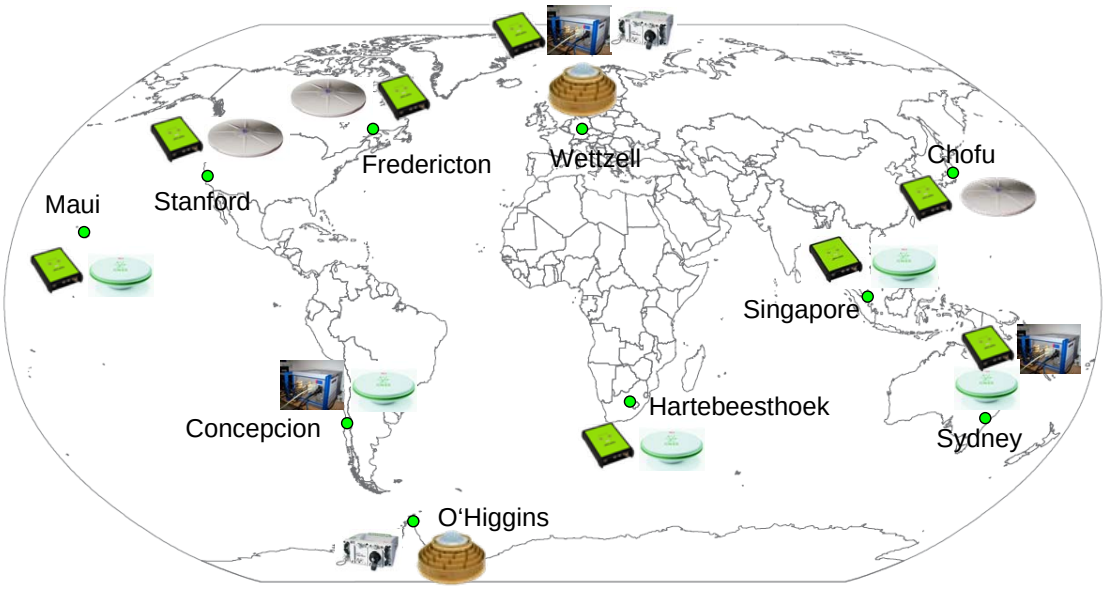

Fig. 3.6: Sites and equipment of the CONGO tracking network in January 2010

The stations in Sydney, Concepcion and Wettzell are equipped with Septentrio's GeNeRx receivers. This type of receiver is used in ESA's GIOVE tracking stations as well and supports tracking of all signals transmitted by the GIOVE satellites. Six configurable channels can be used for tracking the signal on the E1, E5a, E5b and E6 frequencies. Furthermore, the combined E5 signal (AltBOC) can be tracked for one spacecraft. Besides the GIOVE tracking capabilities, the receiver also offers dual-frequency GPS tracking and reports the C/A, P1 and P2 observations for up to 9 satellites. The GeNeRx-receivers used in the CONGO-network have been configured to track GIOVE on the E1[1], E5a and E6 frequency. The stations in O'Higgins (Antarctica) and Wettzell are equipped with a Leica GRX1200+ GNSS receiver. This receiver supports tracking of GPS, GIOVE, GLONASS and SBAS. For GPS, the three frequencies L1, L2 and L5 are supported. For GIOVE, E1, E5a, E5a and E5 (AltBOC) can be tracked. All remaining stations are either equipped with Javad Delta-G2T or -G3TH receivers. The first supports tracking of GPS on three frequencies and GIOVE on two frequencies, namely L1/E1, L2 and L5/E5. The latter additionally offers GLONASS tracking on L1 and L2. At the stations in Wettzell and Sydney, additional receivers have been collocated for testing purposes or as backup.

Besides the receivers, each station must also be equipped with broadband antennas, which allow the reception of the new GPS and Galileo frequencies. The stations in Fredericton (Canada), Chofu (Japan) and Stanford (USA) are equipped with Trimble Zephyr Geodetic II antennas. The station in O'Higgins and Wettzell use the Leica AR25.R3.

[1]It should be noted that the Galileo frequency, which corresponds to L1, is generally denoted E1-L1-E2. For brevity, however, this frequency band is simply referred to here as E1.

These antennas are already upgraded with the additional insert in the antenna's choke ring to avoid significant multipath errors on the L5/E5a-frequency, which have been observed for the unmodified antennas. All other stations are temporarily equipped with Leica AX1203+ GNSS antennas until the upgraded AR25.R3 is available for replacement.

The depth-of-coverage of the CONGO network for the GIOVE satellites is depicted in Fig. 3.7 and represents the state of the network in January 2010. For the plot of the visibility areas, an elevation mask of 10° is used. It becomes obvious that a dual-station visibility is possible for the majority of sub-satellite points. Only small areas close to New Zealand, in the southern part of Africa and in Russia between the Black Sea and Caspian Sea have single-station coverage. The latter two areas may be covered, however, in the near future with an additional station in Addis Ababa (Ethiopia).

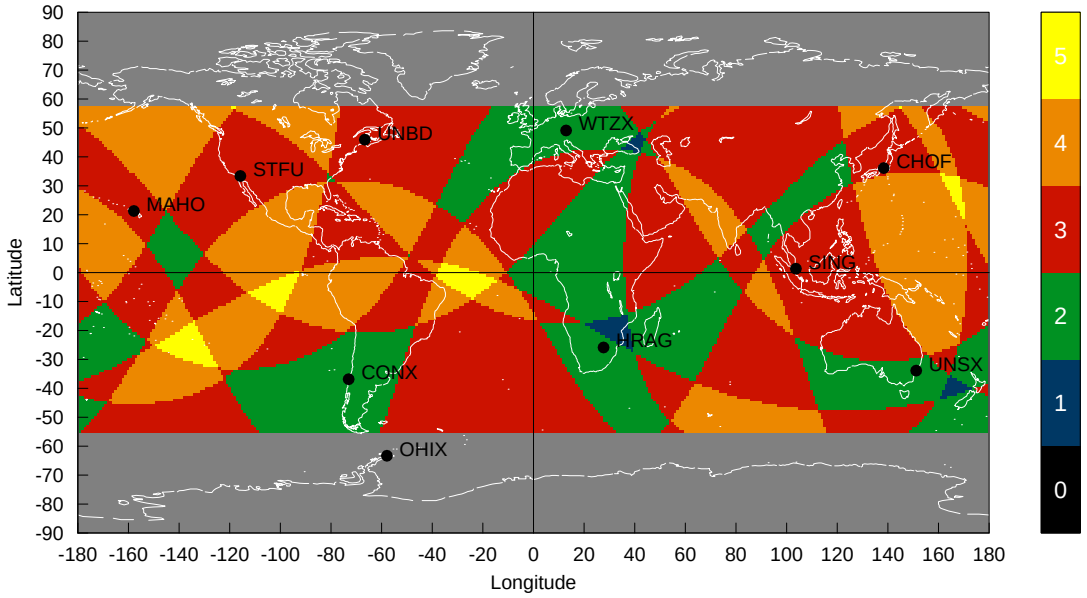

Fig. 3.7: Depth-of-coverage (DOC) of the CONGO-network for GIOVE satellites. Similar to Fig. 3.2, the colorcode indicates the number of stations able to track a GIOVE satellite simultaneously at a certain sub-satellite point. An elevation mask of 10° is used.

The sites of the CONGO network have been selected to achieve global tracking coverage with at least two stations. Restrictions were imposed by the availability of necessary infrastructure, like electricity, housing and high-speed internet connection, which are necessary to setup a real-time tracking station. An extensive performance analysis has been done to optimize the signal quality of each individual station. A careful quality control is especially important for a small network like CONGO with low tracking redundancy. Whereas deficiencies in the measurement quality may be compensated by a high tracking redundancy, like for the IGS GPS tracking network, the products derived from the CONGO observations can be affected by degraded measurements from individual stations. Furthermore, quality control of the state-of-the-art equipment used in the network is important. The experience gained from processing the new GPS- and GIOVE-signals has helped to remove deficiencies in the newly developed equipment.

Tab. 3.2 shows the RMS residuals for the pseudoranges and carrier-phases from mixed GPS and GIOVE PPP solutions over a test period of ten days. It should be considered in the interpretation of the results, that the GIOVE clock solution used for the PPP has a comparably high correlation with the observations of the CONGO stations. Due to the low depth-of-coverage, measurement errors of a single station have a higher impact on the clock estimate. In contrast, the clock estimates of the CODE Rapid prodcuts, which are used for the GPS satellites, have been generated based on a significantly larger station network, which is furthermore completely independent of the CONGO network. As a result, the CODE clock estimates can be considered to be completely uncorrelated from the GPS measurements which have been used in the PPP. Furthermore, only one GIOVE-satellite was transmitting the E1E5a-frequency combination during the selected test interval. Therefore, the amount of data used for the statistics of GIOVE is significantly smaller than for GPS.

Tab. 3.2: Overview of pseudorange and carrier-phase residuals for CONGO stations

	GPS		GIOVE		
Station	PR [m]	CP [mm]	PR [m]	CP [mm]	Receiver Type
CONX	1.07	11	0.82	11	Septentrio GeNeRx1
UNSX	1.10	11	0.98	12	
WTZX	1.73	8	1.17	10	
CHOF	0.87	9	0.60	13	JPS DELTA-G2T
HRAG	0.87	15	0.71	18	
SING	1.02	18	0.81	18	
UNBD	0.77	9	0.45	13	
WTZX	0.76	9	0.64	10	
MAHO	1.04	13	0.70	14	JPS DELTA-G3TH
STFU	0.83	10	0.49	13	
OHIX	0.74	10	0.72	9	Leica GRX1200+ GNSS

The table summarized the residuals for all receivers CONGO tracking stations. The only exceptions are the Leica receiver in Wettzell and the Javad receiver in Sydney, since only a limited amount of observations insufficient for decent statistics was available for them. The results for the GeNeRx1-receivers make obvious, that the pseudorange residuals for GPS are on the order of 1 m. The station in Wettzell has significantly increased residuals. The cause could be identified as far-field multipath originating from a metal roof in the vicinity of the antenna. The GeNeRx receiver turned out to be particularly sensitive to these multipath-errors compared to the other two collocated receivers. As a result, the antenna has been moved to a different position where less multipath reception occurs. The carrier-phase observations for GPS are on the order of 8-11 cm, which fits well to the results found for other receivers from the IGS real-time network as shown in Tab. 3.1.

Most of the Javad receivers show GPS pseudorange residuals between 0.76 m and 0.87 m. The stations in Singapore (SING) and Maui (MAHO), however, exhibit higher residuals on the order of about 1 m, which may be indications for increased multipath-errors at these stations. It should be noted, that the pseudorange observations of the GeNeRx receivers are unsmoothed, whereas the Javad receivers use the carrier-phase observations for an internal smoothing of the observations. The smoothing interval of the Javad receiver is set to 50 s, which allows the elimination of receiver noise and high-

frequency multipath-errors. The carrier-phase residuals for the four stations CHOF, UNBD, WTZX and STFU are close to 10 mm as expected. SING and MAHO, however, exhibit significantly increased residuals with 18 mm and 13 mm, respectively. This is an expected result, since the pseudorange residuals have already indicated multipath problems at these stations. Also, HRAG has increased carrier-phase residuals of 15 mm, even though the pseudorange residuals are not exceptionally high.

The Leica receiver exhibits residuals on the order of 0.70 m, similar to the Javad receivers. However, no pseudorange smoothing is activated for this receiver. The GPS carrier-phase residuals are at 10 mm.

The GIOVE pseudorange residuals are generally lower than the GPS residuals. This effect may be attributed to the increased performance of the new Galileo signals; however, the aforementioned correlation of raw measurements and GIOVE clock estimates will have an effect as well. In can be seen that the same stations, which are affected by multipath for GPS, also have higher residuals for GIOVE. The carrier-phase residuals for the GeNeRx receivers and for the Leica receiver are between 9 mm and 12 mm, which fits well to the values obtained for GPS. The remaining stations, however, have higher carrier-phase residuals between 10 mm and 18 mm. The stations with the highest GPS pseudorange and carrier-phase residuals also have the highest carrier-phase residuals. The comparably high level of carrier-phase residuals for many CONGO stations has not been expected. As a first step to gain more insight into the problem, this analysis should be repeated over a longer test interval when both GIOVE satellites are transmitting on the E1- and E5a-frequencies to gain more data for the statistics.

Due to the limitations caused by the availability of only one GIOVE satellite compared to about 30 GPS satellites and the correlation of the GIOVE clock offsets with the measurements, it is not possible to draw a conclusive statement concerning the measurement quality of GIOVE. However, three stations of the network with increased residuals for GPS and GIOVE observations have been identified. A detailed investigation of these stations should be conducted in the future. Similar to WTZX, a movement of the antenna on site may already improve the performance of the affected stations.

4. Real-Time Clock Estimation

This chapter presents the real-time clock estimation procedure in depth. It begins with an overview of the RETICLE system, followed by an introduction of the basic measurement equations for GNSS observables. All required models for the representation of the observations are presented. A derivation of the necessary equations used to set up the Kalman filter follows.

4.1 RETICLE Overview

The real-time clock-estimation system (RETICLE) developed within this thesis comprises a Kalman filter, which is the core algorithm of the system, together with several functions, which handle the retrieval of real-time measurement and other auxiliary data. In this section, an overview of the system will be provided.

Fig. 4.1 depicts a schematic of the complete system, showing all required inputs for the system on the left side, the Kalman filter loop in the center and the output of the system on the right side. RETICLE is set up on a Linux system. The main algorithm is programmed in C++, while other, auxiliary processes, for example data retrieval from ftp-servers, are realized as shell-scripts. The backbone of the system is RODOS, a software package providing basic real-time functionalities like threading and periodic task execution. RODOS has emerged from its predecessor BOSS, which served as the operating system on a small-satellite mission [Montenegro and Richardson, 2009]. Similar to the operating system of a satellite, the RETICLE system has many different functionalities, which must be executed repeatedly at fixed time intervals. Examples are the retrieval of the input data, output of filter results and last but not least the update of the employed Kalman filter. These tasks are implemented as threads, a class provided by the RODOS system. The different tasks do not have equal importance for the clock estimation process. The retrieval of measurement data has, for example, higher priority than the update of Earth-rotation parameters. Therefore, the different processes, or threads, have a different priority in the system. If a low-priority thread is keeping the system busy, but a high-priority thread is scheduled for immediate execution, the real-time operating system stops the low-priority thread and does not resume it until the high-priority is finished. If, however, a thread, which is responsible for retrieving data, writes this data into a shared storage, it must not be interrupted by other threads, which may read the same information from the data storage. Therefore, the interruption of threads must also be prohibited. The RODOS system provides all of the above functionalities.

The Kalman filter processes measurements received from a global network of GPS reference stations. An overview of the network has already been given in Chap. 3. RE-

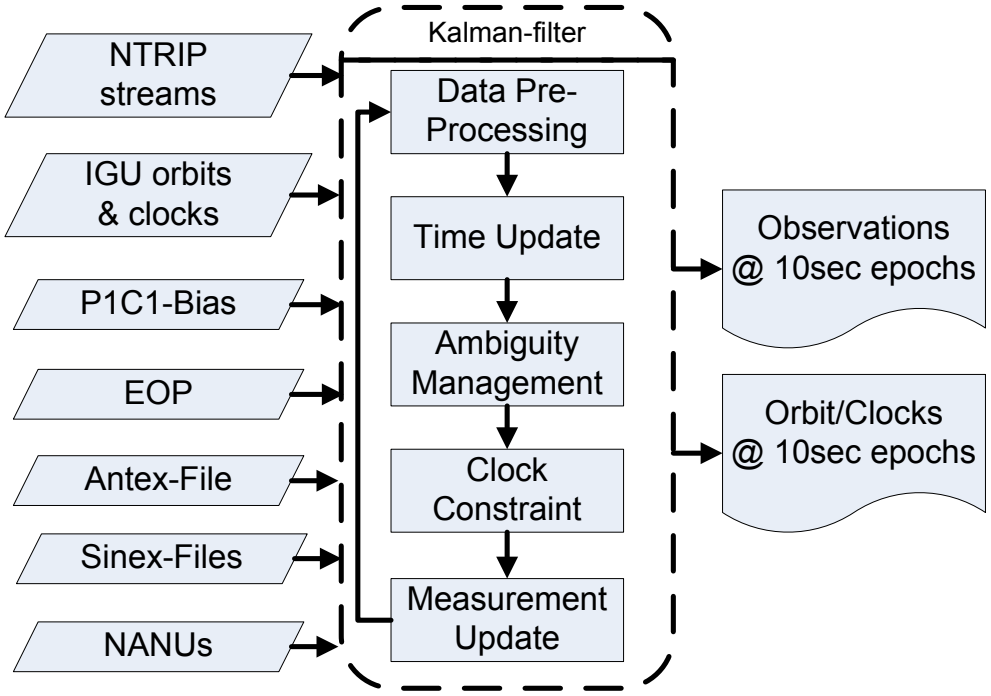

Fig. 4.1: Overview of the RETICLE-System depicting the system inputs on the left side, the Kalman filter core process and the output data on the right side

TICLE reduces the stations' measurement-rate from 1 Hz to 10 second epochs, which are stored in an internal buffer for access by the Kalman filter and additionally recorded in Rinex-files. These Rinex-files can be used for post-processing of the real-time data.

The predicted part of the IGS ultra-rapid (IGU) orbits and clocks is used for initialization of the clock offsets and rates in the filter states. The IGU product contains orbit and clock data for an interval of 48 hours. The first half of the data is computed from actual measurements and the second half are predicted orbit and clocks. Currently, the update rate of the product is four times daily at 3 h, 9 h, 15 h and 21 h UTC with a latency of 3 hours relative to the last observation. Because the accuracy of the clock predictions significantly reduces with an increasing age of data, the most recent available product should be used. In RETICLE, the IGU product is downloaded and concatenated four times each day. In order to reduce discontinuities in the orbits and clocks caused by the concatenation, the old product is faded out and the new product is faded in by a cosine-weighted interpolation.

The differential code biases (DCBs) between the P1 and C1 observables will be introduced in Sec. 4.2.6. Due to the slow change in time of these parameters, the update rate has been reduced to once a week in RETICLE. The DCBs are retrieved via FTP-protocol from the Center for Orbit Determination in Europe (CODE). CODE provides estimations of the DCBs with a moving average over 30 days [Schaer and Steigenberger, 2006].

The most recent predicted Earth-orientation-parameters (EOP) are downloaded via ftp from the IGS. These parameters are necessary for the computation of the transformation from the inertial to the Earth-fixed reference frame. Almost all computations

in the clock estimation application are performed in the Earth-fixed frame directly. The only exception is the computation of the Earth tides and polar tides in the precise station modeling, which is described in Sec. 4.2.1.

The Antex file contains the phase center corrections for all GPS satellite antennas and reference-station antennas as explained in Sec. 4.2.4. These files are provided by IGS and are updated whenever new satellites are launched or new antennas for ground stations are available. The Antex-files are therefore only downloaded manually on demand. For users of the RETICLE clock products it is crucial for consistent processing to utilize the same definitions for the satellites' antenna offsets.

The most recent Notice Advisories to Navstar Users (NANUs) are a very important information for the RETICLE system. GPS satellites frequently undergo orbital maneuvers or maintenance. During or after the maneuver and prior to the availability of a new, updated IGU orbit product, the orbit information of the affected satellite is no longer valid. During maintenance periods, the atomic frequency standards on board the satellite may be manipulated or switched, leading to clock jumps or abnormal clock behavior, which could also disturb the clock estimation process. Even though it is agreed practice for the IGS to also include unhealthy satellites in their precise ephemerides, a lesson learned from the operation of the real-time clock estimation system is, that the problems these satellites cause in the filter exceed the benefits, which users may have by keeping them included. For the sake of robustness of the clock estimation, unhealthy satellites are excluded from the filter during maintenance and maneuver periods and, in the latter case, even beyond until valid predicted orbit information is available again. NANUs contain information about planned outages and are issued for civilian users by the U.S. Coast Guard Navigation Center (NAVCEN) prior to the events [U.S. Coast Guard Navigation Center, 2009].

The estimated GPS clock offsets are stored in a daily SP3 file. This file can be extracted from the system at any time and directly used for near real-time applications like precise orbit determination of LEO satellites. In addition, the GPS orbits and clocks are also provided for remote users via different sources. The recorded SP3 files are uploaded to a FTP-server every 5 minutes, which is publicly accessible. Historic products are stored for up to one week. Furthermore, the products are disseminated via NTRIP-streams from a dedicated caster. These streams are primarily intended for applications with low latency-requirements. Two different formats are supported: The first is the native SP3 format, which is transmitted in plain ASCII. The most recent 8 epochs are transmitted at once for two reasons: Firstly, to provide the user with the necessary data for orbit and clock interpolation and, secondly, to ensure redundancy in case of interruptions in the internet connection. This stream has a data rate of approximately 1600 bytes/s. The second source is a binary data stream in RTCM3 format, employing the latest proposed messages for orbit and clock corrections. These binary state space representation (SSR) messages transmit corrections to the satellite position in the radial, along-track and cross-track directions and the satellite clock offset for a given epoch. The IODE is also transmitted to unambiguously identify the corresponding issue of the broadcast ephemeris for the correction values. Using the broadcast ephemerides (BCEs) provided by the user's receiver, the precise orbit and clock information can than be reconstructed for all tracked satellites. Alternatively, RETICLE also provides a dedicated

stream with the most recent broadcast ephemerides in RTCM3-format. Users receiving the SSR-stream and the BCE-stream simultaneously can then even reconstruct a globally valid orbit and clock product. In addition, the state space messages allow the transmission of signal biases, which allow the user to use the clock information consistently with other signal combinations than the ones used for their generation (see Sec. 4.2.6). Due to the high compression, the data rate of the SSR stream is as low as 100 bytes/s [RTCM, 2009].

4.2 Modeling of GNSS Observations

The precise modeling of the pseudorange and carrier-phase observations is a key requirement for all GNSS applications, where high accuracies are desired. This section introduces the measurement equations including all corrections for precise modeling, beginning with the pseudorange, based on the guideline provided by Kouba [2009].

If dual-frequency GNSS data is available from a reference station, the ionospheric delay on the pseudorange and carrier-phase measurements can be eliminated to first order. The second-order effects of the ionospheric delay for a satellite at zenith can vary between 0-2 cm, depending on the epoch, the solar activity and the user position on the Earth [Bassiri and Hajj, 1993]. The ionosphere-free combination of pseudorange and carrier-phase of the signals A and B, $\rho_{\mathrm{IF(A,B)}}$ and $\Phi_{\mathrm{IF(A,B)}}$, respectively, are formed according to:

$$\rho_{\mathrm{IF(A,B)}} = a_{\mathrm{A}}\rho_{\mathrm{A}} + a_{\mathrm{B}}\rho_{\mathrm{B}} \tag{4.1}$$

$$\Phi_{\mathrm{IF(A,B)}} = a_{\mathrm{A}}\Phi_{\mathrm{A}} + a_{\mathrm{B}}\Phi_{\mathrm{B}} \tag{4.2}$$

ρ_{A}, ρ_{B}, Φ_{A} and Φ_{B} are pseudorange and carrier-phase observables. a_{A} and a_{B} are the linear factors of the corresponding signals. They are found from:

$$a_{\mathrm{A}} = \frac{f_{\mathrm{A}}^2}{f_{\mathrm{A}}^2 - f_{\mathrm{B}}^2} \tag{4.3}$$

$$a_{\mathrm{B}} = \frac{-f_{\mathrm{B}}^2}{f_{\mathrm{A}}^2 - f_{\mathrm{B}}^2} \tag{4.4}$$

where f_{A} and f_{B} are the frequencies of the GNSS-signal in the band A and B, respectively. These frequencies could be any combination of the available signals, for example L1 and L2 for GPS or E1 and E5a for Galileo. The linear factors have the property that $a_{\mathrm{A}} + a_{\mathrm{B}} = 1$, which ensures that the geometry of the observations is maintained. Note that in the following sections, the pseudorange and carrier-phase measurement equations always refer to an ionosphere-free combination. For simplicity, the subscript $_{\mathrm{IF(A,B)}}$ is therefore dropped from here on.

The ionosphere-free linear combination ρ of pseudorange measurements from a GPS antenna n to a GPS satellite s relates to the real range according to:

$$\begin{aligned}\rho_n^{(s)} =& |\boldsymbol{r}^{(s)} - \boldsymbol{r}_n| + c\left(\delta t_n - \delta t^{(s)}\right) + c\delta t_{\mathrm{rel}} + T_n^{(s)} \\ &+ b_{\mathrm{rcv,IF(A,B)}} + b_{\mathrm{sat,IF(A,B)}} + b_{\mathrm{PCO}} + b_{\mathrm{PCV}} + \varepsilon_n^{(s)}\end{aligned} \tag{4.5}$$

In this equation $\boldsymbol{r}^{(s)}$ is the position vector of the GPS satellite and $\boldsymbol{r}_n$ is the position vector of the ground station antenna reference point. The unknown clock offsets of the receiver clock and GPS satellite clock are denoted δt_n and $\delta t^{(s)}$, respectively, and are multiplied with the speed of light c. The relativistic correction δt_{rel} is also multiplied with c to ensure units of length. The errors due to the signal delay in the troposphere is denoted by T. The terms $b_{\mathrm{rcv,IF(A,B)}}$ and $b_{\mathrm{sat,IF(A,B)}}$ are receiver- and satellite-dependent code bias corrections. It is necessary, for example, for ground stations with receivers omitting the P1-code observable. The biases b_{PCO} and b_{PCV} correct for phase center offsets and elevation-dependent phase center variations of transmitting and receiving antennas. Finally, the term ε represents the combined errors due to multipath and receiver noise for the pseudorange measurements. A thorough review of these measurement errors and biases together with an introduction of the used models will follow in subsequent sections.

Next, the equation for the carrier-phase measurements shall be introduced. These measurements differ from the pseudorange since the receiver can only measure the fractional part of a carrier-phase cycle directly. The changes in the distance between satellite and antenna, which exceed one complete cycle, are taken into account by the receiver in the generation of the carrier-phase measurement. Thus, the measurement consists of the actual fractional part of the cycle and the accumulated integer cycle count. Usually the GPS receivers' standard output format of the integrated carrier-phase has the dimension of cycles. Multiplication with the corresponding wavelength of the tracked signal λ converts it to the more convenient dimensions of lengths. Note that in the notation throughout this text, the dimension of the carrier-phase measurement Φ is always in meters. Using the carrier-phase poses an additional challenge, since the receiver cannot determine the number of cycles N between the antenna and the GPS satellite at the beginning of the tracking. Therefore the ionosphere-free phase range measurement is ambiguous by an ambiguity A, which consists of a linear combination of the integer ambiguities:

$$A = a_A \lambda_A N_A + a_B \lambda_B N_B \tag{4.6}$$

Note that in this equation, the integer ambiguities N have been multiplied with the corresponding wavelength, leading to a dimension of length for A. With this derivation, the measurement equation for the ionosphere-free carrier-phase observations is shown in Eq. 4.7:

$$\begin{aligned} \Phi_n^{(s)} =& |\boldsymbol{r}^{(s)} - \boldsymbol{r}_n| + c\left(\delta t_n - \delta t^{(s)}\right) + c\delta t_{rel} + T_n \\ &+ b_{PWU} + b_{PCO} + b_{PCV} - A_n^{(s)} + \varepsilon_n^{(s)} \end{aligned} \tag{4.7}$$

The float ambiguity A remains fixed as long as the GPS satellite is continuously tracked. However, interruptions of the carrier tracking on either of the frequencies in the linear combination cause the receiver to miscount the accumulated integer cycles, which is referred to as a cycle slip. If a cycle slip occurs, the ambiguity of the carrier-phase observation has a discontinuity, which must be handled properly for consistent processing of the observations.

Note that the differential code bias from Eq. 4.5 is not present here. Instead a carrier-phase wind-up correction b_{PWU} is applied. In the following subsections, the

models used for the pseudorange and carrier-phase observations are described in more detail.

4.2.1 Reference Station Position

The position vector $\boldsymbol{r}_n$ of the ground station in the Earth-centered Earth-fixed (ECEF) coordinate frame is based on the position $\tilde{\boldsymbol{r}}_n$ of the corresponding geodetic marker and several correction terms. The marker position varies slowly on the order of centimeters per year due to tectonic plate motion. Earthquakes can cause discontinuities in this motion, however. In order to make sure that the proper station position is used in the clock estimation and discontinuities are correctly regarded, the information is taken from Sinex-files, which are issued by IGS and updated regularly each week. For stations, which are not part of the IGS network, PPP positioning solutions using precise GPS orbit and clock products are independently computed.

The first correction is the eccentricity vector $\Delta\boldsymbol{r}_{\mathrm{ecc}}$, which represents the vector from the geodetic marker to the antenna reference point. The eccentricity vector is a constant value, which changes only if the station configuration is modified and can be found in the Sinex-files. Additionally, three terms are applied which vary on a short time-scale: the corrections due to solid Earth tides $\Delta\boldsymbol{r}_{\mathrm{ET}}$, ocean loading $\Delta\boldsymbol{r}_{\mathrm{OL}}$ and polar tides $\Delta\boldsymbol{r}_{\mathrm{PT}}$. The solid Earth tides are cased by the gravitational pull of the sun and the moon, which deform the Earth's crust. The variation in the horizontal direction is usually on the order of a decimeter. In the radial direction, it can be on the order of several decimeters [Xu and Knudsen, 2000]. The ocean loading displacement results from the varying pressure of the oceans on the coastlines and on the ocean bed, which also deforms the Earths crust. The effect is smaller than the solid Earth tides, but can reach magnitudes up to several centimeters near the coast [Dragert et al., 2000]. Finally, the slow variation of the Earth's spin axis with respect to the crust changes the centrifugal potential. The resulting station displacement reaches several centimeters in the radial direction and several millimeters in horizontal direction [Kouba, 2009]. The modeling of these displacements is described by McCarthy and Petit [2004]. The station position vector is written as the sum of all previous position vectors and correction terms in the following form:

$$\boldsymbol{r}_n = \tilde{\boldsymbol{r}}_n + \Delta\boldsymbol{r}_{\mathrm{ecc}} + \Delta\boldsymbol{r}_{\mathrm{ET}} + \Delta\boldsymbol{r}_{\mathrm{OL}} + \Delta\boldsymbol{r}_{\mathrm{PT}} \tag{4.8}$$

4.2.2 Relativistic Correction

The correction term due to relativistic effects in Eq. 4.5 and Eq. 4.7, respectively, consists of two components. The first component $\delta t_{\mathrm{rel,p}}$ accounts for the periodic change in the GNSS satellite clock rate as the satellites trajectory deviates from its nominal circular orbit. This correction can amount to several meters and is computed according to:

$$\delta t_{\mathrm{rel,p}} = -2\frac{\boldsymbol{r}\cdot\boldsymbol{v}}{c^2} \tag{4.9}$$

In this equation, $\boldsymbol{r}$ and $\boldsymbol{v}$ are the satellite's position and velocity in the Earth-centered Earth-fixed frame [GPS-ICD-200c, 1993; Kouba, 2002].

The second part is due to the space-time curvature correction and is denoted as $\delta t_{\mathrm{rel,sct}}$. In the presence of the Earth's gravitational field, the GNSS signal does not travel on the direct way from the satellite to the user. Instead the signal-path is curved, which increases its length. For a receiver on the Earth's surface or on a LEO orbit, this increase in the path length amounts to between 1 and 2 cm, depending on the elevation of the GPS satellite [Bahder, 2003]. This correction is computed according to:

$$\delta t_{\mathrm{rel,sct}} = 2\frac{\mu_{\oplus}}{c^3} \cdot \log\left(\frac{|\boldsymbol{r}_n| + |\boldsymbol{r}^{(s)}| + |\boldsymbol{r}_n - \boldsymbol{r}^{(s)}|}{|\boldsymbol{r}_n| + |\boldsymbol{r}^{(s)}| - |\boldsymbol{r}_n - \boldsymbol{r}^{(s)}|}\right) \tag{4.10}$$

In the previous equation, $\mu_{\oplus}$ denotes the gravitational constant of the Earth. The antenna and satellite position vectors $\boldsymbol{r}_n$ and $\boldsymbol{r}^{(s)}$, respectively, have already been introduced. The complete relativistic correction in Eq. 4.5 and Eq. 4.7 is then found from:

$$\delta t_{\mathrm{rel}} = \delta t_{\mathrm{rel,per}} + \delta t_{\mathrm{rel,sct}} \tag{4.11}$$

4.2.3 Tropospheric Correction

Unlike the ionospheric delay, the tropospheric delay of GNSS signals in the atmosphere is non-dispersive. Therefore all frequencies experience the same delay, which depends on the atmospheric conditions along the raypath. The delay can amount from 2.4 m in zenith-direction to about 25 m at low elevations. For modeling, the delay is often split up into the dry component, which results from the dry air, and the wet component, which depends on the water vapor content of the atmosphere. Furthermore, both the wet and the dry delay are usually modeled as the delay in the zenith direction multiplied with a mapping function, which yields the following basic equation for the tropospheric delay T:

$$T = M_d D_d + M_w D_w \tag{4.12}$$

where M_d and M_w are the dry and wet mapping functions, respectively. D_d and D_w are the dry and wet delays in the zenith direction [Kaplan, 2006].

The zenith path delays can be computed from empirical equations, which depend on five parameters: total pressure, temperature and water vapor content (all referred to sea level) as well as the temperature lapse rate and the average decrease of water vapor with height. The latter two parameters describe the change of pressure, temperature and water vapor content with height [Smith, 1966]. If meteorological measurements are not available, models of the standard atmosphere must be used to gain the necessary data. An accurate model for the tropospheric path delays D_d and D_w is the UNB3 model, which has been developed at the University of New Brunswick. In this model, the five meteorological parameters are interpolated depending on the latitude of the user position. Furthermore, seasonal variations are accounted for [Collins et al., 1996]. The UNB3-model has been updated to the more precise model UNB3m, which exhibits a reduced mean error of the modeled tropospheric delay [Leandro et al., 2006].

The Niell mapping functions are used to map the zenith path delays to the actual raypath according to the antenna-satellite-geometry. The mapping function M_d for the dry component depends on the location of the user antenna, the satellite elevation and the epoch, whereas the wet mapping function M_w depends only on user antenna location and satellite elevation [Niell, 1996].

In general, the models for the dry delay, which accounts for about 90 % of the total delay, are more accurate than the models for the wet delay due to uncertainties in the distribution of water vapor in the atmosphere [Kaplan, 2006]. In order to account for these deviations from the true conditions, a differential zenith path delay dT_n is estimated for each station and appears in the state vector of the Kalman filter. The differential zenith path delay is then mapped into a differential tropospheric slant delay, using the Niell's mapping function for the wet delay M_w, which depends on the elevation of the satellite with respect to the user position. Thus, the complete tropospheric correction T_n in Eq. 4.5 and Eq. 4.7 is found from:

$$T_n = T_{n,\mathrm{UNB3}} + M_w dT_n \tag{4.13}$$

where $T_{n,\mathrm{UNB3}}$ denotes the complete delay computed according to Eq. 4.12 using the UNB3 model and Niell's mapping functions.

4.2.4 Antenna Phase Center Correction

Contrary to the broadcast ephemerides, where the satellite position refers to the antenna reference point (ARP), the IGS orbit products refer to the center of mass of the spacecraft. Therefore, users must correct for this offset, when modeling GNSS observations with IGS products. The two terms b_{PCO} and b_{PCV} in Eq. 4.5 and Eq. 4.7 represent the corrections due to phase center offset (PCO) and phase center variations (PCV), respectively, and combine the corrections for the transmitting (satellite) antenna and the receiving (station) antenna. For precise positioning, the phase center of an antenna can no longer be defined as a fixed point, because elevation- and azimuth-dependent phase reception patterns must be taken into account. Therefore, each GPS antenna is characterized using a constant phase center offset and an elevation- and azimuth-dependent part. The phase center offset is a constant vector, which originates at the antenna reference point and may differ for the individual frequencies of the antenna. The scalar value for phase center offset correction for a single frequency is found from the dot-product of the phase center offset vector and the unit line-of-sight vector $\hat{\boldsymbol{e}}_n^{(s)}$ from the antenna reference point to the GPS satellite position:

$$b_{\mathrm{PCO}} = \hat{\boldsymbol{e}}_n^{(s)} \cdot \boldsymbol{b}_{\mathrm{PCO}} \tag{4.14}$$

In addition to the constant phase center offset, the elevation- and azimuth-dependent correction for the phase-center variation b_{PCV} is used as well. It is obtained by interpolation from a table, which holds the necessary information in an elevation-azimuth-grid. In order to be consistent with the ionosphere-free data combination, the phase center offset and phase center variation correction for both frequencies must of course be weighted with the corresponding coefficients [Schmid et al., 2007].

Since November 5, 2006, the IGS has adopted a new convention for the use of phase center offsets and phase center variation for transmitting and receiving antennas. Prior to this date, satellite-block-dependent phase center offsets have been used, but no phase center variations. The new convention defines individual phase center offsets for each satellite. The phase center variations depend on the satellite block-type only and are axis-symmetric to the boresight vector. Both PCO and PCV for each satellite are

identical for the L1 and L2 frequency. The ground station antennas are calibrated in a similar manner with antenna-specific PCO and PCV. The latter is in general elevation- and azimuth-dependent. However, sometimes only elevation-dependent phase center variations are available. It should furthermore be noted that the PCO and PCV also depend on the radome used for the antenna. The Antex-files from IGS hold the PCO- and PCV-data for all antennas currently used in the IGS network as well as for the current and past satellite antennas. The plots in Fig. 4.2 and Fig. 4.3 show the phase center variations for the Leica AR25 R3 antenna without a radome and a Block-IIR satellite antenna, respectively. The plots have been generated from the IGS Antex file for GPS week 1570. Fig.4.2 plots the variations from the zenith direction down to an elevation of 0°. It becomes obvious that the elevation-dependent variations range from approximately 15 mm to about -10 mm. The azimuthal variations are much smaller and hardly noticeable in the plot. Fig. 4.3 depicts the phase center variations for Block-IIR satellites, which have per definition no azimuthal variations. The magnitude of the elevation-dependent variations is similar to the Leica antenna. It should be noted that the transmitting antennas are only calibrated over a boresight-angle range from 0° to 14°, which corresponds to elevation angles between 90° and 76°, respectively.

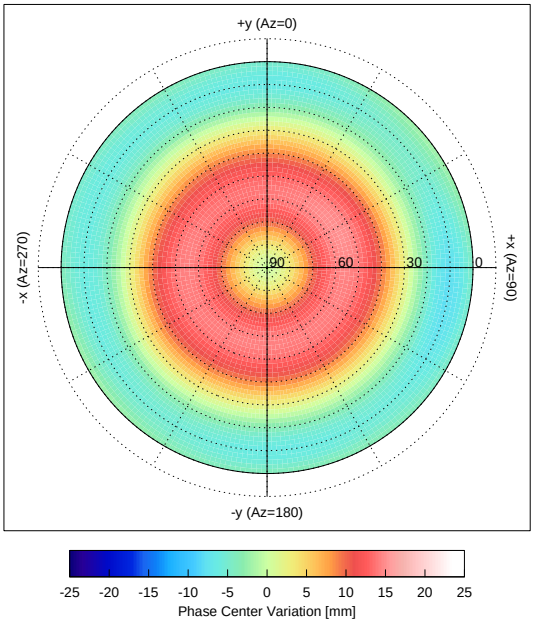

Fig. 4.2: Azimuth- and elevation-dependent phase center variations for Leica AR25. R3 antenna without a radome for the ionosphere-free combination from L1 and L2

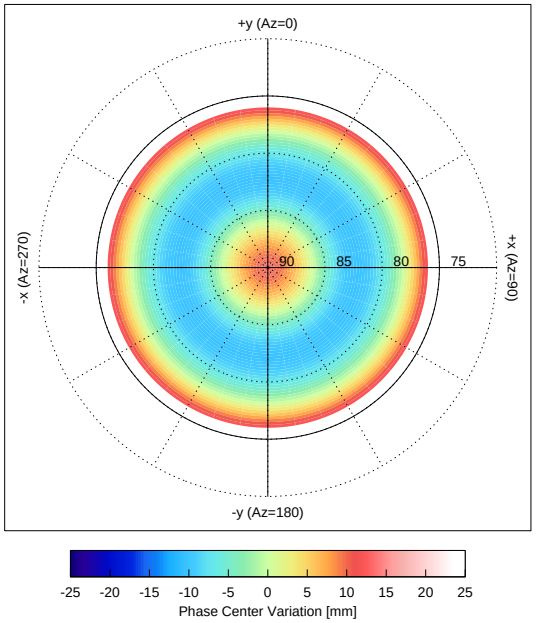

Fig. 4.3: Elevation-dependent phase center variations for Block-IIR satellites for the ionosphere-free combination from L1 and L2. The plot shows the variations for elevations from 90° to 76° , which corresponds to boresight angles from 0° to 14° .

4.2.5 Phase Wind-Up Correction

The correction b_{PWU} is due to the phase wind-up phenomenon of a circular-polarized electromagnetic wave, which manifests itself in an apparent change in the observed

carrier-phase, if the transmitting or receiving antennas are rotating about their boresight vectors with respect to each other. When processing measurements from a ground station network, the receiving antennas are of course fixed with respect to the Earth-fixed frame. However a GNSS satellite slowly changes its attitude to keep the solar panels pointed to the sun. As a result, the transmitting antenna rotates with respect to the receiving antenna. For precise modeling of the carrier-phase measurements, the correction term is applied in Eq. 4.7.

The wind-up phenomenon of the carrier-phase has been thoroughly discussed by Wu et al. [1993] and shall only briefly be repeated here. An antenna is described using two orthogonal unit-vectors, $\hat{\boldsymbol{n}}$ and $\hat{\boldsymbol{m}}$, which point into the directions of the antenna's two dipole-elements. If $\hat{\boldsymbol{k}}$ is the unit vector pointing from the transmitting antenna to the receiving antenna, the effective dipole of the receiving antenna can be found from:

$$\boldsymbol{D} = \hat{\boldsymbol{m}} - \hat{\boldsymbol{k}} \left(\hat{\boldsymbol{k}} \cdot \hat{\boldsymbol{m}} \right) + \hat{\boldsymbol{k}} \times \hat{\boldsymbol{n}} \tag{4.15}$$

Vice versa, the corresponding definition can also be found for the transmitting antenna:

$$\boldsymbol{D}' = \hat{\boldsymbol{m}}' - \hat{\boldsymbol{k}} \left(\hat{\boldsymbol{k}} \cdot \hat{\boldsymbol{m}}' \right) - \hat{\boldsymbol{k}} \times \hat{\boldsymbol{n}}' \tag{4.16}$$

The phase wind-up correction can now be computed from

$$b_{PWU} = sign\left(\zeta\right) acos\left(\frac{\boldsymbol{D}' \cdot \boldsymbol{D}}{|\boldsymbol{D}'| \cdot |\boldsymbol{D}|} \right) \tag{4.17}$$

with ζ being defined as

$$\zeta = \hat{\boldsymbol{k}} \cdot \left(\boldsymbol{D}' \times \boldsymbol{D} \right) \tag{4.18}$$

It should be noted that the phase wind-up correction in Eq. 4.17 is only a fractional correction and does not account for a roll-over of ionosphere-free carrier-phase cycles. As this roll-over has the same effect as a carrier-phase cycle slip, it can most conveniently be compensated for by re-initializing the carrier-phase ambiguity A in the estimation. However, since continuous use of the carrier-phase observable is desirable to increase the precision of the clock estimation, the ambiguity in Eq. 4.7 should be adjusted by one ionosphere-free cycle if the roll-over occurs.

4.2.6 Code Bias Correction

The GPS clock offset estimates provided by RETICLE are consistent with the ionosphere-free combination of the P1 and P2 signal according to the IGS convention. However, quite often these observations are not available, for example if the data-format used to stream the receiver measurements is limited to only one pseudorange observation per frequency. In this case the P1 observable is dropped in favor of C1. Furthermore, some receivers do not support the output of the P1 observable at all. If the data combination is formed from different observations, code bias corrections must be applied, which consist of a satellite- and receiver-dependent part and are denoted $b_{\mathrm{sat,IF(A,B)}}$ and $b_{\mathrm{rcv,IF(A,B)}}$, respectively, in Eq. 4.5. For notational convenience, the ionosphere-free linear combination of two signals A and B will be referred to by IF(A,B) in the text and

the equations from now on. In the following, the code biases are introduced in further detail and related to the differential code biases, provided by the CODE analysis center, for example.

A single frequency pseudorange observation ρ_A is related to the ionosphere-free linear combination of the GPS P1 and P2 observation $\rho_{\mathrm{IF(P1,P2)}}$ as follows:

$$\rho_A = \rho_{\mathrm{IF(P1,P2)}} + I_A + CB_{\mathrm{rcv,A}} + CB_{\mathrm{sat,A}} \tag{4.19}$$

where the parameter I_A denotes the ionospheric delay of the signal A. It is found from $I_A = \frac{40.3 \cdot \mathrm{TEC}}{f_A^2}$, where f_A is the frequency corresponding to the signal A and TEC is the total electron content in a tube along the transmission path from the satellite to the receiver with 1 m^2 cross-section [Misra and Enge, 2001]. The code biases $CB_{\mathrm{rcv,A}}$ and $CB_{\mathrm{sat,A}}$ are receiver- and satellite-dependent code biases of the signal A with respect to the ionosphere-free combination. As the name implies, the satellite-dependent bias is different for each satellite, but it would be identical for a second receiver observing the same satellite on the same signal. The receiver-dependent bias is equal for the observations of all satellites on the same signal for this receiver, but is different for a second receiver observing the same satellite. If Eq. 4.19 is used to form the ionosphere-free combination using $\rho_{\mathrm{IF(A,B)}} = a_{\mathrm{A}}\rho_{\mathrm{A}} + a_{\mathrm{B}}\rho_{\mathrm{B}}$ the following expression is obtained:

$$\begin{aligned}\rho_{IF(A,B)} =& \rho_{\mathrm{IF(P1,P2)}} \\ &+ a_{\mathrm{A}}(CB_{\mathrm{rcv,A}} + CB_{\mathrm{sat,A}}) + a_{\mathrm{B}}(CB_{\mathrm{rcv,B}} + CB_{\mathrm{sat,B}})\end{aligned} \tag{4.20}$$

The receiver- and satellite-dependent bias terms can now be combined into the two terms $b_{sat,IF(A,B)}$ and $b_{rcv,IF(A,B)}$, which appear in Eq. 4.5:

$$b_{\mathrm{sat,(A,B)}} = a_A CB_{\mathrm{sat,A}} + a_B CB_{\mathrm{sat,B}} \tag{4.21}$$

$$b_{\mathrm{rcv,(A,B)}} = a_A CB_{\mathrm{rcv,A}} + a_B CB_{\mathrm{rcv,B}} \tag{4.22}$$

If the P1 and P2 signals are substituted for A and B, respectively, in Eq. 4.20, the code biases must vanish, of course, which means that $b_{\mathrm{sat,IF(P1,P1)}} = 0$ and $b_{\mathrm{rcv,IF(P1,P2)}} = 0$ Obviously, one possibility to satisfy these conditions is:

$$CB_{\mathrm{sat,P2}} = -\frac{a_{\mathrm{L1}}}{a_{\mathrm{L2}}} CB_{\mathrm{sat,P1}} \tag{4.23}$$

$$CB_{\mathrm{rcv,P2}} = -\frac{a_{\mathrm{L1}}}{a_{\mathrm{L2}}} CB_{\mathrm{rcv,P1}} \tag{4.24}$$

At this point the definition of the differential code bias shall be introduced, which is defined as the difference between two code biases on different signals:

$$DCB_{(A,B)} = CB_A - CB_B \tag{4.25}$$

This definition holds both for the receiver-dependent and satellite-dependent bias, however, the corresponding indices have been omitted here. Using Eq. 4.25 with Eq. 4.24 leads to definition of the code biases in terms of the $DCB_{\mathrm{(P1,P2)}}$:

$$CB_{\mathrm{sat,P1}} = a_{\mathrm{L2}} DCB_{\mathrm{sat,(P1,P2)}} \tag{4.26}$$

$$CB_{\mathrm{sat,P2}} = -a_{\mathrm{L1}} DCB_{\mathrm{sat,(P1,P2)}} \tag{4.27}$$

The same definitions hold also true for the receiver-dependent biases. Using Eq. 4.25 and Eq. 4.26, the code bias for the C/A-code can also be found:

$$CB_{\mathrm{sat,C1}} = a_{\mathrm{L2}} DCB_{\mathrm{sat,(P1,P2)}} - DCB_{\mathrm{sat,(P1,C1)}} \tag{4.28}$$

The derived values correspond to the biases of the individual C1, P1 and P2 observations with respect to the ionosphere-free observations. They can be used by single frequency users, who must apply bias corrections when using the satellite clock corrections. It is interesting to note that the P1-code bias derived in Eq. 4.26 is equivalent to the GPS group delay value (T_{GD}), which is transmitted in the broadcast ephemerides for single frequency users [Simsky and Sleewaegen, 2004]. They can also be used to process observations from different signals consistently with the ionosphere-free P1-P2-clocks. This is important, when clock offsets must be estimated according to the IGS convention even if the required signals are not available. When applied to the modeling of dual-frequency measurements with Eq. 4.21 and Eq. 4.22, the contribution of the P1P2-DCB drops out of the equations. Though this derivation appears cumbersome if only the dual-frequency application is regarded, advantage is that the same biases can be used by single-frequency and dual-frequency users. This versatility becomes important for the new RTCM3 state-space-messages. A dedicated message is forseen for the transmission of individual code biases for each signal, which should be valid for both dual- and single-frequency applications [RTCM, 2009]. Obviously, knowledge of differential code biases is required for the computation of the corrections. Solutions for the P1C1-DCB and the P1P2-DCB, which are computed from a sliding average of 30 days, are available from the CODE analysis center [Schaer and Steigenberger, 2006]. The satellite- and receiver-dependent biases required for processing the new L2C-signals, which are broadcast by Block-IIR satellites, are not yet provided routinely by an analysis center.

It should furthermore be noted that the corrections for the receiver-dependent biases can be dropped in certain cases, for example when the C/A code is used in place of the P1 consistently for all observations. In this case, these biases will be absorbed into the receiver clock offset estimate like all other common biases on the observations. However, the receiver-dependent biases become important when mixed observation types are used. Example are the aforementioned new L2C observations or processing of observations from constellations other than GPS. In the following, the necessary biases for consistent processing of GIOVE observations shall be introduced.

Similar to the GPS satellite, the estimated GIOVE satellite clocks are also referred to an ionosphere-free linear-combination of two signals. For the clock generation based on the measurements from the CONGO-network, the combined signal from data and pilot tracking on the E1 and the E5a frequency have been selected, since they are tracked by all three receiver-types in the network. The Rinex3 signal identifiers are C1X and C5X, respectively. However, the signals are denoted as E1X and E5X in the following to emphasize the fact that they are GIOVE (or Galileo) signals. With these two signals, Eq. 4.19 can be written for the GIOVE signals in the following way:

$$\rho_A = \rho_{\mathrm{IF(E1X,E5X)}} + I_A + CB_{\mathrm{rcv,A}} + CB_{\mathrm{sat,A}} \tag{4.29}$$

In a similar way as before, the receiver- and satellite-dependent biases could now also be derived for the GIOVE observations, such that they cancel out in the ionosphere-free

combination if E1X and E5X signals are used, but the corresponding corrections based on differential code biases are retained for different signal combinations. We can also find an expression similar to Eq. 4.20 to make all GIOVE observations consistent with the ionosphere-free combination of E1X and E5X signals:

$$\begin{aligned}\rho_{IF(C,D)} =& \rho_{\mathrm{IF(E1X,E5X)}} \\ &+ a_{\mathrm{C}}(CB_{\mathrm{rcv,C}} + CB_{\mathrm{sat,C}}) + a_{\mathrm{D}}(CB_{\mathrm{rcv,D}} + CB_{\mathrm{sat,D}}) \qquad (4.30)\\ =& \rho_{\mathrm{IF(E1X,E5X)}} \\ &+ b_{\mathrm{sat,IF(C,D)}} + b_{\mathrm{rcv,IF(C,D)}} \qquad (4.31)\end{aligned}$$

In this equation, different signal identifiers C and D are used to emphasize that GIOVE signals are used in this case. Similar to Eq. 4.20, the combined code bias corrections would be zero if the signals C and D coincide with E1X and E5X and non-zero if other signals are used. Now, a final step remains to make the linear-combination of GIOVE observations compatible with the linear-combination of GPS. Since the GPS and GIOVE signals may be affected by different hardware delays in the receiver, the linear combination of P1 and P2 for GPS may have an offset compared to the linear combination of E1X and E5X for GIOVE. This bias is commonly referred to as an inter-system-bias (ISB) [Píriz et al., 2006] and must be accounted for in mixed GNSS processing. The inter-system bias is equipment-dependent and thus varies between different stations in a network. Thus, in order to make Eq. 4.31 consistent with the ionosphere-free combination of P1 and P2, the intersystem-bias $b_{\mathrm{ISB,IF(E1X,E5X)-IF(P1,P2)}}$ is introduced:

$$\begin{aligned}\rho_{IF(C,D)} =& \rho_{\mathrm{IF(P1,P2)}} \\ &+ b_{\mathrm{sat,IF(C,D)}} + b_{\mathrm{rcv,IF(C,D)}} + b_{\mathrm{ISB,IF(E1X,E5X)-IF(P1,P2)}} \qquad (4.32)\end{aligned}$$

A more elaborate notation is chosen here in order to emphasize that the inter-system bias depends on the selection of the reference frequencies of both systems, in this case E1X and E5X for GIOVE and P1 and P2 for GPS. Special care must be taken in using different signals. If, for example, the C/A-code is used for the GPS observations instead of the P1 code, the use of the receiver-dependent code bias is mandatory! When processing GPS satellites only, this common bias is absorbed in the receiver's clock offset and is not harmful. In mixed processing with different constellations however, the resulting receiver clock offset, which refers now to the ionosphere-free combination of C1 and P2, would cause an inconsistency in Eq. 4.32, which requires the receiver clock to be consistent with IF(P1,P2). As a consequence, the GIOVE observations will be biased with respect to the GPS observations by the receiver-dependent P1C1-bias. More details on the estimation and practical use of the GIOVE biases will be given in Chap. 7.1.

4.3 Filter Design

This section begins with the derivation of the necessary equations for setting up the Kalman filter used in RETICLE. In the following, the entire filter update loop, which is depicted in the center of Fig. 4.1 will be discussed in further detail.

The filter state includes the satellite clock error $dt^{(s)}$ and the clock drift $df^{(s)}$ for the complete constellation of 32 satellites. The state vector additionally comprises the receiver clock offset dt_n, a differential tropospheric zenith delay dT_n as well as the float carrier-phase ambiguities $A_{n,i}$ for all satellites in view of each station. The subscript n denotes the individual tracking station and i denotes the i-th satellite tracked by the station. The current GPS constellation has 30 active satellites and the typical tracking network size for the filter is about 30 stations. The assumption that each station tracks 12 GPS satellites at a time leads to a total number of about 500 elements in the state vector.

Some of the state vector elements require further explanation: The estimated satellite clock offset and drift are computed with respect to the GPS time scale. The receiver clock offsets for the tracking stations, however, do not represent the offset of the real receiver clocks, since the observations have been pre-processed before being used in the filter. The pseudorange observations are used together with the a-priori orbits and the known station position to compute a coarse estimation of the receiver's clock error. All observations and the measurement epoch are then corrected by the estimated clock offset. This pre-processing is necessary to reduce large clock jumps on the order of milliseconds. The remaining variations in the ground stations' clocks are typically less than a microsecond, after the pseudorange-based clock correction has been applied. The receiver clocks are modeled as white-noise processes and their variation is compensated by process noise in the Kalman filter.

The estimated differential tropospheric zenith delay has already been explained in further detail in Sec. 4.2.3. The carrier-phase ambiguities in the filter state are estimated as float values and are not fixed. The state vector $\boldsymbol{x}$ can be written as:

$$\boldsymbol{x} = \begin{bmatrix} (dt^{(1)} & \cdots & dt^{(n_{sat})})^T \\ (df^{(1)} & \cdots & df^{(n_{sat})})^T \\ (dt_1 & \cdots & dt_{n_{sta}})^T \\ (dT_1 & \cdots & dT_{n_{sta}})^T \\ (A_{1,1} & \cdots & A_{1,n_{cha}})^T \\ \vdots & & \vdots \\ (A_{n_{sta},1} & \cdots & A_{n_{sta},n_{cha}})^T \end{bmatrix} \tag{4.33}$$

In this equation, n_{sat} denotes the number of satellites and n_{sta} is the number of stations included in the filter. n_{cha} is the maximum number of channels for each receiver. For clock estimation of the GPS constellation, n_{sat} is set to 32. The number of channels is typically set to 12 for each receiver.

In order to be able to perform the Kalman filter time update, the state vector must be predicted towards the next update epoch. It turns out that the state vector for the clock estimation problem can be predicted in a straightforward manner, since most parameters evolve linearly or are assumed to remain constant over short time intervals. Therefore the integration of differential equations is not necessary. The clock offsets of the GPS satellites are predicted linearly in time using the estimated clock drift. The GPS satellite clock drifts, the station clock offsets, the differential tropospheric zenith path delays and the carrier-phase ambiguities are assumed to be constants. The state vector can thus be

predicted without loss of accuracy from epoch k to epoch $k+1$ according to:

$$\boldsymbol{x}_{k+1}^{-} = \boldsymbol{\Phi}\boldsymbol{x}_{k}^{+} \tag{4.34}$$

In this notation, the superscript '$-$' denotes the state vector prior to the measurement update, whereas the superscript '$+$' indicates the already updated state vector. The state transition matrix used for the propagation has the following form:

$$\boldsymbol{\Phi} = \begin{bmatrix} \boldsymbol{I}_{n_{sat}} & \Delta t\boldsymbol{I}_{n_{sat}} & \boldsymbol{0}_{n_{sat},n_{cha}\cdot n_{sta}} \\ \boldsymbol{0}_{n_{sat},n_{sat}} & \boldsymbol{I}_{n_{sat}} & \boldsymbol{0}_{n_{sat},n_{cha}\cdot n_{sta}} \\ \boldsymbol{0}_{n_{cha}\cdot n_{sta},n_{sat}} & \boldsymbol{0}_{n_{cha}\cdot n_{sta},n_{sat}} & \boldsymbol{I}_{n_{cha}\cdot n_{sta}} \end{bmatrix} \tag{4.35}$$

Here, $\boldsymbol{I}_i$ denotes an identity matrix with i rows and columns. $\boldsymbol{0}_{i,j}$ is a zero matrix with i rows and j columns. The term Δt is the time step between two filter updates. The index n denotes the number of stations in the network. The last element on the main diagonal has $14n$ elements, since clock offset, zenith path delay and 12 carrier-phase ambiguities are estimated for each station.

The Kalman filter also keeps a record of the estimated error of the state vector elements in the covariance matrix $\boldsymbol{P}$. The station transition matrix is also utilized for the update of the covariance matrix:

$$\boldsymbol{P}_{k+1}^{-} = \boldsymbol{\Phi}\boldsymbol{P}_{k}^{+}\boldsymbol{\Phi}^{T} + \boldsymbol{Q} \tag{4.36}$$

In this equation, the matrix $\boldsymbol{Q}$ is the process noise matrix, which shall be introduced later in this section. After the prediction step, where the state vector and its covariance matrix are updated to the current epoch, the measurement update is performed. The modeled observations can be generally written as

$$\tilde{\boldsymbol{y}}_k = \boldsymbol{h}_k(\boldsymbol{x}_k) + \boldsymbol{v} \tag{4.37}$$

where $\tilde{\boldsymbol{y}}_k$ is a vector of modeled measurements at epoch k. The vector function $\boldsymbol{h}_k$ maps the state vector $\boldsymbol{x}_k$ to the observations. The mapping functions for the pseudorange and carrier-phase measurements have already been defined in Eq. 4.5 and Eq. 4.7. Finally, $\boldsymbol{v}$ denotes the remaining, unmodeled measurement errors, which are assumed to be Gaussian white noise. The assumed covariance matrix of the observations $\boldsymbol{R}$ is a diagonal matrix with the square of the standard deviations of the pseudorange and carrier-phase observations on the main diagonal.

For the measurement update, the Kalman gain $\boldsymbol{K}$ must be computed first. It is the quantity used in the Kalman filter to determine the magnitude of the corrections applied to the state vector during the measurement update. The magnitude of the Kalman gain is determined by the covariance of the measurements $\boldsymbol{R}$, the covariance of the state vector $\boldsymbol{P}$ and the sensitivity matrix $\boldsymbol{H}$. The latter quantity is computed from the derivative of the measurement mapping function $\boldsymbol{h}$ with respect to the state vector $\boldsymbol{x}$:

$$\boldsymbol{H}_k = \frac{\delta \boldsymbol{h}}{\delta \boldsymbol{x}}\bigg|_{\boldsymbol{x}_k^{-}} \tag{4.38}$$

Due to the large dimension of the state vector, a derivation of the complete equation for $\boldsymbol{H}$ is not provided here. However, a few remarks shall be provided about the characteristics of this matrix. It provides information about the sensitivity of the estimation

parameters in the state vector to the observations. The number of columns corresponds to the number of estimation parameters and the observations are associated with the rows of the matrix. Having evaluated the matrix for all observations of a given epoch, the sensitivity of a certain estimation parameter to the given measurements can be obtained by inspecting the corresponding column of the matrix $\boldsymbol{H}$. If an element is zero in the sensitivity matrix, the corresponding parameter cannot be observed by this measurement. If a column of $\boldsymbol{H}$ contains exclusively zeros, then this estimation parameter is unobservable by the measurements and can only be estimated from the information provided in the system model. This case applies to all GPS satellite clock drift parameters. They are estimated from the change in the clock offset parameters as defined in the state transition matrix Eq. 4.35. Now, the Kalman gain can be computed according to:

$$\boldsymbol{K}_k = \boldsymbol{P}_k^- \boldsymbol{H}_k^T \left[\boldsymbol{H}_k \boldsymbol{P}_k^- \boldsymbol{H}_k^T + \boldsymbol{R}_k\right]^{-1} \tag{4.39}$$

Finally, the measurement update equation for the state vector can be evaluated, using the Kalman gain and the measurement residuals, which are the differences between the real measurements $\boldsymbol{y}$ and their model according to Eq. 4.37:

$$\boldsymbol{x}_k^+ = \boldsymbol{x}_k^- + \boldsymbol{K}_k \left[\boldsymbol{y} - \boldsymbol{h}\left(\boldsymbol{x}_k\right)\right] \tag{4.40}$$

Note that the superscript of the state vector has changed, to indicate the state prior to and after the update. In addition to the state vector, the covariance information in the filter must be updated as well. Therefore, the covariance matrix update is performed according to:

$$\boldsymbol{P}_k^+ = \left[\boldsymbol{I} - \boldsymbol{K}_k \boldsymbol{H}_k\right] \boldsymbol{P}_k^- \tag{4.41}$$

The thoughtless implementation of Eq. 4.41, however, may lead to problems, since rounding errors can cause the predicted covariance matrix to loose its symmetric properties. In order to avoid this undesired effect, the alternative formulation of the covariance update equation can be chosen, which is known as the Joseph's form or Joseph-stabilized version. The basic idea is to use a less condensed version of Eq. 4.41, which reads as follows:

$$\boldsymbol{P}_k^+ = \left[\boldsymbol{I} - \boldsymbol{K}_k \boldsymbol{H}_k\right] \boldsymbol{P}_k^- \left[\boldsymbol{I} - \boldsymbol{K}_k \boldsymbol{H}_k\right]^T + \boldsymbol{K}_k \boldsymbol{R}_k \boldsymbol{K}_k^T \tag{4.42}$$

Though not immediately obvious, Eq. 4.41 and Eq. 4.42 are interchangeable. The advantage of the latter formulation lies in the fact that it enforces the covariance matrix to remain symmetric and is less likely to lose the required property of positive definiteness [Crassidis and Junkins, 2004]. However, these advantages do not come without a price to be paid for them. Obviously, Eq. 4.42 requires much more computational effort to evaluate. For the RETICLE system, the Joseph-stabilized version has, nevertheless, been selected. The processing time for the filter update is still fast enough to manage the envisaged update rate and provide sufficient computation time for other tasks to be performed. Since the filter is supposed to operate continuously over long periods of time, round-off errors are more likely to build up and affect the filter in the long run. Thus numerical stability is of high importance.

This step concludes the Kalman filter loop, which continues again with the propagation to the next measurement epoch. Fig. 4.4 summarizes the most important equations

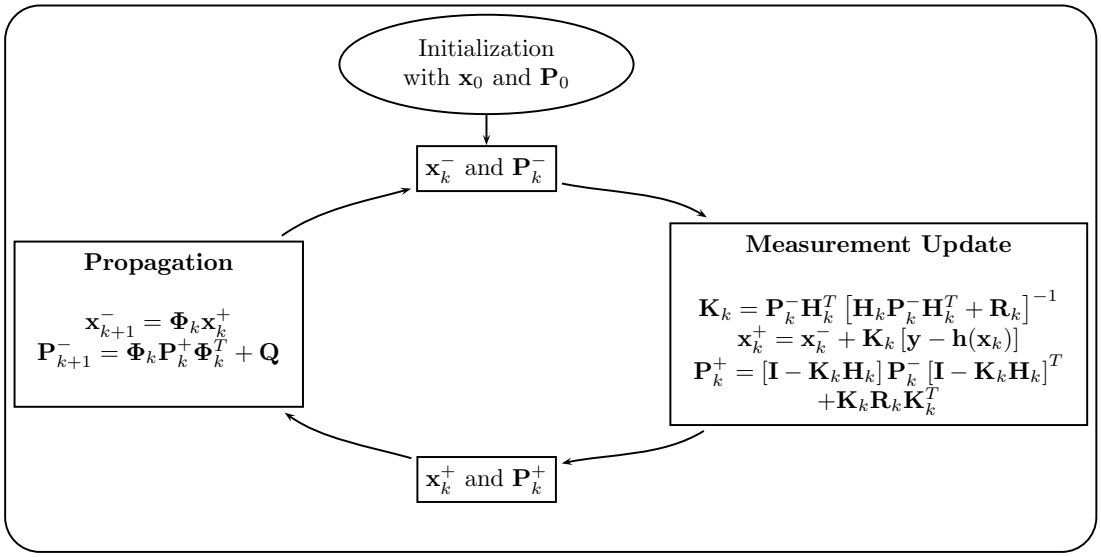

Fig. 4.4: Flowchart of the Kalman filter loop

used for the prediction and measurement update step. Upon initialization a first guess of the state vector $\boldsymbol{x}_0$ and the covariance matrix $\boldsymbol{P}_0$ is required. The initial covariance provides information about the expected errors in the initial guess for the state vector and contains the square of the initial standard deviation on the main diagonal:

$$\boldsymbol{P}_0 = \begin{bmatrix} \sigma_{0,dt}^2 \boldsymbol{I}_{n_{sat}} & \mathbf{0} & \mathbf{0} & \mathbf{0} & \mathbf{0} \\ \mathbf{0} & \sigma_{0,df}^2 \boldsymbol{I}_{n_{sat}} & \mathbf{0} & \mathbf{0} & \mathbf{0} \\ \mathbf{0} & \mathbf{0} & \sigma_{0,dt_n}^2 \boldsymbol{I}_{n_{sta}} & \mathbf{0} & \mathbf{0} \\ \mathbf{0} & \mathbf{0} & \mathbf{0} & \sigma_{0,dT_n}^2 \boldsymbol{I}_{n_{sta}} & \mathbf{0} \\ \mathbf{0} & \mathbf{0} & \mathbf{0} & \mathbf{0} & \sigma_{0,A}^2 \boldsymbol{I}_{n_{sta} \cdot n_{cha}} \end{bmatrix} \tag{4.43}$$

The derivation of the Kalman filter equation is now complete, except for the discussion of the process noise, which is a critical component in the filter design and shall thus be discussed in more detail. Obviously, the assumptions made for the development of the state vector variables over time do not perfectly match their true behavior. The strictly linear development of the clock offset is certainly not true for longer time intervals due to hardly predictable effects like thermal variations on board the GPS satellites, which cause a variation in the clock drift. Even over the short update intervals of several seconds, the clock offset and drift are affected by phase and frequency noise of the atomic clock (compare Chap. 2). Furthermore, the ground station clock offsets and the differential tropospheric delays are subject to variations. Thus, the system model (or process model) deviates from the truth.

During the measurement update, the filter has to merge the information from the system model with the observations. Obviously, if the system can be modeled only poorly, but the measurements have a high quality, the latter should be weighted strongly during the measurement update. In the opposite case, when a system can very well be described by a model but the observations are noisy, the estimation parameters should only be gradually corrected to allow a suppression of the measurement noise. The quality of the system model and the measurements are characterized via their statistical

properties. The derivation of the Kalman filter assumes that all systematic effects in the measurements and the system model are eliminated by including them as estimation parameters or employing suitable models. Thus, the remaining errors should only have random characteristics and can be described by statistical noise processes [Crassidis and Junkins, 2004].

The covariance of the state vector is reduced with each measurement update as obvious from Eq. 4.41 and is driven towards zero when more and more measurements are being processed. As a result, the Kalman gain decreases, which leads to a diminishing impact of the measurements during the measurement update according to Eq. 4.40. Ultimately, the filter would reject the information from the observations and purely rely on the system model. This will inevitably lead to a divergence of the estimation parameters from the truth over time. In order to avoid this divergence, the covariance is increased during the prediction step according to the expected deviation of the system model from the truth over this time interval. These errors in the system model are statistically modeled in the process noise matrix $\boldsymbol{Q}$ in Eq. 4.36. The addition of process noise prevents the covariance of the state vector to drop below a certain threshold and prevents the measurements from being rejected. For an optimal filter performance, the filter settings should be selected such that enough process noise is added to avoid a divergence of the state from the truth, but at the same time the noise in the measurements is suppressed by the filter. A reasonable selection of the filter parameters is therefore essential for the performance of the filter.

For the RETICLE filter, the increment in process noise is assumed to result from an integrated white noise process, or random walk process, and the associated covariance grows linearly in time. The process noise is characterized using the standard deviation σ and a time constant τ in this case. As already mentioned, the process noise must be applied to the satellite and ground clock states as well as to the tropospheric zenith wet-delay estimation to account for deviations from the assumed linear or constant development in time. The system model for the float ambiguities assumes these parameters to be constant, which should also reflect their true behavior. However, it will be shown in Sec. 4.5 that the inclusion of process noise of the ambiguities is beneficial for the clock estimation. As a result, a small amount of process noise is added to the ambiguities as well in order to ensure a variation of these parameters throughout the satellite pass. Contrary to the other parameters, the process noise is scaled with the elevation E of the satellite. For simplicity, the matrix $\boldsymbol{Q}$ is assumed to be a diagonal matrix:

$$\boldsymbol{Q} = \begin{bmatrix} \frac{\sigma_{dt}^2 \Delta t}{\tau_{dt}} \boldsymbol{I}_{n_{sat}} & \mathbf{0} & \mathbf{0} & \mathbf{0} & \mathbf{0} \\ \mathbf{0} & \frac{\sigma_{df}^2 \Delta t}{\tau_{df}} \boldsymbol{I}_{n_{sat}} & \mathbf{0} & \mathbf{0} & \mathbf{0} \\ \mathbf{0} & \mathbf{0} & \frac{\sigma_{dt_n}^2 \Delta t}{\tau_{dt_n}} \boldsymbol{I}_{n_{sta}} & \mathbf{0} & \mathbf{0} \\ \mathbf{0} & \mathbf{0} & \mathbf{0} & \frac{\sigma_{dT_n}^2 \Delta t}{\tau_{dT_n}} \boldsymbol{I}_{n_{sta}} & \mathbf{0} \\ \mathbf{0} & \mathbf{0} & \mathbf{0} & \mathbf{0} & \frac{\sigma_A^2 \Delta t}{\tau_A} cos\,(E)\, \boldsymbol{I}_{n_{sta} \cdot n_{cha}} \end{bmatrix} \tag{4.44}$$

Having completed the formal derivation of the necessary equations for the Kalman filter, the individual steps of the complete algorithm shall be described in more detail. Upon start of the filter, an initialization of the state vector parameters and the corre-

sponding covariance matrix is necessary. The satellite clock offsets and drifts are initialized using the values provided in the IGS ultra-rapid predicted product. The remaining state vector elements, the receiver clock offsets, the tropospheric zenith-delays and the ambiguities, are set to zero. The ambiguities are initialized on-the-fly by the ambiguity management as shown in Fig. 4.1. As previously mentioned, an initial covariance matrix, representing the errors in the initial guess of the state vector, must also be provided and is set up according to Eq. 4.43. The values for the a-priori standard deviation are summarized in Tab. 4.1. It should be added here that the initial values for the covariance errors are not only used upon initialization of the filter, but also for example after a re-initialization of the clock parameters for a satellite, when it is stated to be healthy again after a maneuver or clock maintenance.

The standard deviation of the observables used for $\boldsymbol{R}$ in Eq. 4.39 can be found from an assessment of the measurement precision. For this purpose, the residuals of the pseudorange and carrier-phase measurements have been analyzed. The station positions have been computed with a precise point positioning routine using daily data batches and CODE final orbits and clocks. In order to gain better statistics, one complete month has been processed. The results have already been shown in Tab. 3.1. It turns out that the pseudorange observations have residuals on the order of 1 m. The exception are stations employing a Leica's GRX1200GGPRO receiver with active smoothing of pseudoranges. For these receivers, the residuals can be as low as 0.30 m, depending on the selected smoothing interval. The residuals of the carrier-phase observations in Tab. 3.1 vary between 6 mm and 12 mm. These values have been used for the standard deviation of code and carrier-phase measurements.

An additional note should be added here concerning the smoothed pseudorange observations. The derivation of the Kalman filter assumes all measurements to be uncorrelated [Crassidis and Junkins, 2004]. If the pseudorange observations are smoothed with the carrier-phases over a certain interval, the measurements are correlated with each other. As long as the smoothing interval is sufficiently short compared to the filter update rate, this is of little relevance. For increasing smoothing intervals, however, the correlation increases as well, which violates the basic assumption of uncorrelated measurements. In practice, this problem cannot be avoided, since the configuration of the receivers is out of reach and no alternative source for unsmoothed observations is available. Adverse effects due to the correlated measurements could not be detected so far.

Contrary to the measurement standard deviation, the process noise of the state vector elements, which characterizes the deviation of the system model from the truth, cannot be assessed directly. In the case of the GPS satellite clocks, the phase and frequency noise can be assessed by computing the Allan variance or Hadamard variance of each individual satellite clock. A process noise model can then be derived for each clock, which incorporates the contributions of the individual noise components for white noise and Flicker noise on phase and frequency [Hutsell, 1996].

For the RETICLE filter, a simplified approach has been chosen, which assumes the same process noise settings for all GPS satellite clocks. A coarse approximation of the predicted clock errors has been computed from the Allan deviation provided in Fig. 2.1 by multiplying the Allan deviation $\sigma(\tau)$ at time interval τ with the corresponding time

interval [Misra and Enge, 2001]. This leads to a process noise standard deviation of 3 centimeters at a time-constant τ of 600 s for the clock offset. The clock drift process noise is set to a standard deviation of 0.0005 m/s ($\approx 10^{-12}$ s/s) over 900 s. Though these setting may not perfectly reflect the performance of each individual clock, it has been found during the operation of the system, that the amount of process noise is sufficient to avoid filter divergence and at the same time reduce the effects of measurement outliers and noise. Furthermore, using default parameters eliminates the need for frequent updates of the parameters in case of clock switches on board the satellites. Thus, robustness and autonomy of the RETICLE system is improved.

The differential zenith-path delays of the ground stations are assumed to be constant in the filter model and only have a small variation over time. Therefore, only a small amount of process noise with a standard deviation of 2 mm over 1 hour is selected. The ground station clock offsets require a significantly higher process noise, since they will exhibit stochastic behavior with variations on the order of tens of meters. This is caused by the a-priori clock offset correction, which will be introduced in more detail in following paragraphs. A large process noise on the order of 100 m over 100 s has been selected. The carrier-phase ambiguities are initialized from the difference of the pseudorange and carrier-phase. In order to ensure proper convergence from the coarse initial values, an a-priori standard deviation of 5 m is selected. The settings for the process noise and the measurement noise are summarized in Tab. 4.1.

Tab. 4.1: Filter settings for RETICLE Kalman filter

Process Noise:	σ_0	σ	τ
GPS clock offset	5 m	0.03 m	600 s
GPS clock drift	0.005 m/s	0.0005 m/s	900 s
Rcv clock offset	100 m	100 m	100 s
Tropospheric zenith delay	0.5 m	0.002 m	3600 s
Ambiguities	5 m	0.001 m	30 s
Measurement Noise:			
Pseudorange		0.3-2.0 m	
Carrier Phase		6-12 mm	
Clock Constraint		0.1 m	

The Kalman filter estimation loop depicted in Fig. 4.1 starts with the pre-processing of all observation collected at the epoch. Fig. 4.5 provides an overview of the data editing process. The selected thresholds for the data editing process are summarized in Tab. 4.2. In the first step, some fundamental checks to ensure data-integrity are performed. First, orbit and clock information must be available for the corresponding satellite. The RETICLE system uses the orbit information from the IGU predicted orbits and the estimated clock offsets from the filter state for data editing. If no estimated clock offset is present for a tracked satellite, the availability of the IGU predicted clock value is checked, since it will later be used to initialize the estimation in the filter state. The observations are screened for missing pseudoranges. Satellites which have dropped below an elevation limit of 12.5° are rejected. The signal-to-noise density ratio (SNR) of the observations must be higher than a threshold of 15 dB-Hz. Furthermore, the availability of differential code biases and antenna phase center corrections for the satellite

are required. Finally, satellites with active maneuvers or maintenance indicated by a NANU are rejected.

Tab. 4.2: Data editing limits for RETICLE Kalman filter

Edit Limits:	
Elevation	12.5 °
SNR	15.0 dB-Hz
Code-Carrier-Difference	10.0 m
Pseudorange RMS	2.0 m
Carrier-Phase RMS	0.05 m

In the next step, the receiver clock offset is computed from the mean value of the differences between modeled and measured pseudoranges for all accepted satellites. The filter uses the estimated satellite clock offsets, which have been predicted with the estimated clock drift to the current epoch, for the pseudorange modeling. Outlier satellites are then identified and rejected by monitoring the RMS residuals of the computed receiver clock offset. Since the clock offset is the only free parameter in this calculation, at least three satellites are required to identify and eliminate an outlier satellite. However, in practice a larger minimum number of satellites of at least four is beneficial to ensure a robust identification of outliers. If the RMS of the pseudorange residuals exceeds the limit defined in Tab. 4.2, the clock offset computation is repeated with recursive exclusion of a single satellite. The solution with the smallest RMS residuals identifies the satellite with the corrupt pseudorange measurement, which is then definitely rejected. This procedure is repeated, if necessary, until the RMS drops below the threshold or too few satellites remain to continue. In the latter case, all measurements from this station are rejected.

If the clock offset computation has been successful, it is eliminated from the observations by firstly correcting the epoch and secondly correcting all pseudorange and carrier-phase measurements after converting the clock offset to the appropriate units of meters or cycles, respectively. The necessity for the clock offset elimination results from the fact that many receivers in the real-time network are not connected to atomic-clocks. To avoid large offsets of the internal oscillator with respect to GPS time, the receiver computes its clock offset and keeps it within boundaries of $\pm$ 0.5 ms. As a result, the receiver clock undergoes frequent jumps of 1 ms, which cannot be compensated easily by the Kalman filter. With the computed receiver clock offset, these large jumps can be reduced to a residual clock error on the order of less than a microsecond, which can be compensated for by process noise in the Kalman filter. It should be mentioned, however, that the epochs of the measurements originating from different stations are not aligned to integer epochs any more. In order to restore this alignment, the carrier-phases and pseudoranges must be propagated to integer epochs using the corresponding Doppler frequency. The Doppler, however, is in general not transmitted by real-time stations. Thus, the RETICLE system processes the un-aligned measurements as observations at the closest integer epoch. Considering that the GPS satellites exhibit clock drifts on the order of 1 mm/s, the error caused by the maximal possible misalignment of 1 ms is negligible.

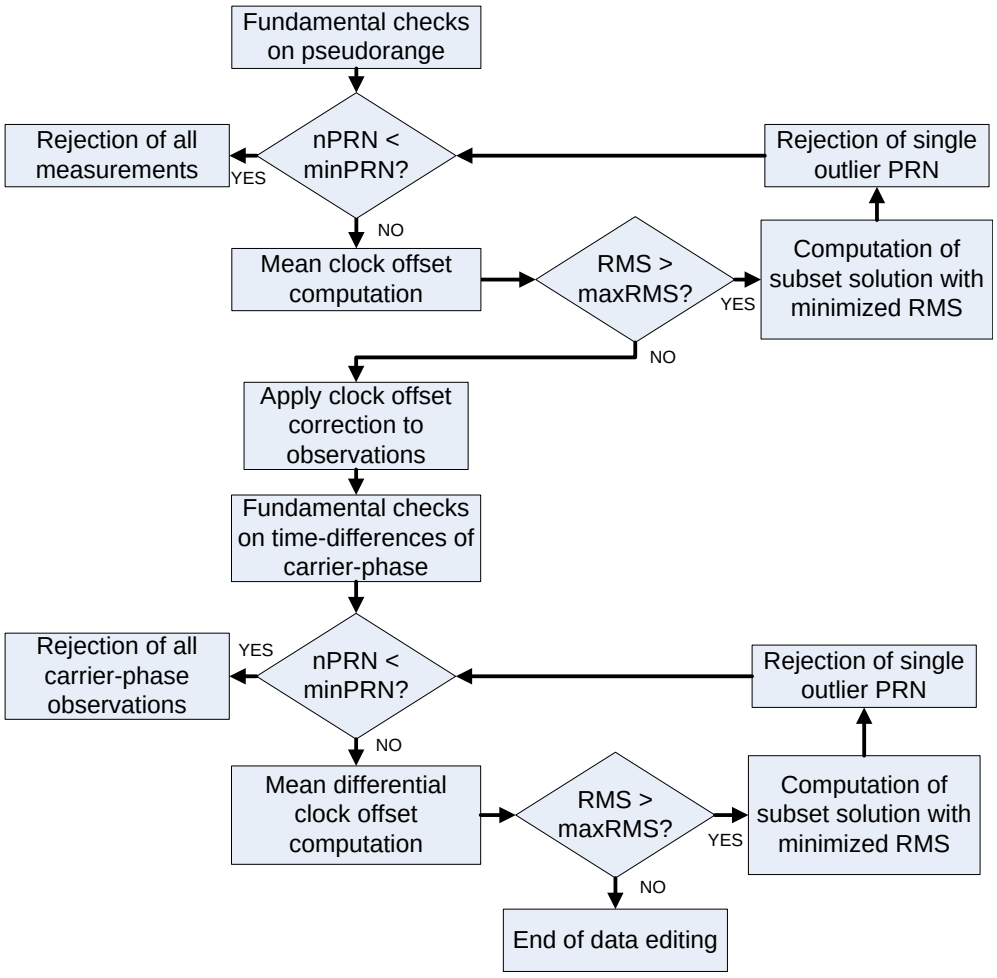

Fig. 4.5: Flowchart of the data-editing algorithm used by RETICLE. nPRN denotes the number of valid observations, minPRN is the minimal required number of observations for a robust data editing, typically set to 4. RMS denotes the RMS of the observation residuals and maxRMS is the corresponding editing limit from Tab. 4.2.

The data editing of the carrier-phase measurements is very similar to the approach used for the pseudoranges. At the beginning, the data is again screened for missing carrier-phase observations. Since the carrier-phases are subject to ambiguities, the data editing is performed on time-differences of observables from the previous to the current epoch, which eliminates constant biases. Additionally, the differences of the time-difference of pseudorange and carrier-phase observations are formed. Ideally, this value is zero, because both observables change equally over time. However, different noise characteristics and different multipath-effects let the code-carrier-difference deviate from zero. If the difference exceeds a certain threshold, a code-carrier-inconsistency is detected, which is in most cases caused by a large cycle-slip in the carrier-phase. Another cause for this inconsistency originates from the internal clock correction of the receiver. Whereas most receivers correct the pseudorange and carrier-phase on a clock reset, some do not apply this correction to the carrier-phase. In this case, the correction during clock offset elimination must not be applied to the carrier-phases. The following receivers have been identified to show this behavior:

- ASHTECH UZ-12
- TRIMBLE 4000SSI
- Septentrio PolaRx2 (depending on firmware-version)

Finally, the same recursive elimination of observations is performed on the carrier-phases, in case the RMS residuals exceed the threshold. If the number of available observations drops below the minimum, all carrier-phase measurements are rejected. A filter-update using the pseudoranges can still be performed however.

After the pre-processing of the observations, the filter state and the covariance matrix are propagated from the last epoch to the current epoch using Eq. 4.34 and Eq. 4.36. The ambiguity management in the next step ensures proper allocation of ambiguities in the filter state. If satellites have dropped below the elevation limit of the filter or are no longer tracked, their ambiguities are deleted and the space in the filter state is made available for new ambiguities. If satellites are newly acquired, their ambiguities are initialized using code-carrier differences to provide their initial values. Also, ambiguities of satellites which have been rejected during the data screening are removed from the filter and initialized again as soon as valid measurements for the satellite are available.

Prior to the measurement update, a clock constraint is applied to tie the clock corrections to the GPS timescale. In the clock filter, the mean value of GPS satellite clock ensemble is unobservable. It is obvious from Eq. 4.5, that a common bias can be added to all satellite clocks and can be compensated for by the ground station clocks. If unconstrained, this bias can grow infinitely large. To avoid this potentially unbound offset of the GPS clocks, a "pseudo"-measurement update is performed. For this update, the mean value of the predicted IGU clock offsets is used as observation of the mean of the estimated clock offsets for a given epoch. Thus, the observation y_{CS} of the clock constraint is found from:

$$y_{CS} = \frac{c}{n_{sat}} \sum_{m=1}^{n_{sat}} \delta t_{m,IGU} \tag{4.45}$$

where $\delta t_{m,IGU}$ is the clock offset of the m-th satellite in the IGU predicted product. The modeled observation $\tilde{y}_{CS}$ is formed equivalently from the estimated offsets of the state vector:

$$\tilde{y}_{CS} = h(\boldsymbol{x}) = \frac{c}{n_{sat}} \sum_{m=1}^{n_{sat}} \delta t_m \tag{4.46}$$

Finally, the sensitivity matrix $\boldsymbol{H}_{CS}$ with the derivatives of eq. 4.46 with respect to the state vector is derived as:

$$\boldsymbol{H}_{CS} = [1 \cdots 1 \;\; 0 \cdots 0] \tag{4.47}$$

$\boldsymbol{H}_{CS}$ is a matrix with one row and 64+14n columns. Having derived these equations, the clock constraint can be included in the Kalman filter measurement update procedure and processed together with the other scalar measurement updates.

Though not explicitly mentioned here, it should be noted that satellites, which are unhealthy and thus excluded from the clock estimation but still present in the IGU predictions, are excluded from the clock constraint, to avoid jumps and subsequent biases in the constellation mean offsets if a satellite switches from healthy to unhealthy or vice versa. As a result of the clock constraint, the estimated clocks are tied to a virtual reference clock without the need to fix one of the satellite or receiver clocks to zero.

The final step of the filter loop depicted in Fig. 4.1 is the measurement update of the Kalman filter. It is performed with a latency of 4 seconds after the measurement epoch, to allow sufficient time for the observations to be transmitted via the internet. The complete Kalman filter update from the state propagation to the measurement update takes approximately 1 second. The estimated clocks are therefore available 5 seconds after the epoch; however, additional delays occur due to the transmission to the user. These delays are not critical however, since the satellite clocks can be predicted using the estimated clock rate. Thus, the satellite clocks can also be made available in "true" real-time.

4.4 Satellite Clock Discontinuity Detection

The clock estimation strategy introduced in the previous sections assumes a linear clock model and compensates small deviations from this model by using process noise. This approach is no longer valid when the GPS satellite's clock exhibits a discontinuity, which seriously violates the statistical assumption of the short term clock behavior defined by the process noise settings. Though these discontinuities, or clock jumps, happen only rarely, they can significantly disturb clock estimation algorithms. As a matter of fact, in the early development phase of the RETICLE system, when a protection against clock jumps was not yet included in the algorithm, the Kalman filter was affected by a clock jump and could not recover in an acceptable amount of time. A manual interaction was necessary to restart the system. This event triggered the implementation of a clock jump detection scheme, which will be introduced in Sec. 4.4.1.

Having detected a clock jump immediately requires a second step, which is to manipulate the clock filter algorithm in order to avoid that the results of the affected satellite are degraded. It turns out that this step is of high importance for the RETICLE system, since undetected clock jumps will also have an influence on the clock estimation of the other satellite clocks, which are not affected by the clock jump. The reason for this sensitivity is the clock constraint, mentioned in the previous sections, which couples the mean estimated clock offset to the mean predicted clock offset of the IGU predicted orbits. If a single satellite clock out of N clocks is biased by Δt, this constraint will lead to a bias on the order of $\frac{\Delta t}{N-1}$ of the remaining satellites. Though this effect is not potentially harmful, since common biases vanish in the receiver clock offset without affecting the navigation solution, it is still undesirable, since certain users may have requirements for the stability of the estimated receiver clock. Therefore, care is taken in the clock discontinuity recovery to assure a reasonably smooth and unbiased estimation after the clock jump.

Last but not least, if a clock jump has been detected and its effects have been diminished as much as possible, the information about this irregularity should be shared with the users as well. This knowledge enables users to take further actions on their end, for example excluding an affected satellite from the solution or at least considering the possibly degraded clock offset estimate in their statistical error modeling.

The following sections describe the discontinuity detection and recovery scheme, which has been implemented in the algorithm. Additionally, examples for clock jumps

will be provided. The reaction of the filter to these jumps will be shown as well to demonstrate the performance of the implemented detection and recovery.

4.4.1 Discontinuity Detection and Recovery Scheme

The data editing algorithm, where all observations must pass prior to being included in the Kalman filter, is the most suitable place in the RETICLE processing algorithm for the clock jump detection. The data editing has already been introduced in Sec. 4.3 and depicted in Fig. 4.5. It is based on the outlier detection of the pseudorange and carrier-phase observations. When a clock discontinuity of several decimeters or meters occurs, the pseudorange observations will pass the data editing procedure due to the comparably high editing threshold of the pseudorange. However, at carrier-phase level, the editing threshold is much lower. As a result, the time differences of the carrier-phase measurements prior to and after the clock discontinuity do not pass the RMS-test due to their high residuals and are rejected. Since the clock jump is observed at all stations equally, this rejection of the carrier-phase observations happens at all stations tracking the affected satellite. Therefore, the global editing of all carrier-phase observations from a particular satellite is in general a sign of a clock anomaly. Furthermore, assuming that the clock discontinuity did not cause a loss-of-lock of the carrier-phase, the value of carrier-phase residual provides a decent estimate of the magnitude and sign of the clock jump. Taking the mean and the standard deviation of the residuals of all rejected carrier-phase observations, the first can be taken as a measurement of the clock jump and the latter provides information about the accuracy of this measurement.

The clock jump detection implemented in RETICLE monitors the editing status of the carrier-phase observations for all satelites. If continuous carrier-phase tracking is interrupted for a satellite on global level, a clock discontinuity is detected. The mean and standard deviation of the residuals is calculated to assess the magnitude of the clock jump. During the state-vector update step of the Kalman filter, the clock offset of the affected satellite is manipulated and adjusted according to the detected discontinuity. Additionally, the covariance of the clock offset is increased by the standard deviation of the residuals. This manipulation is only performed, however, if the standard deviation of the residuals stays below a threshold of 20% of the magnitude of the clock jump. If this threshold is exceeded, indicating a bad estimate of the clock jump, the state vector is not manipulated. Instead, the covariance of the clock offset and drift estimate of the affected satellite is reset to the initial covariance value used upon initialization.

This precaution is necessary to prevent possible adverse effects of the clock jump detection for two special cases: It has been observed several times during the operation of the RETICLE filter, that tracking of a GPS satellite is lost globally by all stations simultaneously without the occurrence of a clock jump. The detection of a clock discontinuity, however, was triggered, since all receivers restarted the carrier-phase tracking, which results in changed ambiguities, and therefore all carrier-phase observations dropped out of the differential editing. Consequently, the mean of the carrier-phase residuals yields an erroneous estimate for the non-existing clock discontinuity, which can be recognized from a large standard deviation. In this case, the clock estimate must not be manipulated; however, the increased standard deviation assists the filter to re-converge to a precise clock estimate again. A paper recently published by Gordon et al.

[2009] discusses very similar observations made during the operation of the WAAS system. The paper highlights problems caused by carrier-phase perturbations of PRN21, which led to a global loss-of-lock for this satellite in the WAAS tracking network. Similar problems also occur for other satellites, however, PRN21 in particular seems to be affected most frequently [Gordon et al., 2009].

The second case, which will lead to problems with the adopted clock discontinuity detection, is an event, at which a part or all of the tracking stations loose lock on the carrier-phases due to the clock jump. The same problem with the differential carrier-phase editing mentioned in the previous case reappears again here. Since the carrier-phase ambiguities have changed for many or all receivers, the mean of their residuals yields a degraded or completely meaningless estimate of the clock discontinuity with a high standard deviation. Again, only the covariance is increased to enable a quick re-convergence of the clock offset.

After this introduction of the clock jump protection and recovery implemented in RETICLE, the next sections will introduce three examples of clock irregularities. The results presented have been postprocessed with an offline version of the real-time algorithm, which has served as a prototype implementation for RETICLE and has already been introduced in a previous publication [Hauschild and Montenbruck, 2009].

4.4.2 Examples of GPS Clock Jumps

In the following sections, three examples for clock jumps are presented. The events are verified from inspections of the final clock solutions from the Center for Orbit Determination in Europe (CODE). Then, the comparison of the real-time solution with respect to the CODE solution shows the performance of the clock discontinuity detection and recovery.

Clock Jump PRN24

The first example for a clock jump is shown in Fig. 4.6. The plot shows the clock solution for PRN24 (SVN24) obtained from the CODE final product on June 26th, 2008 with a discontinuity at approximately 17:40h. This Block-IIA satellite, which is still available in the current constellation at the time of writing, was launched at the beginning of July 1991, being the second oldest space vehicle in the constellation [Langley, 2009]. The clock used for the signal generation on board of the satellite was switched from a rubidium to a cesium atomic standard in September 2000, meaning that the satellite is running on the second of its four clocks. Until now, no other clock switches have been done and the same cesium standard is still in use [USNO, 2009].

The plot in Fig. 4.6 shows the reference clock solution after the removal of a second order polynomial. It becomes obvious, that the clock follows this polynomial with small deviations until approximately 17:40:30h. Then a discontinuity of about 3 m occurs. Afterwards, the clock solution continues smoothly. There are no obvious explanations for this discontinuity available. According to the Notice Advisories to Navstar Users the satellite was set healthy during the occurrence of the clock jump. Also, no information about a clock switching commanded by the GPS operators is available.

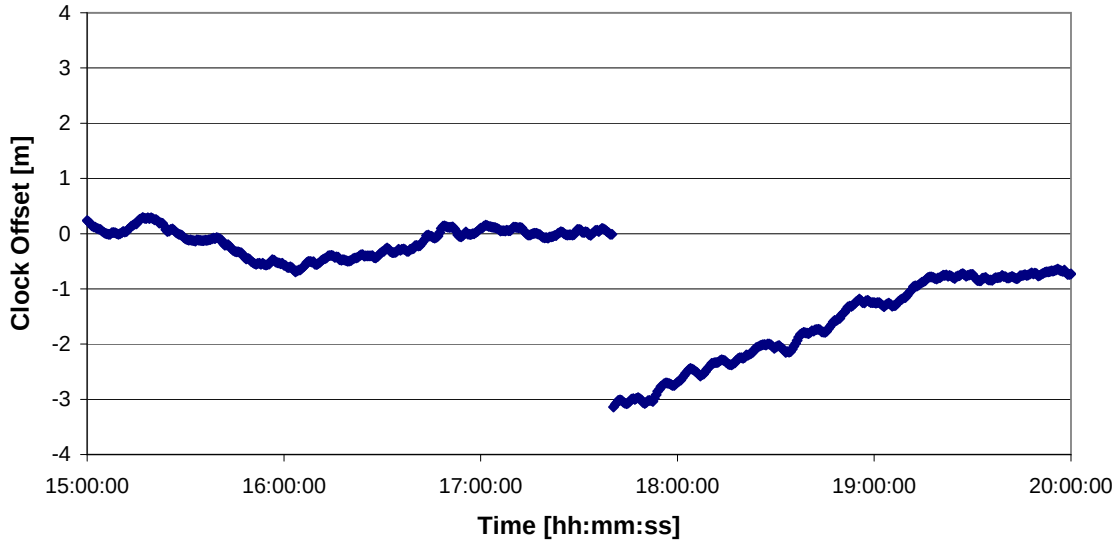

Fig. 4.6: Example for clock jump of PRN24, 2008/06/26 17:40h from CODE final clock product. A second order polynomial has been removed from the clock.

Fig. 4.7 shows the clock offset errors from the real-time Kalman filter compared to the reference solution from the CODE analysis center. It can be seen that the clock offset is biased by approximately +5 cm with respect to the reference prior to the clock discontinuity. After the jump, the bias has changed to about -12 cm. The clock discontinuity is detected between the epochs 17:44:00h and 17:44:30h. The satellite is tracked by seven stations at that time, namely ADIS, BRAZ, CAS1, CTWN, DAV1, MAW1 and RCMN. The differential carrier-phase editing for all stations fails, with residuals on the order of 3.1 m, except for CTWN, which reports a residual of only 1.4 m. Obviously, a cycle slip must have been occurred at this station, which naturally affects the differential carrier-phase residuals. RETICLE reports a clock discontinuity of 2.87 m, which fits reasonably well to the magnitude observed in Fig. 4.6. The clock estimation converges again after the clock jump within several minutes. It should also be noted that the solution is not affected by any significant outliers even directly after the re-initialization of the carrier-phase ambiguities.

This example also demonstrates the importance of continuous carrier-phase tracking for achieving precise clock estimates. Precise information about the short term behavior of the GPS clocks is gained from the carrier-phase observations. Knowledge about the absolute value of the clock is, however, mostly gained from pseudorange observations, since the carrier-phases are per se ambiguous. The estimated clock is smooth before and after the discontinuity, where the short-term variation of the clock is derived from the highly precise carrier-phase measurements. At the clock discontinuity, the ambiguities for the affected satellite are re-initialized. As a result, the effect of carrier-phase measurements on the clock estimation is reduced, since the information about the ambiguities must be rebuilt again from the code- and carrier-measurements. Once the ambiguities have reconverged, a precise and continuous estimation of the clock is possible again. The different bias of the estimated clock before and after the jump is presumably caused by systematic errors of pseudoranges, like multipath. These pseu-

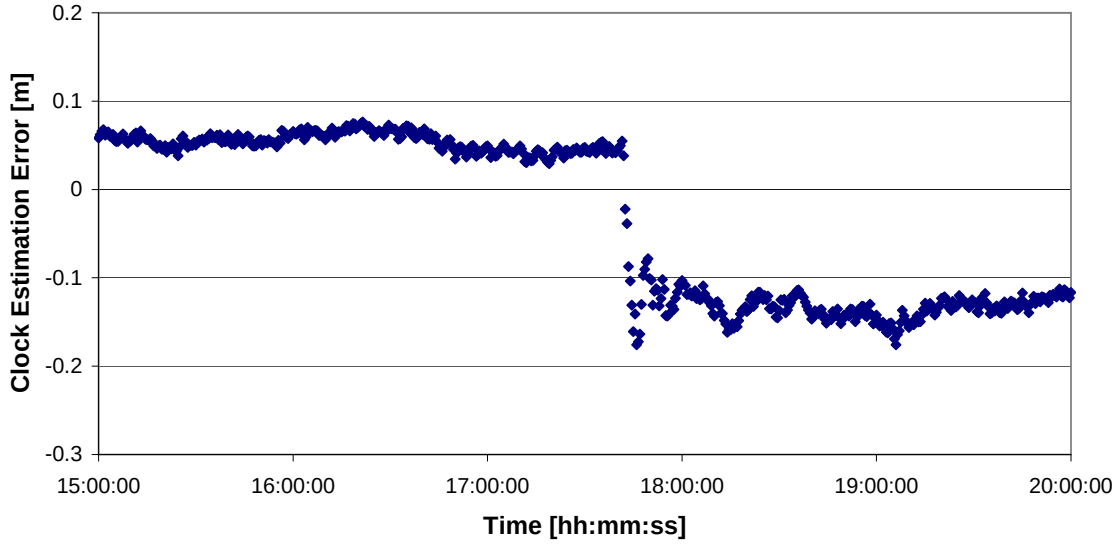

Fig. 4.7: Clock estimation errors for clock jump of PRN24, 2008/06/26 17:40h. The plot shows the comparison of the real-time processing with respect to CODE final clock product.

dorange errors are not suppressed by the filter as long as the precise carrier-phase are available and do not affect the estimated clock. However, when a discontinuity happens, the absolute level of the clock is fixed to a new value, which is influenced by the errors of all pseudorange observations.

Clock Jump PRN05

The second example for a clock jump is shown in Fig. 4.8. The plot shows the CODE reference solution for PRN05 (SVN35), which exhibit a discontinuity of approximately 3 m at 20:43h on November 19th, 2008. This satellite is also a Block-IIA satellite and was launched in October 1993. It is, however, no longer part of the current constellation since it was decomissioned at the end of March 2009 [Langley, 2009]. The rubidium atomic standard was active when the clock discontinuity occurred. Like in the first example, SVN05 was healthy at the point in time of the clock discontinuity and no information about a clock switch is available. Being one of the older satellites in the constellation, several clock switches have been commanded for SVN35 in the past and it operated on its last clock already since September 2005. This clock discontinuity observed in November 2008 could be seen as an indication of this last clock starting to fail, and may have led to the decomissioning of the satellite four months later by the GPS control segment [USNO, 2009]. The plot in Fig. 4.8 shows again the CODE reference clock solution after the removal of a second order polynomial. The clock jump has approximately the same magnitude as the previous example for PRN24 and happens between the epochs 20:43:00h and 20:43:30h GPST.

Fig. 4.9 depicts the results for the real-time clock estimation. The clock jump is detected by RETICLE at 20:43:30h GPST, when the carrier-phase observations are globally lost at eight tracking stations. The estimated magnitude of the clock jump is 2.78 m with a standard deviation of 0.42 m. Similar to the previous example, the clock errors are smooth before and after the discontinuity due to the effect of the carrier-phase ob-

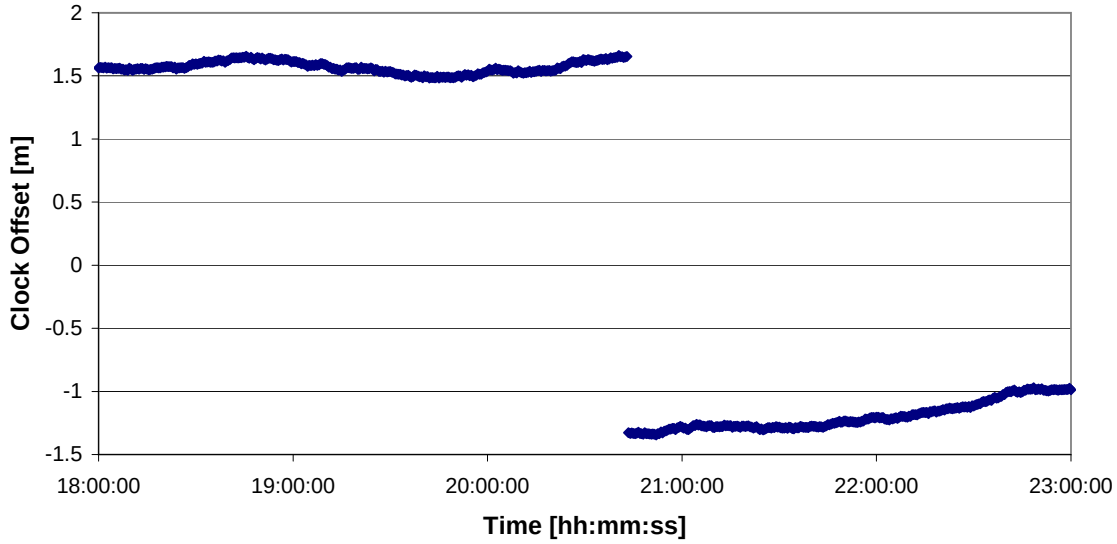

Fig. 4.8: Example for clock jump of PRN05, 2008/11/19 20:43h from CODE final clock product. A second order polynomial has been removed from the clock.

servations. Also, a change in the clock error bias is visible again. Though the solution converges quickly within several minutes, comparably large outliers are present this time during four or five epochs directly after the clock discontinuity appeared.

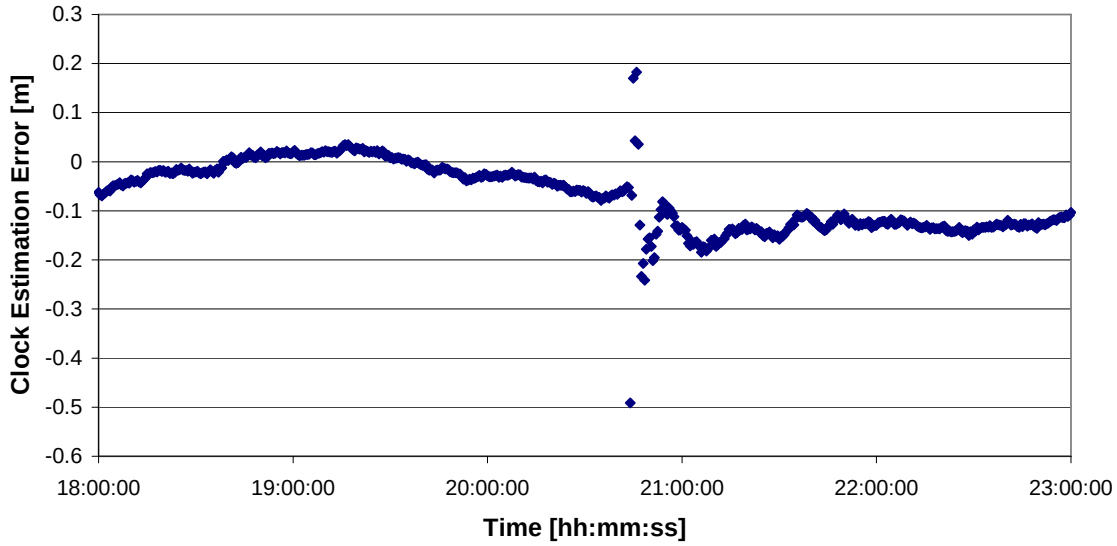

Fig. 4.9: Clock estimation errors for clock jump of PRN05, 2008/11/19 20:43h. The plot shows the comparison of the real-time processing with respect to CODE final clock product

Clock Jump PRN08

The last example for a clock jump is depicted in Fig. 4.10. Again a second order polynomial has been removed from the clock offset of the CODE reference solution in the plot for November 4th, 2008. The affected satellite this time is PRN08 (SVN38). Like

the previous two satellites, SVN38 is a Block-IIA satellite. It was launched in November 1997 and is still active in the current constellation. The satellite has been switched to its second clock in May 2004, which is still used until today [USNO, 2009].

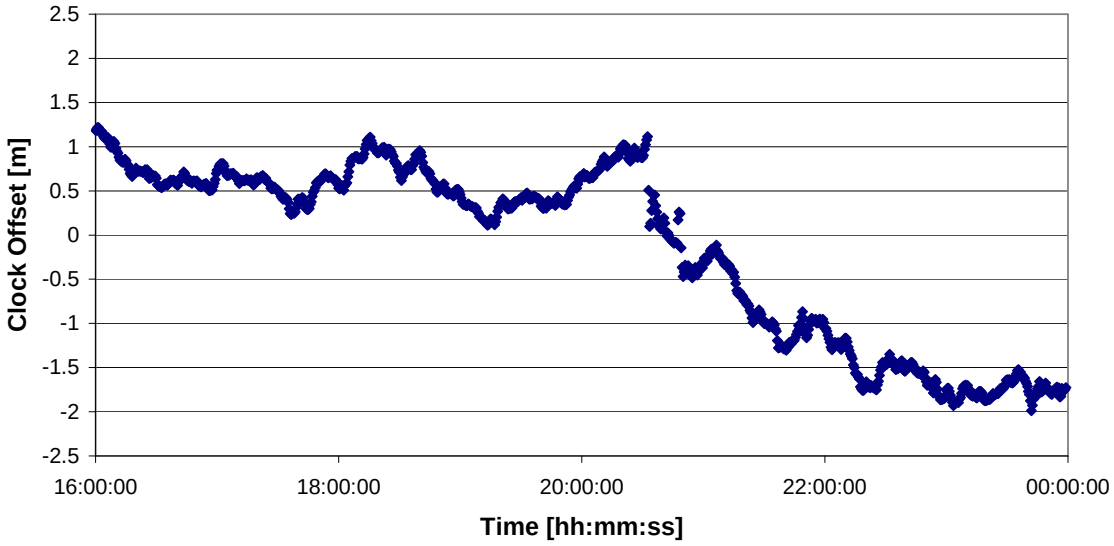

Fig. 4.10: Example for clock jump of PRN08, 2008/11/04 20:34h from CODE final clock product. A second order polynomial has been removed from the clock.

The clock discontinuity of SNV38, differs from the previous examples both in its magnitude and its characteristics. The two other documented events consisted of a single, large discontinuity, which have been preceded and followed by continuous clock development. In this case, however, the clock is affected by several smaller jumps in series. The jumps take place between 20:32:00h GPST and 20:50:00h GPST and are not easily distinguishable in Fig. 4.10. It is interesting to note that the drift of the atomic standard is obviously also affected and changes significantly when the discontinuities start.

To better illustrate the behavior of the clock, a summary of clock jumps is provided in Tab. 4.3. The table provides an overview of the true clock jumps, which are found in the reference clock product and their corresponding time of occurrence. The right column lists the jumps which have been detected in the real-time processing.

Tab. 4.3: Summary of PRN08 (SVN38) clock jumps on Nov 4th, 2008

	Clock discontinuities	
Time	*true*	*detected*
20:32:00 h	0.60 m	0.66 m $\pm$ 0.008 m
20:32:30 h	0.41 m	0.41 m $\pm$ 0.007 m
20:36:30 h	-	0.20 m $\pm$ 0.010 m
20:47:30 h	-	-0.27 m $\pm$ 0.006 m
20:49:00 h	0.39 m	0.38 m $\pm$ 0.007 m
20:49:30 h	0.22 m	0.23 m $\pm$ 0.009 m

The table shows that the frequency standard on board SVN38 suffered from a significant degradation over a period of approximately 30 minutes. During this period,

several clock discontinuities occur with varying magnitude between 22 cm and 60 cm. The right column with the detected clock jumps shows that in the majority of the cases, the discontinuities have been detected correctly. Two false detections, however, occur at 20:36:30h and 20:47:30h.

Fig. 4.11 shows the errors of the real-time clock offset estimation with respect to the CODE reference product. The estimated clock exhibits only a small bias and is smooth until the point in time when the first clock discontinuity occurs. During the period of time where the frequency standard of SVN38 has a degraded performance, the real-time clock shows jumps on the order of 15 cm until the estimation errors finally decrease again. Obviously, this series of clock discontinuities is much more challenging to the filter than the single, isolated jumps which occurred in the previous two examples. This result could be expected, since knowledge of the carrier-phase ambiguities must be newly built up after each clock jump. When the covariance of the ambiguities is high, the effect of the carrier-phase measurements on the clock estimate is reduced. The false detection of two clock jumps in this example magnifies this adverse effect.

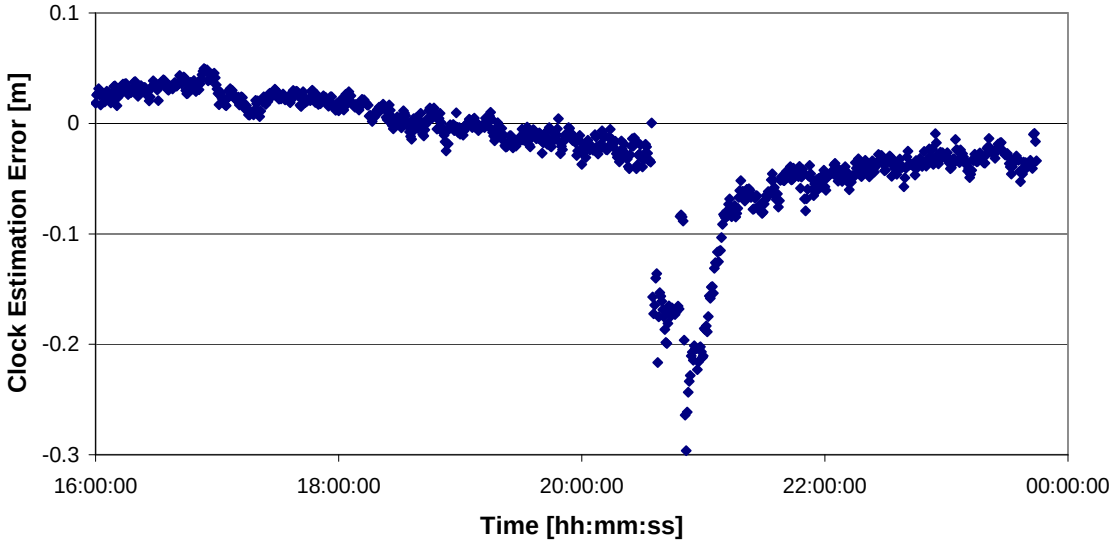

Fig. 4.11: Clock estimation errors for clock jumps of PRN08, 2008/11/04 around 20:34h. The plot shows the comparison of the real-time processing with respect to CODE final clock product.

4.4.3 Problems and Limitations

The three clock discontinuity examples in this section demonstrated the capabilities of RETICLE's clock discontinuity detection and recovery algorithm. It has been shown that the estimated clocks exhibit comparably small discontinuities and increased noise after clock jumps. The discontinuities are most likely attributed to systematic errors of the pseudoranges, which govern the absolute level of the clock estimate. The increased noise is a result of the decreased effect of the carrier-phase observations on the clock estimate, when the covariance of their ambiguities is still high after the re-initialization. However, despite these adverse effects, the clock recovery avoids more serious damage to the estimation process which would otherwise be caused by large clock jumps.

Another problem, which has not been discussed so far, surfaced during the implementation of the clock jump detection. The differential carrier-phase data editing uses predicted clock offsets for the modeling of the observations. If the drift estimate of a satellite's clock deviates significantly from the truth, the predicted clock offset is erroneous and the clock jump detection will trigger. Though bad clock drift estimates are not a major problem for the majority of the satellites, one spacecraft in particular has repeatedly caused the false alarms in the clock jump detection. This satellite is PRN13 (SVN43), which is the oldest Block-IIR satellite and was launched in July 1997. The satellite is still operated on its first rubidium clock [USNO, 2009].

The plot in Fig. 4.12 shows the variation of the atomic clock over time for November 22nd, 2009. The data is obtained from a CODE final product and a second order polynomial has been removed. It becomes immediately obvious from the plot that the clock exhibits an abnormal behavior, which repeats with each orbit. The high resolution of the clocks in the CODE final product reveals that the deviation is not a discontinuity, but a rather continuous process, which appears to result from rapid changes in the clock drift. A similar pattern can be found for other days as well. If the data editing thresholds in the differential carrier-phase editing process are set too small, SVN43 will frequently be globally edited when the changes in the clock drift are high and the predicted carrier-phases deviate too much from the truth. Therefore finetuning of the editing threshold for the carrier-phase editing is crucial to reduce the amount of false alarms in the clock jump detection to a minimum.

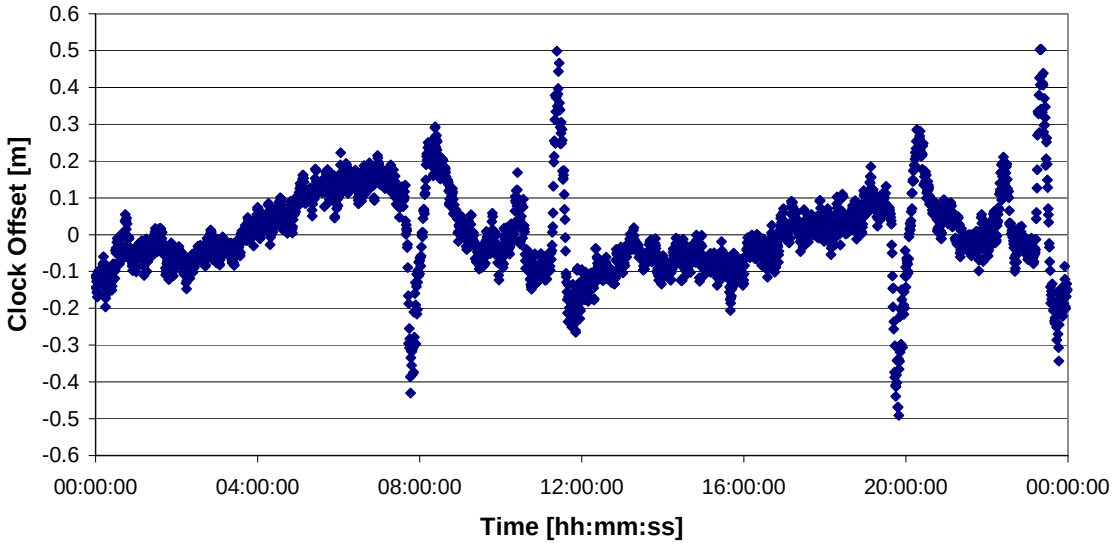

Fig. 4.12: Periodic clock variations of PRN13 for November 22nd, 2009. The plot shows the clock offset from the CODE final product after the removal of a second order polynomial.

Another upcoming challenge in this context will be the increasing ionospheric activity. In times of high solar activities, the electron density in the ionosphere can vary significantly over short distances, which causes fluctuations of the amplitude and phase of radio-navigation signals. This effect is known as scintillation and can cause a loss-of-lock of signals for receivers over larger areas [Datta-Barua et al., 2003]. These effects will have the same characteristic as a true clock jump and will be difficult to distinguish

during the data pre-processing. However, scintillation effects are most likely to occur in low and high latitudes and therefore continuous carrier-phase tracking may still be provided by receivers at mid-latitudes. Furthermore, the advances in receiver technology since the last solar maximum in the year 2000 hopefully have made the current equipment more resistant to scintillation events and will help to minimize the adverse effects in the future.

4.5 Effects of Orbit Errors on Clock Estimation

The following sections evaluate and discuss the effects of orbit errors on the clock estimation. As already explained in the previous sections, the RETICLE system makes use of the Ultra-Rapid orbit product provided by the IGS. An investigation of the orbit errors and their influence on the clock estimation process is therefore important to understand, if the use of the IGU predicted orbits poses a limitation. To point out the effects of orbit errors on clock estimates, dedicated simulations with artificially applied orbit errors are performed and the results are presented. Finally, methods to reduce these effects are introduced and discussed.

4.5.1 IGS Ultra-Rapid Predicted Orbit Error Analysis

The IGU product is generated from the ultra-rapid products of several IGS analysis centers. These input products are combined by the analysis center coordinator. This task is performed by NOAA's National Geodetic Survey (NGS) since February 2008. The product consists of a total data arc of 48 hours. The first half of the data is based on actual observations, whereas the second half are predicted orbits and clocks. The latency from the epoch of the last observations processed until the dissemination of the product is 3 hours.

Fig. 4.13 shows the orbit errors of this product, split up into the radial, along-track and cross-track components with respect to the CODE final orbits, which serve as a reference solution. The plot shows the daily RMS of the orbit errors of the complete constellation for more than one year of RETICLE operation, starting at the end of September 2008 and going until the end of November 2009. The orbit consists of the most recent available predicted orbit, which is updated four times per day and is exactly the same orbit which has been used as input for the RETICLE filter. The gap in October 2009 is due to an interruption of the operation of the RETICLE filter.

The plot shows that the radial orbit error has a daily RMS error of less than 2 cm most of the time. It is the lowest error component and has a high day-to-day repeatability. The second lowest errors are obtained for the cross-track orbit component. The RMS varies between 2 cm and 8 cm most of the time, with some exceptions which reach up to a maximum of 10 cm. Finally, the along-track orbit error varies between 4 cm and 12 cm, with some exceptions extending up to 20 cm. This component contributes most to the overall error budget. The repeatability of the along-track error is also worse compared to the other orbit components. It must be considered, that the orbit predictions have an age-of-data of at least 3 hours, before they can be used in the RETICLE filter. This latency consists of the latency of the product itself plus the time required to update

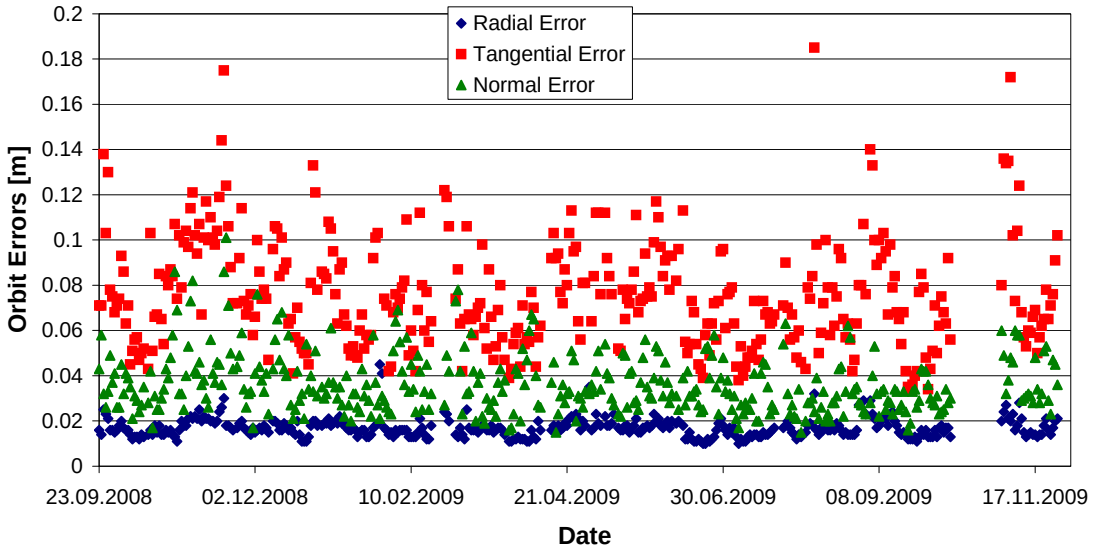

Fig. 4.13: Daily RMS orbit errors of the IGS Ultra-Rapid product Sept. 2008 - Nov. 2009. The plot shows the radial, along-track (tangential) and cross-track (normal) orbit errors of the latest available predicted orbits. Reference orbit is the corresponding final orbit from CODE.

the orbit information in the real-time processing. As already explained in Sec. 4.1, the new IGU orbit is introduced in the filter using a fade-in to avoid orbit discontinuities. This fade-in adds additional latency until the update information is available.

At first glance, no adverse effects on the clock estimation should be suspected, judged by the indeed impressive performance of the IGU predictions. The impact of errors in the modeled satellite position on the clock estimate depends on the projection of these errors on the line-of-sight vector from receiver to the GPS satellite. Though the along-track and cross-track errors of the IGU product are largest, only a fraction of these errors is mapped onto the line-of-sight vector. For a ground-based observer with a GPS satellite directly at zenith, the projection of the along-track and cross-track orbit errors on the line-of-sight vector is effectively zero, since the receiver-satellite range is several orders of magnitude larger than the orbit error. At a low elevation of 10°, still only 25% of these errors affect the modeled range. The radial orbit error on the other hand maps completely onto the modeled range for a satellite at zenith. Even at a low elevation of 10°, 97% of the radial error is still projected on the line-of-sight. These errors would therefore be completely absorbed by the clock estimation. This error absorption is, however, in general rather beneficial than harmful, since the effective range error of the combined orbit and clock product is reduced. Therefore, the direct effect of the IGU orbit errors on the clock estimation accuracy should be expected to pose a major limitation.

However, during the continuous operation of the RETICLE filter over longer periods of time, it could be observed that slowly changing biases in the clock estimates appeared and remained constant for several days, even though the effect of radial orbit errors has been removed. The cause of these biases was unclear until it could be observed that satellites having a low orbit accuracy were more likely to be affected than satellites with good orbits. Thus a correlation between orbit accuracy and biased clock estimates seems to exist. To verify this observation and gain a better understanding of

the underlying effects, a dedicated analysis has been performed and will be presented in the following sections.

4.5.2 Effects of Radial, Tangential and Normal Orbit Errors

For the analysis, one day of recorded data from the stations of RETICLE's real-time network has been used with CEST, the offline version of the real-time filter. The observations have been recorded on October 16th, 2009. The CODE rapid product serves as the source for the GPS satellite orbits and a-priori clocks in this case. The comparison of the estimated clocks with the CODE rapid clocks allows an assessment of the errors. In order to study the effect of orbit errors, constant offsets have been applied to the satellite positions in the radial, along-track and cross-track directions. The following sections provide an overview of the results for the different components of the orbit errors, starting with the radial directions.

Radial Orbit Errors: The effect of the radial orbit errors is shown for the example of PRN02. Fig. 4.14 shows the clock estimation error of CEST with respect to the CODE rapid clocks for the complete 24 hours of the analysis. Two scenarios have been analyzed. First, no additional orbit errors have been applied. The plot shows that the filter takes approximately 2-3 hours for convergence. Afterwards, the clock offset has a bias of approximately 2-3 cm and a small variation.

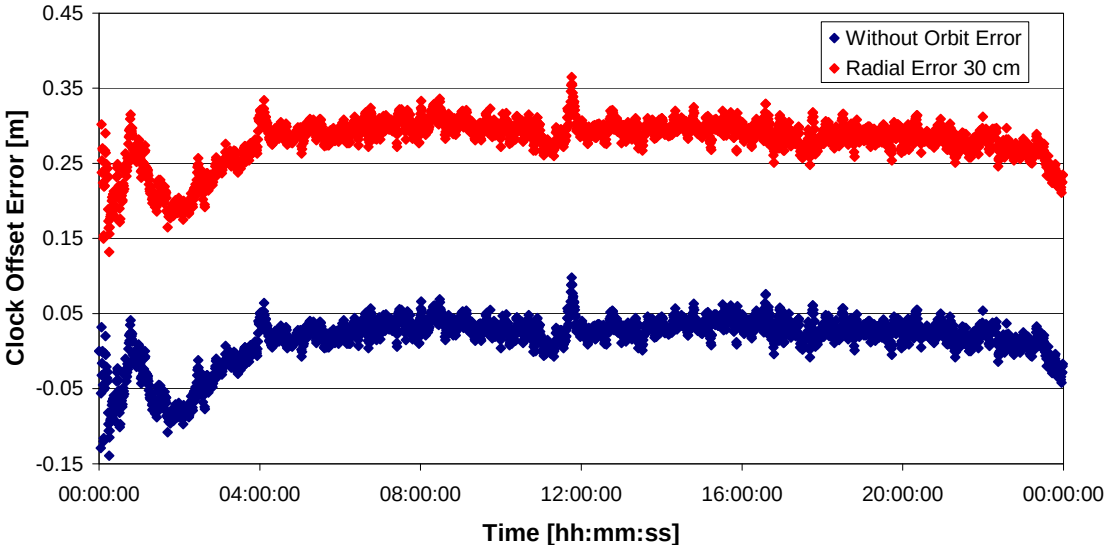

Fig. 4.14: Effect of radial orbit errors on clock estimation. The plot shows an example for PRN02 without additional orbit errors (blue) and with an artificial orbit error of 30 cm applied in the radial direction (red). Clock errors are computed with respect to the CODE rapid clock.

For the second scenario in Fig. 4.14, a constant offset of 30 cm has been applied to the CODE reference orbit. All other processing inputs and parameters are identical to the previous run. It becomes obvious from the plot, that the temporal variation of the clock estimate is very similar to the case without additional orbit errors, however, the clock offset is shifted by 30 cm. This offset exactly matches the radial orbit error, which is applied to this satellite. The result was expected due to the measurement geometry of

a ground-based observer. The radial orbit error is completely absorbed in the satellite clock correction and therefore annihilated in the modeling of the GPS observations.

Along-Track Orbit Errors: The along-track (or tangential) orbit errors are studied in the same way as the previous case. Fig. 4.15 shows the clock estimation errors of CEST with respect to the CODE final clock for PRN13 again without and with additional errors in the along-track direction. The clock estimation requires again a short convergence interval of approximately 2 hours. Afterwards, the clock offset is almost unbiased with errors not exceeding 5 cm.

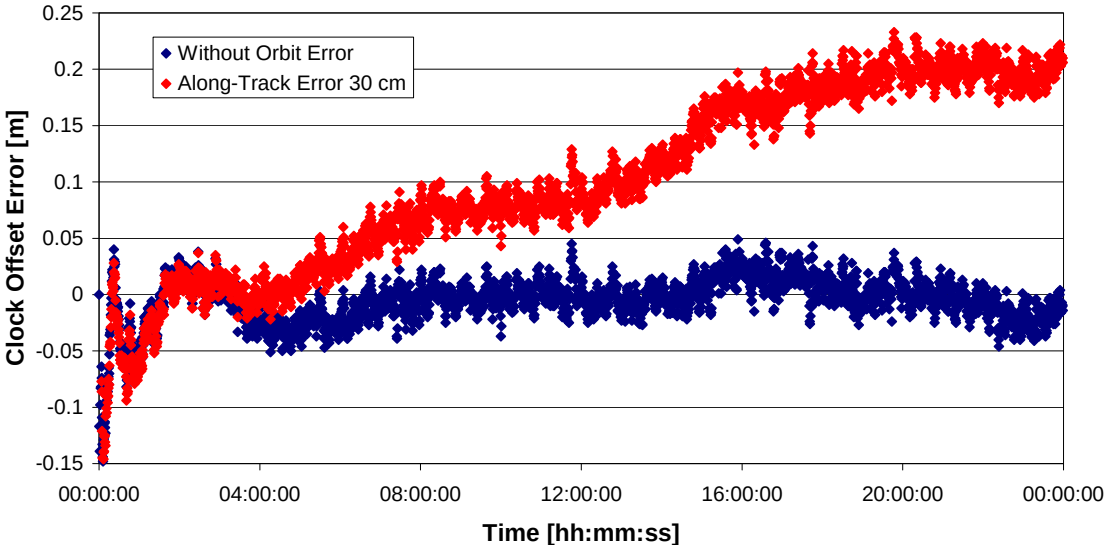

Fig. 4.15: Effect of along-track orbit errors on clock estimation. The plot shows an example for PRN13 without additional orbit errors (blue) and with an artificial orbit error of 30 cm applied in the along-track direction (red). Clock errors are computed with respect to the CODE rapid clock.

The second plot in Fig. 4.15 shows the effect of the along-track orbit errors. For this clock determination run, a constant offset in the tangential direction of 30 cm has been applied to the orbit of PRN13. The first four hours of the clock estimation do not differ significantly from the results for the error-free orbit scenario. Afterwards, the estimated clock starts to deviate significantly from the reference. The deviation appears to follow a linear trend, leading to a continuously growing bias in the clock estimate. After 24 hours of processing, a bias of approximately 20 cm has accumulated. Additional tests with other satellites have been performed to ensure sound results. It has been found that the bias grows faster for larger along-track orbit errors and slower for smaller errors. Furthermore, changing the sign of the along-track error, i. e. applying it in the anti-flight direction, results in a negative bias to be accumulated.

These surprising results are completely different from what would have been expected from considering the observation geometry from a single ground station. Two unfavorable situations apply here: Firstly, the clock estimation errors will grow over time as long as an along-track error is present. Though a comparably large orbit error has been applied in the test case in order to emphasize the effects, smaller errors will over time induce biases of similar magnitude. Secondly, the tangential orbit errors

dominate the error budget of the IGS Ultra-Rapid product as seen in Fig. 4.13, which additionally worsens the situation. Prior to discussing the cause of these growing biases, the effects of the cross-track errors will be presented.

Cross-Track Orbit Errors: The remaining case study shows the effect of cross-track (or normal) orbit errors. PRN14 has been selected for this analysis. The plot in Fig. 4.16 depicts the errors of the clock estimation, showing again the filter's convergence time of approximately 3-4 h. Without artificial cross-track errors, the clock offset estimate is unbiased but is affected by small variations on the order of 2 cm.

The same figure also shows the results obtained with a 30 cm error applied to the cross-track (normal) direction. It becomes obvious that the clock offset is apparently biased by approximately 7.5 cm compared to the reference solution. However, contrary to the along-track orbit error, the bias appears to be constant, at least no accumulating bias is visible over the 24 hour period considered in the analysis. Instead, a sinusoidal variation with a 12 h period is visible in the plot, which suggests a correlation of the clock estimation error with the orbit period.

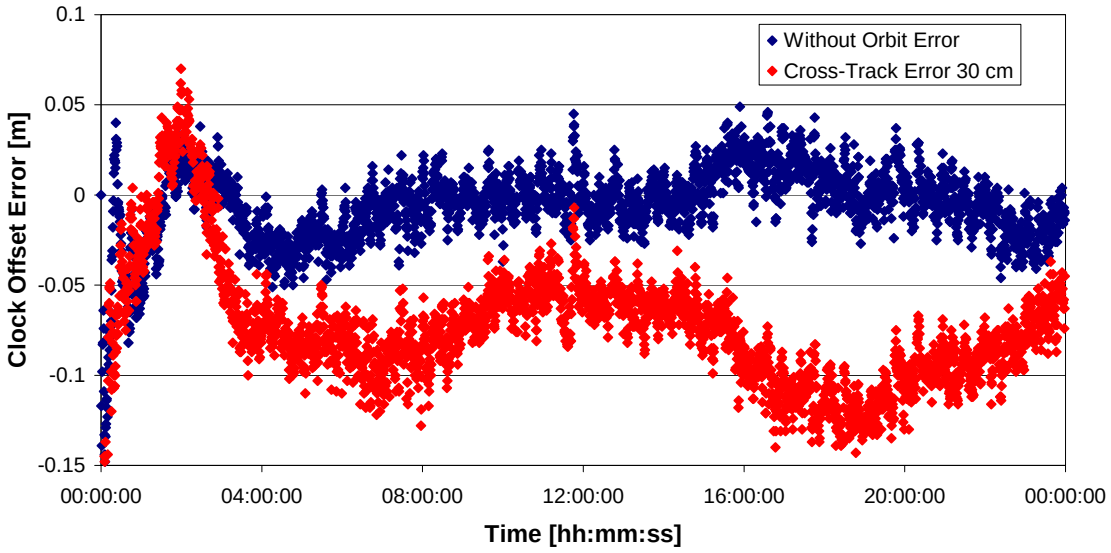

Fig. 4.16: Effect of cross-track orbit errors on clock estimation. The plot shows an example for PRN14 without additional orbit errors (blue) and with an artificial orbit error of 30 cm applied in the cross-track direction (red). Clock errors are computed with respect to the CODE rapid clock.

After having presented the results from the simulation with orbit errors, the origin of these errors shall be discussed in further detail with special emphasis on the most critical case for the tangential errors. The origin of the clock offset for the radial orbit errors is rather self-explanatory and has already been discussed sufficiently at the beginning of this section. For the explanation of the clock biases induced by the along-track errors, a simplified schematic is shown in Fig. 4.17. The figure shows a network of three stations, which receive signals from a GPS satellite. In order to simplify the geometry and keep the scenario clearly laid out, several assumptions are made:

1. The Earth is flat and the satellite is assumed to travel in a straight line.

2. The orbit error remains constant.
3. All measurements are free of errors.
4. All receivers and the satellite have perfect clocks.
5. No cycle slips occur during the entire pass of the satellite over a station.
6. The carrier-phase ambiguities of each receiver are zero.

Assumption 4 means that the receivers' clocks and the satellite clock do not exhibit an offset or a drift with respect to GPS time. This simplification assures that these parameters can be eliminated from the equations in this example. The true satellite position is indicated by a circle on the orbit. The corresponding modeled satellite position, affected by an along-track offset in the anti-flight directions, is shown as a cross. At time t_1, the satellite is tracked only by station 1. The solid line indicates the true range r and the dotted line is the modeled range $\tilde{r}$. Obviously, the modeled range is longer than the true range due to the orbit error. It should be noted that the realistic dimensions could of course not be realized in Fig. 4.17. The magnitude of the orbit error is usually on the order of decimeters, whereas the range varies between 20000 km and 25000 km. It can be assumed that the line-of-sight vectors to the true and modeled satellite positions are parallel and the difference between r and $\tilde{r}$ is simply the projection of the orbit error on the line-of-sight vector, which shall be denoted a here.

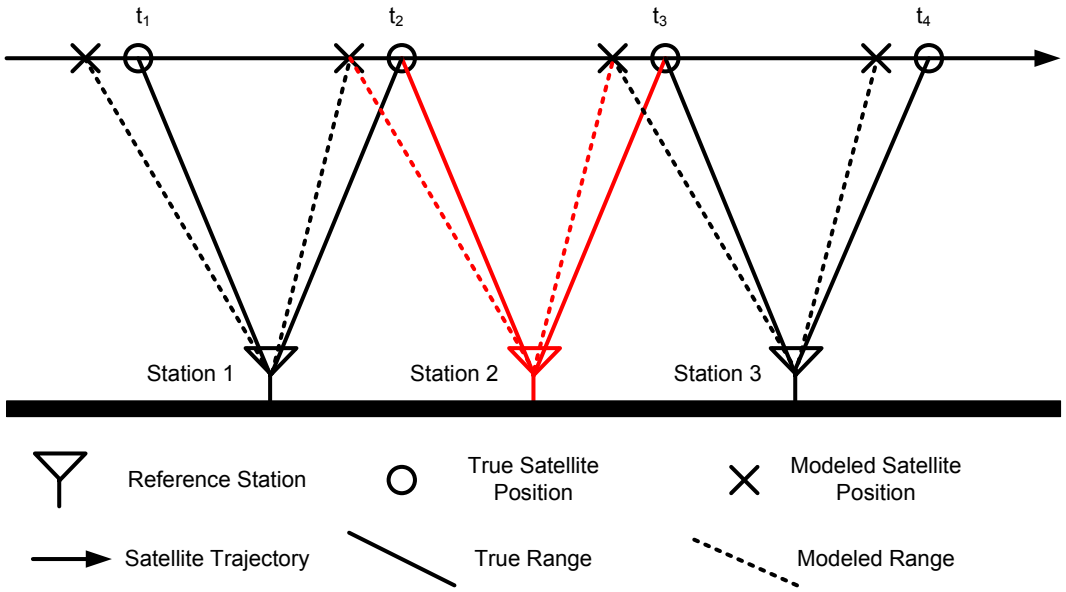

Fig. 4.17: Simplified observation geometry for multiple receivers and a single satellite with constant along-track orbit error

Assume further, that a pseudorange and a carrier-phase observation are available from station 1 at time t_1. The assumptions 3, 4 and 6 ensure that the receiver measures only the true range r. We arrive at very simple equations for the pseudorange observation y_ρ and the carrier-phase observation y_Φ:

$$y_{\rho,1}(t_1) = r \tag{4.48}$$

$$y_{\Phi,1}(t_1) = r \tag{4.49}$$

The modeled observations for pseudorange and carrier-phase, denoted ρ and Φ, respectively, can be found from Eq. 4.5 and Eq. 4.7. Using again assumptions 3, 4 and 6, the following equations can be found for station 1 at t_1:

$$\rho_1(t_1) = r + a - c\delta t^{(s)}(t_1) \tag{4.50}$$

$$\Phi_1(t_1) = r + a - c\delta t^{(s)}(t_1) - A_1 \tag{4.51}$$

Note, that the clock offset of the satellite $\delta t^{(s)}$ is still included in the modeled observations, since it is the estimation parameter. The same also holds for the carrier-phase ambiguity A. As a reminder, the clock offset of the satellite is multiplied with the speed of light c and the carrier-phase ambiguity is multiplied with the wavelength λ of the ionosphere-free combination to assure consistent units of length in the equations. Also note that the projected orbit error a is included in the modeled range, since the wrong satellite position is used here. It is obvious from Fig. 4.17 that the modeled range is longer than the true range, resulting in a positive sign for a. The two unknown quantities $\delta t^{(s)}$ and A can now be determined using the two measurements available at time t_1. Combining Eq. 4.48 and Eq. 4.50 yields an estimate of the satellite's clock offset:

$$c\delta t^{(s)}(t_1) = a \tag{4.52}$$

Combining Eq. 4.49 and Eq. 4.51 together with the estimate of the clock offset from Eq. 4.52 allows the estimation of the carrier-phase ambiguity:

$$A_1 = 0 \tag{4.53}$$

In this simplified example, we assume that the ambiguity can be estimated by a single measurement and is constant thereafter. In summary, we gain an estimate of the satellite's clock offset, which should be zero but is affected by the projected orbit error. The carrier-phase ambiguity has also been determined. Assumption 5 allows us to use this carrier-phase ambiguity from now on continuously over the complete pass of the satellite. As a result, the clock offset can from now on be determined solely from the carrier-phase measurements. Keeping this in mind, we proceed to time t_2. Station 1 still tracks the satellite and due to the symmetry of the picture, the measured carrier-phase observation is identical to Eq. 4.49. However, the modeled range is now obviously shorter than the true range as the satellite has passed over the station. Therefore, the sign of the orbit error projection changes. Due to assumption 2, the magnitude is still the same. Thus, for time t_2 we find:

$$\Phi_1(t_2) = r - a - c\delta t^{(s)}(t_2) - A_1 \tag{4.54}$$

$$y_{\Phi,1}(t_2) = r \tag{4.55}$$

Evaluating these two equations and recalling that $A_1 = 0$, we find for the estimated clock offset at time t_2:

$$c\delta t^{(s)}(t_2) = -a \tag{4.56}$$

Note, that the estimated clock offset has decreased from a to $-a$ from time t_1 to t_2. At t_2, station 2 acquires the satellite for the first time. The modeled carrier-phase measurement

Φ_2 and the true carrier-phase measurement $y_{\Phi,2}$ of this station can be found as:

$$\Phi_2(t_2) = r + a - c\delta t^{(s)}(t_2) - A_2 \tag{4.57}$$

$$y_{\Phi,2}(t_2) = r \tag{4.58}$$

Note that the sign of the projected orbit error is positive again, since the modeled range is larger than the measured range. The satellite's clock offset $c\delta t^{(s)}(t_2)$ is already known at this epoch from Eq. 4.56, which allows us to compute the unknown carrier-phase ambiguity directly as

$$A_2 = 2a \tag{4.59}$$

Note that at epoch t_2 the estimated satellite clock offset is $-a$ and the estimated ambiguity is $2a$, but both should actually be zero. We proceed to time t_3 with the assumption that again no cycle slips occur and the carrier-phase ambiguity of station 2 remains constant. The following equations are gained for the modeled and the measured carrier-phase observations:

$$\Phi_2(t_3) = r - a - c\delta t^{(s)}(t_3) - A_2 \tag{4.60}$$

$$y_{\Phi,2}(t_3) = r \tag{4.61}$$

Combining these two equations together with the known ambiguity from Eq. 4.59 yields the clock estimate at epoch t_3:

$$c\delta t^{(s)}(t_3) = -3a \tag{4.62}$$

Continuing this process to time t_4 in the same manner yields an estimate of the carrier-phase ambiguities for station 3 of $A_3 = 4a$ and a clock offset of $c\delta t^{(s)}(t_3) = -5a$, for the next station an ambiguity of $A_4 = 6a$ would be estimated and so on.

Tab. 4.4 summarizes the results for this simple scenario. It becomes obvious, that the estimated clock offset, which should remain constant, has a linear (!) trend and drifts over time away from the truth. It can also be seen that the estimated ambiguities deviate from the truth with a linear trend as well. It can therefore be concluded, that under the given assumptions, where the ambiguities are fixed at the very beginning and then seamlessly handed over from one station to the next station, offsets build up in the ambiguities and the clock offset. The driving force behind this effect is the change in sign of the orbit error projection on the line-of-sight vector, as the satellite passes over the ground station. Since the ambiguities have been fixed instantly at the beginning of the pass and the projected error changes from $-a$ to a, the residual of the observed minus the modeled carrier-phase measurement is pushed into the satellite's clock offset. At the hand-over to the next station, the biased clock estimate is fixed into the new ambiguities. Again, residuals of modeled minus observed observations will grow in the same direction and push the bias of the clock offset even further.

After having presented a possible explanation for the accumulating effect of the clock offset in the case of along-track orbit errors, the assumptions made in the derivation must be carefully reviewed to verify, if the same effect can also be responsible in the real application. Firstly, assumption 1 simplifies the geometry. In the example, only exact zenith-passes of the satellite over the ground stations are assumed. In reality, the

Tab. 4.4: Clock offset and ambiguity estimation results for simplified along-track error scenario in Fig. 4.17

Epoch	t_1	t_2	t_3	t_4	t_5
$c\delta t^{(s)}$	a	-a	-3a	-5a	$\cdots$
A	0	2a	4a	6a	$\cdots$

observation geometry varies from station to station depending on the satellite's ground track. However, the driving force behind the accumulating bias in the simplified scenario is the change in the sign of the projected orbit error for ascending or descending satellites. For a satellite, which is approaching the station and therefore ascending in elevation, an along-track error in the anti-flight direction increases the modeled range. If this satellite is moving away from the station, the modeled range is decreased. This effect, however, still holds for the more complicated geometry of the real world. The second assumption is that the along-track error is constant over a sufficiently long period for the accumulating effect to build up. If the along-track errors in the IGU orbits were of short term or even stochastic variation, this assumption would clearly be violated. However, the example shown in Fig. 4.18 demonstrates that constant orbit biases in the along-track direction occur in reality. The figure depicts the orbit errors of PRN03 on October 16th, 2009 compared to the CODE final product.

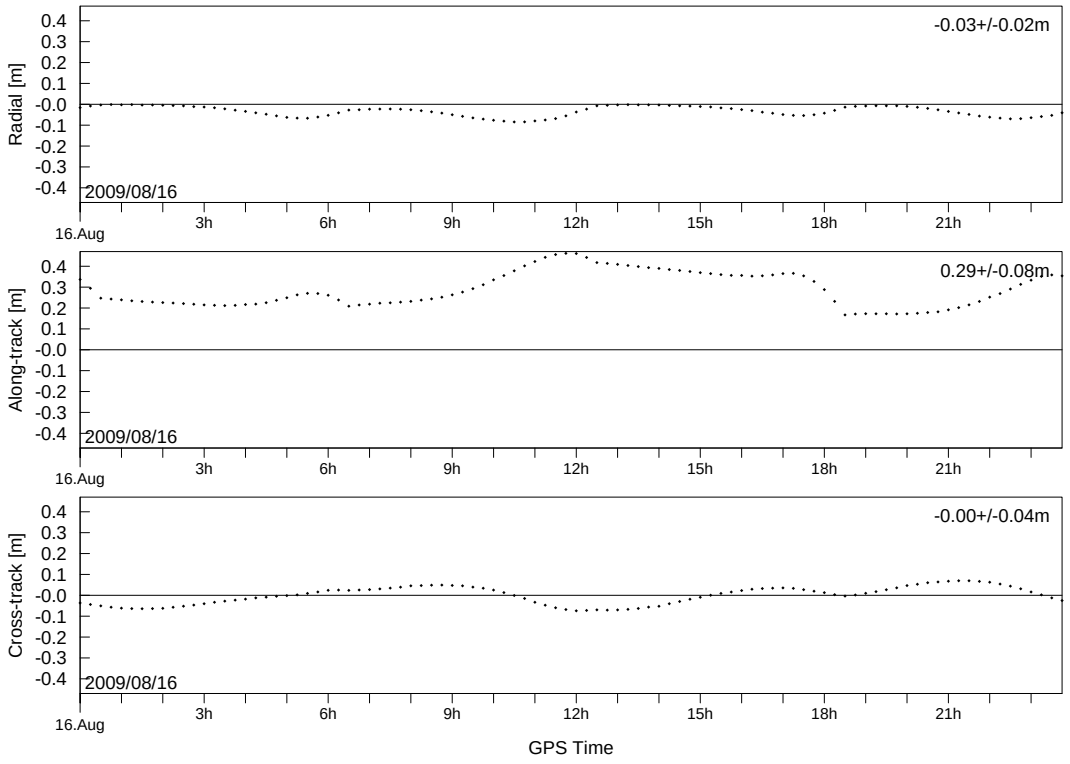

Fig. 4.18: Radial, along-track and cross-track orbit errors of IGU for G03 on Aug. 16th, 2009. Reference orbit is the corresponding CODE final product.

The middle plot with the tangential orbit errors clearly shows a bias with a mean of approximately 30 cm and a standard deviation of 8 cm in the flight direction, which

proves that assumption 2 also holds true in reality. Reviewing the accuracy of the RETICLE product for this day reveals that this satellite was indeed affected by a particularly high bias in the estimated clock. This is another indication that the correlation of along-track errors and clock biases can also be found in the real-world application.

The assumption which implies perfect measurements is of course not valid in reality. Instead, stochastic errors with zero mean will only add noise on the clock estimates. Systematic errors with comparably long time constants like multipath can cause additional effects in the estimation parameters. However, the multipath on the carrier-phase observations can at most amount to one quarter of the wavelength, which corresponds to approximately 2.5 cm for the ionosphere-free combination. The multipath of the pseudorange can be several orders of magnitude larger, however, the pseudorange has much less weight in the RETICLE Kalman filter. Furthermore, since multipath is in general different from station to station, the effect can be expected to average out for tracking situations with a sufficient depth-of-coverage.

Assumption 4 does also not restrict the applicability of the simplified concept. The assumption of a perfect satellite clock simply defines the reference solution to zero but every other reference solution would be possible without changing the results. The reasoning holds also for Assumption 6. The assumption of a perfect clock for the ground station is necessary to eliminate this parameter from the equations. In the true applications, the receiver's clock offsets are of course additional estimation parameters. In this case, the receiver clock would be determined from the average common offset of all satellite pseudorange and carrier-phase measurements. Therefore, the projected orbit error of a single satellite cannot be expected to be completely absorbed in this parameter.

The last assumption that no cycle slips occur over the entire pass (assumption 5) is not realistic, especially for satellites at low elevations. However, in case of loss-of-lock on the carrier-phase, the ambiguities are simply re-estimated based on the clock estimates, which are still provided with the measurements from other stations. This justification leads to another significant difference between the example and the real scenario: A satellite is in general tracked by several stations simultaneously, code and phase measurements are jointly processed and the ambiguities are not initialized instantly, but converge over a longer time interval. Since the pseudoranges are unambiguous and several stations observe a satellite at the same time from different viewing angles, the effect of the projected orbit errors would be assumed to average out if the clock estimates would solely be based on these observations. However, the key information to be kept in mind is the reduced weight of the pseudoranges compared to the carrier-phases. Therefore, the accumulating biases will lead to increasing pseudorange residuals. Due to the small weight of these observables, the clock estimates are not significantly corrected in the Kalman filter update albeit the residual. Contrary to the simplified example, however, the clock biases will not grow indefinitely but will become bounded by the pseudorange update once the residuals have reached a certain magnitude.

Finally, the convergence of the carrier-phase ambiguities in the filter does not happen instantly, but over a longer time. However, this effect does also not contradict the reasoning of the simplified example. The information about the ambiguity for a newly acquired satellite is built up during the measurement update of the carrier-phase ob-

servation. Once again, the small weight of the pseudorange observations impedes an unbiased estimation of the ambiguities, which would be possible from the difference of code and carrier-phases since the projected orbit errors cancel. Instead, the biased GPS clock estimates are likely to transfer a large part of the biases into the ambiguities upon the handover of the satellite to the new station.

Prior to concluding the discussion about the origin of the accumulating clock biases, another example shall be presented here, which further supports the findings. The plot in Fig.4.19 shows the clock estimation error of PRN03 with respect to the CODE final clock on Aug. 17th, 2009. The clock shows a significant offset of about 1 m. Fig. 4.18 has already shown that this satellite was affected by an along-track error on the previous day, which has caused the clock offset to accumulate. At approximately 4:15h, an interruption of the internet connection cuts off the filter shortly thereafter from the NTRIP streams. This interruption of the continuous data stream causes all carrier-phase ambiguities in the filter to be re-initialized, which also results in a reset of the corresponding covariance information to the a-priori covariance. As a result, the pseudorange observations gain a higher impact compared to the carrier-phases, whose covariance information must be rebuilt. Obviously, the clock bias vanishes during the measurement updates following the ambiguity reset.

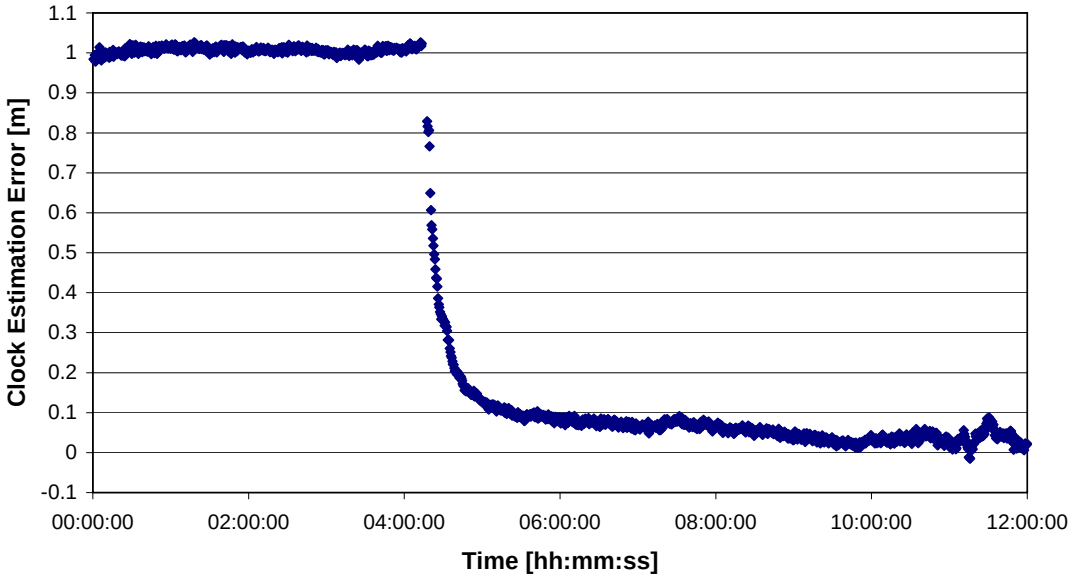

Fig. 4.19: Clock estimation error of G03 on Aug. 17th, 2009. Reference clock solutions is the corresponding CODE final product.

Having discussed the origin of the along-track biases leaves only the cause of the cross-track biases to be explained. Again, the situation shall be demonstrated with a very simplified model, which is depicted in Fig. 4.20. The plot shows a top-view on a tracking scenario involving three ground stations and a single satellite with a cross-track orbit error. The same assumptions used for the previous example shall be used here as well. It shall also be assumed that the orbit errors are many orders of magnitude smaller than the receiver-satellite range, which means that the satellite trajectory is assumed to be high up above the drawing plane. Therefore, the error of the modeled range is simply the projection on the line-of-sight vector and shall be denoted again as a.

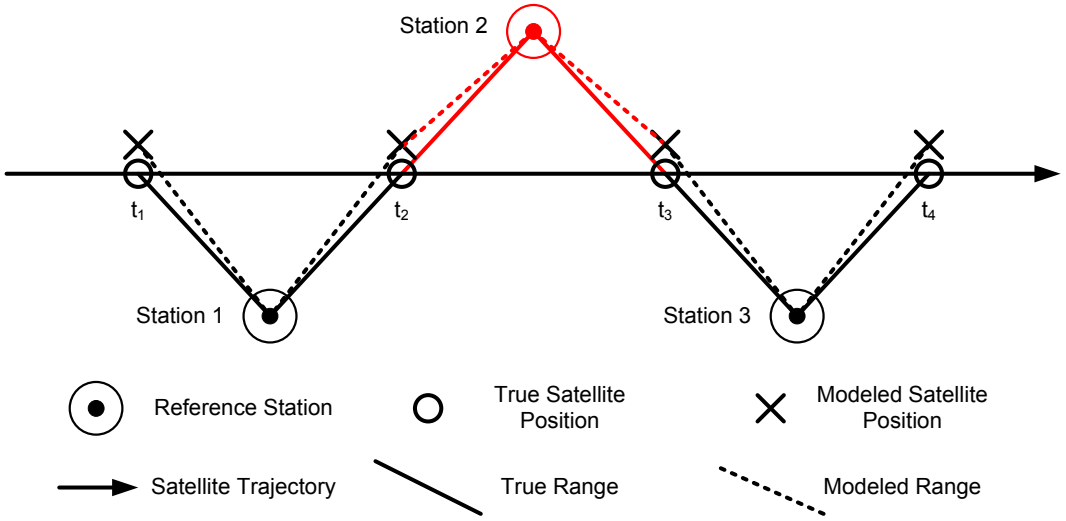

Fig. 4.20: Simplified observation geometry for multiple receivers and a single satellite with constant cross-track orbit error. The satellite trajectory is assumed to be high above the drawing plane.

Starting at epoch t_1 we can find the following modeled pseudorange and carrier-phase equations:

$$\rho_1(t_1) = r + a - c\delta t^{(s)}(t_1) \tag{4.63}$$
$$\Phi_1(t_1) = r + a - c\delta t^{(s)}(t_1) - A_1 \tag{4.64}$$

With the help of the two corresponding observations, the satellite's clock offset and the carrier-phase ambiguities can be determined:

$$c\delta t^{(s)}(t_1) = a \tag{4.65}$$
$$A_1 = 0 \tag{4.66}$$

The major difference to the along-track orbit error scenario becomes obvious when we proceed to time t_2. At this epoch, we have one carrier-phase observation from station 1 and station 2 available:

$$\Phi_1(t_2) = r + a - c\delta t^{(s)}(t_2) - A_1 \tag{4.67}$$
$$\Phi_2(t_2) = r - a - c\delta t^{(s)}(t_2) - A_2 \tag{4.68}$$

Note that the sign of the orbit error projection a has not changed during the pass over station 1 from t_1 to t_2. It is different for station 2 at t_2, however. According to assumption 5, we still know the carrier-phase ambiguity A_1 and can therefore determine the satellite's clock offset as well as N_2:

$$c\delta t^{(s)}(t_2) = a \tag{4.69}$$
$$A_2 = -2a \tag{4.70}$$

Finally, epoch t_3 yields again two equations for the clock offset and the carrier-phase ambiguity:

$$\Phi_2(t_3) = r - a - c\delta t^{(s)}(t_3) - A_2 \tag{4.71}$$
$$\Phi_3(t_3) = r + a - c\delta t^{(s)}(t_3) - A_3 \tag{4.72}$$

which can be solved for $\delta t^{(s)}$ and A_3:

$$c\delta t^{(s)}(t_3) = a \tag{4.73}$$

$$A_3 = 0 \tag{4.74}$$

For this simple example we gain a clock offset, which is constantly offset by a and carrier-phase biases, which alternate from station to station between 0 and $2a$. Tab. 4.5 summarizes the results for this scenario.

Tab. 4.5: Clock offset and ambiguity estimation results for simplified cross-track error scenario in Fig. 4.20

Epoch	t_1	t_2	t_3	t_4	t_5
$c\delta t^{(s)}$	a	a	a	a	$\cdots$
A	0	-2a	0	-2a	$\cdots$

Reviewing the results for the test case with artificial cross-track errors shows, that the clock estimates are in fact affected by an offset. Fig. 4.16 depicts the biased clock for this case. According to the previous discussion of the simple scenario, the clock bias is determined by the initial viewing geometry for the affected satellite, when the carrier-phase ambiguities are not yet converged. Once the ambiguities have converged, the bias is fixed in the estimated clock offset and handed over from station to station. The important difference with respect to the along-track error scenario is, however, that the sign of the orbit error projection remains preserved during a pass over a station in this case. As a result, no accumulating effects can be observed.

Finally, both Fig. 4.15 and Fig. 4.16 exhibit comparably small variations of the clock estimation errors on top of the linearly growing or constant bias, respectively. These variations can be explained with the changing geometry of the satellite visibility from a non-uniformly distributed tracking network. As the satellite moves along the orbit, the projected error on the line-of-sight vector changes, resulting in a variation of the clock error. These variation have been omitted in the discussion of the simplified scenarios in favor of the clearness of the main effects.

4.5.3 Methods for Mitigation

The effects of radial, along-track and cross-track orbit errors on the clock estimation have been introduced in the previous section. Especially the accumulation of clock estimation errors, which has been discovered to originate from the along-track orbit errors, poses a problem to the filter and should possibly be avoided. In this section, solutions to this issue are introduced.

The most thorough solution to this problem would be to utilize improved orbit predictions. The orbit error should ideally be reduced until its projection on the line-of-sight does not significantly exceed other measurement or model errors. The most effective measure to achieve this goal is to decrease the update interval and the latency of the orbit prediction. The currently available Ultra-Rapid predictions represent the achievable prediction accuracy over 9 hours, taking into account the latency of 3 hours.

A higher update rate and shorter latency would require all agencies to adjust the submission of their input product for the IGU combination accordingly. Alternatively, an independent orbit prediction product could be generated exclusively for RETICLE. Other agencies, which participate in the real-time pilot-project, have adopted this procedure. It turns out, however, that the implementation of an orbit prediction system is beyond the scope of this dissertation. Therefore, a practical solution must be found, which can cope with the current orbit prediction errors of the IGUs.

It has been shown in the analysis, that the change of the projected along-track orbit errors cannot be compensated for by any estimation parameters and is thus moved into the satellite clock. The pseudorange residuals will grow over time. However, these observables have a higher noise and thus have a lower weight in the filter. A straightforward solution is to compensate the changing orbit-errors by an estimation parameter. A feasible solution is to combine this parameter together with the carrier-phase ambiguities. In order to compensate for the change of the bias when the satellite passes over the ground station, process noise must be added during the covariance update on the ambiguities. As a result, the carrier-phase ambiguities are no longer regarded as constant parameters, but are adjusted depending on the amount of process noise applied. The advantage of this approach is that no additional estimation parameters must be introduced in the filter state. Therefore, the computation time required for the Kalman filter loop remains unchanged. The drawback is that the weight of the precise carrier-phase observations is reduced, depending on the amount of process noise applied. In order to keep this adverse effect as small as possible, the variance is scaled with the elevation of the satellite. Obviously, the change in the projected orbit error is higher at low elevations, whereas satellites at high elevation are hardly affected. The following equation can thus be obtained for the process noise of the ambiguities q_N, which is characterized with a standard deviation σ and a time constant τ:

$$q_N = \frac{\sigma_N^2 \Delta t}{\tau_N} cos\,(E) \tag{4.75}$$

The elevation angle of the corresponding satellite is denoted E. The process noise for the ambiguities is added on the main diagonal of the elements of Eq. 4.44. No additional modifications of the Kalman filter equations are necessary. In order to prove, that the process noise on the ambiguities indeed removes the accumulating biases, simulations with applied process noise have been performed. The Kalman filter settings for these simulation are summarized in Tab. 4.6. A standard deviation of 1 mm over a time interval of 30 s has been selected for the ambiguity process noise. The orbit errors and all other Kalman filter settings used for this simulation are identical to the previous example.

The results for the along-track orbit error of 30 cm are depicted in Fig. 4.21. The plot shows the error of the real-time clock with respect to a CODE reference solution over 24h hours. Obviously, the clock is affected by a small bias, but no accumulating effects like those in Fig. 4.15 are visible any more. The same results are also obtained for other satellites with different magnitude and sign of the tangential orbit error. Of course, for significantly larger orbit errors, the applied process noise is not sufficient and a slowly increasing bias can again be observed. However, long term results of the

Tab. 4.6: Filter settings for simulation with ambiguity process noise

Process Noise:	σ_0	σ	τ
GPS clock offset	5 m	0.05 m	600 s
GPS clock drift	0.005 m/s	0.0005 m/s	900 s
Rcv clock offset	100 m	100 m	100 s
Tropospheric zenith delay	0.5 m	0.002 m	3600 s
Ambiguities	5 m	0.001 m	30 s
Measurement Noise:			
Pseudorange		1.0 m	
Carrier Phase		0.01 m	
Clock Constraint		0.1 m	

operational RETICLE filter show, that the selected process noise setting is sufficient to cope with the existing along track errors.

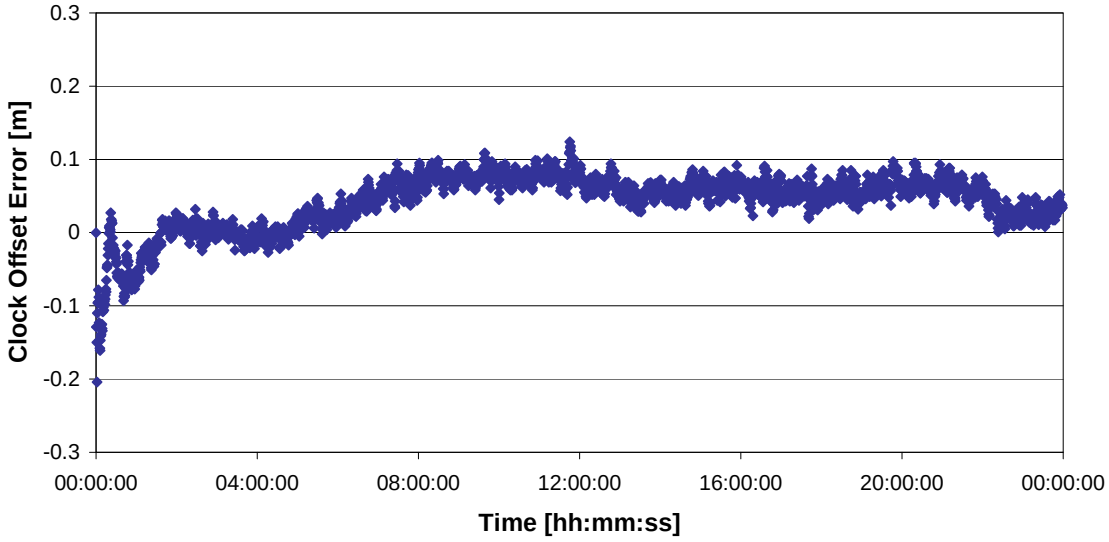

Fig. 4.21: Clock estimation errors for PRN13 with respect to the CODE rapid clock. An artificial along–track orbit error of 30 cm has been applied to the satellite orbit. Process noise is applied on the ambiguities in the Kalman filter.

The plot in Fig. 4.22 depicts the clock estimation errors for the satellite with the cross-track error. It turns out that the bias is still present in the estimation results. However, a more pronounced variation of the clock is visible. This results seems reasonable, however, since the initial clock bias for the cross-track orbit errors results from the observation geometry. With process noise on the ambiguities, the estimated clock is less "stiff" and more likely to exhibit temporal variations.

It can be summarized that the constant biases still remain in the estimated clocks despite the inclusion of process noise. However, the accumulation of clock errors could be avoided for tangential orbit errors. For the less critical case of the cross-track errors, the additional process noise does neither cause a significant improvement nor a major degradation. After these encouraging results, process noise was also implemented on the operational RETICLE filter. Results from the IGS real-time pilot project presented

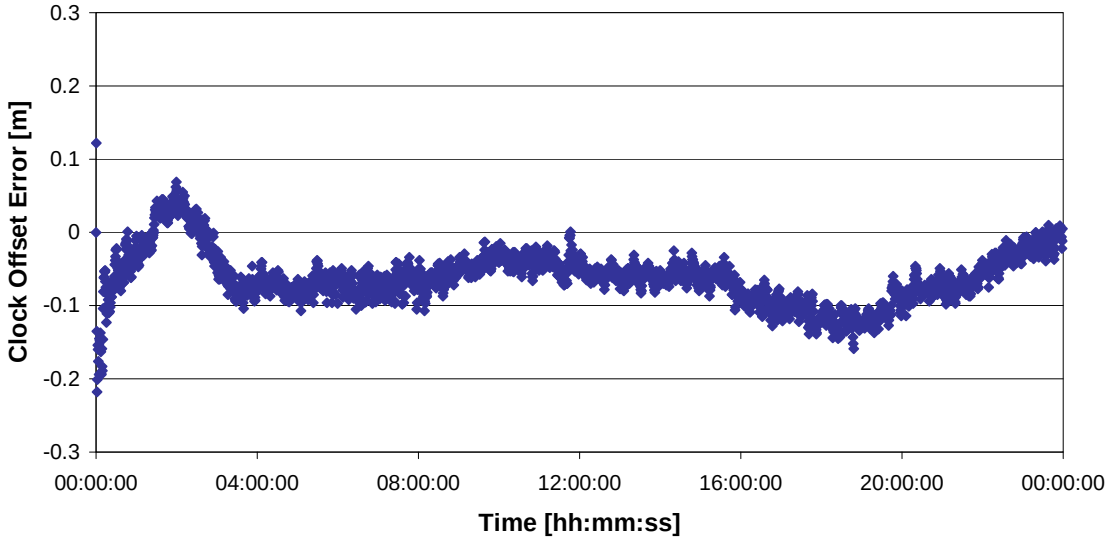

Fig. 4.22: Clock estimation errors for PRN14 with respect to the CODE rapid clock. An artificial cross–track orbit error of 30 cm has been applied to the satellite orbit. Process noise is applied on the ambiguities in the Kalman filter.

in Chap. 6 will demonstrate that the biases in the clock estimates have been significantly reduced after this change. The price to be paid is a minor increase in the noise of the estimated clocks.

Though the solution presented here has been proven to be suitable, a more sophisticated method should also be feasible. As already indicated, systematic errors should best be modeled or included as estimation parameters in the filter state. Since the unknown orbit errors cannot be modeled, of course, the only feasible approach is to estimate them along with the clock offset parameters. For a full 3-D orbit correction, however, this would add three additional states per satellite to the filter state. Besides a significant increase in processing time, another drawback is obvious: if the tracking network remains unchanged, the same amount of information from the measurements must be distributed to an increased number of estimation parameters. Strong correlations between these parameters, like for the radial orbit error and the clock, may cause problems with the estimation.

As a compromise, only the along-track orbit error component could be added to the filter state. This would increase the state vector only moderately, but remove the most troublesome error from the estimation. Furthermore, the process noise on the ambiguities could again be removed, since an estimation parameter for the orbit error exists in this case. It should be investigated if a reliable estimation of the along-track orbit errors is indeed feasible and if better clock estimation results can be obtained compared to the method with ambiguity process noise.

5. Performance Assessment with Precise Orbit Determination

In this section, precise orbit determination results obtained with real flight data from a LEO-satellite are presented. The RETICLE products have been used for the POD and the resulting LEO-orbits are compared to a reference solution. Sec. 5.1 describes different approaches for the assessment of the clock accuracy. The following Sec. 5.2 introduces the orbit determination strategy adopted for this analysis. Finally, Sec. 5.3 compares the different orbit solutions and provides a discussion of the results.

5.1 Clock Accuracy Assessment

The assessment of an orbit- and clock-product can be done with different approaches. The most straight-forward method is to directly compare the orbit and clock information with a reference product. The IGS final product or one of the final products of an IGS analysis center can serve as a reference here. From the comparison, statistics like mean and standard deviation can be derived. These statistics are certainly useful for the comparison of different clock products, however, information about the expected position accuracy cannot be directly deduced.

The Signal-In-Space Range Error (SISRE) tries to overcome this deficiency [Warren and Raquet, 2003]. This quantity is a coarse measure of the errors in the satellite ephemerides which affect the computation of the user position. It depends only on the accuracy of the orbit- and clock-product which is used to compute the navigation solution.

The computation of the SISRE for a single satellite i is based on the radial, cross-track and along-track orbit errors denoted as e_R, e_C and e_A, respectively, and the clock error e_{cdt}. The orbit and clock correction errors are computed with respect to a reference solution of significantly higher accuracy. It should be noted that the antenna offset vectors, which are used for the computation of the clock correction errors, must be consistent with the ones used for the orbit and clock product to be assessed. Therefore the clock correction error term is computed according to

$$e_{cdt}^{(i)} = \left(dt_a^{(i)} - dt_b^{(i)} \right) c + \left(a_{z,a}^{(i)} - a_{z,b}^{(i)} \right) \tag{5.1}$$

where dt_a and dt_b are the clock correction terms and $a_{z,a}$ and $a_{z,b}$ are the corresponding antenna offsets from the spacecrafts center of mass to the antenna reference point in the spacecraft z-direction. The effect of the radial orbit error and the clock correction error results in the combined error $e_{RC}^{(i)} = e_R^{(i)} - e_{cdt}^{(i)}$. The SISRE of a satellite can be found

from the following equation using the properties defined previously:

$$\mathrm{SISRE}^{(i)} = \sqrt{\mathrm{rms}\left(e_{RC}^{(i)}\right)^2 + \frac{1}{49}\left(\mathrm{rms}\left(e_{C}^{(i)}\right)^2 + \mathrm{rms}\left(e_{A}^{(i)}\right)^2\right)} \tag{5.2}$$

In this equation the $\mathrm{rms}\,()$-terms denote the values of many individual orbit and clock errors over the time interval of interest. Since the combined errors in the satellite clock and the radial orbit error have a larger impact on the user ranging error than the orbit error in the cross-track and along-track directions, they are scaled by a factor of 1/49. The scaling factor is the square of the sine of the average angle between the radial direction and the line-of-sight directions for Earth-bound users. An issue associated with the formula stated above is, that radial orbit offsets or clock errors, which are common to all satellites in the constellation, affect the computed SISRE value. In a navigation solution, these common errors would be absorbed into the user's clock correction values and do not affect the position. Therefore, the mean values of the orbit and clock errors of the complete constellation at the same epoch must be subtracted prior to the computation of the RMS in Eq. 5.2. Denoting these mean pseudorange errors over the complete constellation at each epoch with $\bar{e}_{RC}^{(i)}$, Eq. 5.2 can be rewritten in the following form using the corrected range error $\tilde{e}_{RC}^{(i)} = e_{RC}^{(i)} - \bar{e}_{RC}^{(i)}$:

$$\mathrm{SISRE}^{(\mathrm{i})} = \sqrt{\mathrm{rms}\left(\tilde{\mathrm{e}}_{\mathrm{RC}}^{(\mathrm{i})}\right)^2 + \frac{1}{49}\left(\mathrm{rms}\left(\mathrm{e}_{\mathrm{C}}^{(\mathrm{i})}\right)^2 + \mathrm{rms}\left(\mathrm{e}_{\mathrm{A}}^{(\mathrm{i})}\right)^2\right)} \tag{5.3}$$

Eq. 5.3 provides more realistic results for the SISRE. The mean value of all SISRE of the complete constellation is then used as a the measure to assess the accuracy of the product.

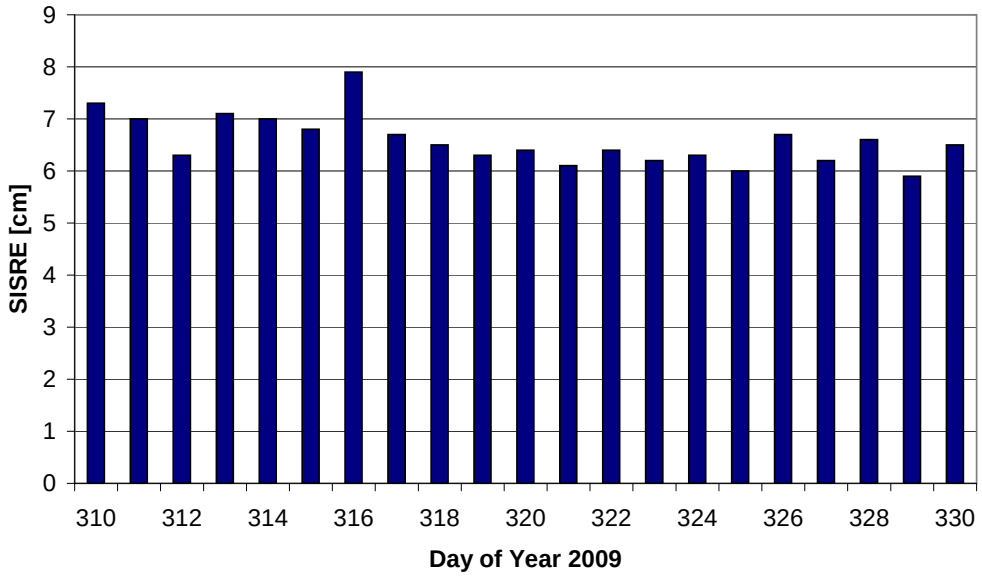

Fig. 5.1: SISRE for RETICLE products for November 6-26, 2009

The Signal-in-Space Range Error for the RETICLE products has been computed with respect to the CODE final products for the selected test period between November

6th and November 26th of 2009. The results are depicted in Fig. 5.1. It is obvious, that most of the time the SISRE varies between 6-8 cm. Day 316 has the highest SISRE with close to 7.9 cm. Closer inspection of the clock errors for this particular day reveals that the clock accuracy is degraded between 3h UTC and 6h UTC.

Experience shows that the SISRE results for the expected positioning accuracy are rather pessimistic, if precise point positioning with carrier-phase positioning is performed. However, it is certainly still a convenient and quick measure for a first characterization or coarse quality check of orbit/clock-products. More meaningful results are obtained by using the products for positioning and comparing the results to a reference solution. This approach is described in the next sections.

5.2 Orbit Determination Procedure

The orbit determination procedure adopted for this analysis has been designed to reflect the situation of a near real-time POD scenario as closely as possible. The GPS measurements used for the analysis stem from the German LEO satellite TerraSar-X. It has been launched on June 15th, 2007 into a sun-synchronous orbit with 97° inclination. The main payload is a synthetic-aperture-radar for high-quality cartography of the Earth's surface. The satellite is equipped with three GPS receivers: Two MosaicGNSS single-frequency receivers are used for the on-board navigation. Additionally, the Integrated GPS and Occultation Receiver (IGOR), has been contributed to the mission by the GeoForschungsZentrum (GFZ) Potsdam. The IGOR is a dual-frequency space-grade receiver manufactured by Broadreach Engineering, based on JPL's BlackJack receiver. It allows the connection of four antennas, which can either be used for navigation or for occultation measurements. On-board TerraSAR-X, two antenna inputs are connected to zenith pointing antennas for navigation purposes. The remaining two inputs are fed by the occultation antennas, which point into the flight- and anti-flight-directions of the satellite. The receiver has in total 48 independent channels, which can be grouped to 3 $\times$ 16 channels to track C/A, P1 and P2 signals [Montenbruck et al., 2006]. Fig. 5.2 depicts TerraSAR-X during ground testing. The two zenith-pointing choke-ring antennas are visible in the upper half of the satellite structure. The IGOR receiver is shown in Fig. 5.3. For the analysis in the following sections, measurements collected with one of the zenith-pointing antennas have been used.

The orbit determination procedure done for the analysis has been performed with the "GPS High Precision Orbit Determination Tools (GHOST)" [Montenbruck et al., 2005b] and consists of several steps, which are depicted in Fig. 5.4 and shall be shortly explained here. At the beginning, an a-priori trajectory has been computed with the single point positioning routine "SPPLEO". The algorithm only uses pseudorange-measurements and no dynamic model for the spacecraft trajectory. In a consecutive step, this coarse trajectory is smoothed using the "PosFit" software, which employs a reduced-dynamical model of the satellite's orbit. This smoothed trajectory is finally used for the precise orbit determination, which is performed by RDOD with a Least-Squares-Adjustment based on a reduced-dynamic model. The attitude information for the LEO spacecraft is provided by quaternions. The modeling of the GPS measurements comprises phase center offsets and variations for transmitting as well as receiving an-

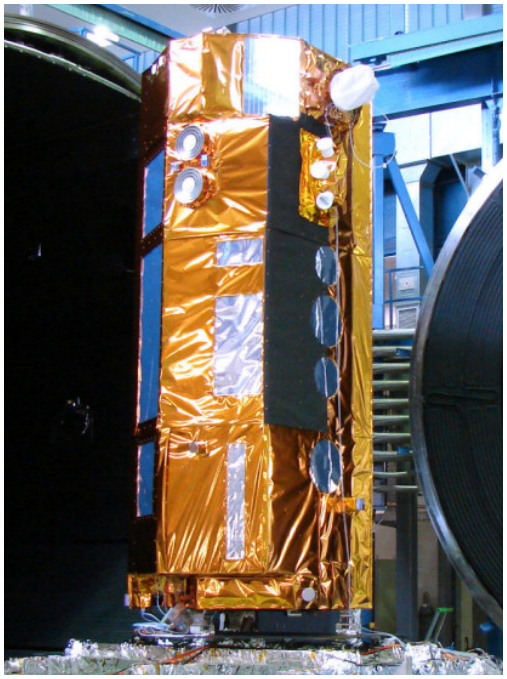

Fig. 5.2: TerraSAR-X satellite during ground tests (imagery courtesy of IABG)

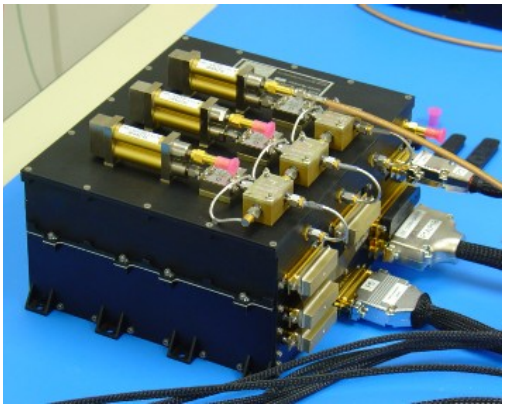

Fig. 5.3: IGOR receiver (imagery courtesy of DLR)

tennas and carrier-phase wind-up corrections. The gravitational force of the reduced dynamic model for the spacecraft trajectory is based on Earth's gravity field model UT/CSR GGM01 with 100x100 terms. Additionally, solid Earth tides and pole tides are used together with ocean tides based on the UT/CSR TOPEX_3.0 model. Third body accelerations of the sun and the moon are based on analytical ephemerides. The non-gravitational forces comprise the Jacchia-Gill atmospheric density model and a cannonball solar radiation pressure model. Empirical acceleration parameters in the x-, y- and z-axes are estimated at intervals of 10 minutes in order to compensate for non-modeled forces. Additionally, two constant scaling factors for the solar radiation pressure model and the atmospheric drag model are estimated. The estimation parameters also comprise the satellite position- and velocity-vector at the initial epoch, which is propagated with the dynamical model. The receiver clock offsets are estimated at each epoch. Finally, the carrier-phase biases of the ionosphere-free combination are estimated as constant parameters for periods of un-interrupted carrier-phase-tracking [Montenbruck et al., 2005b].

In addition to the dynamic orbit determination, a kinematic orbit determination "KIPP" procedure has been employed. The main difference to the reduced dynamics approach is the absence of a dynamical model. Instead of estimating the initial position and velocity vector via the dynamic model, the kinematic approach estimates the satellite's position at each epoch individually. The estimation vector thus consists of position vector and receiver clock offset for each epoch and again the carrier-phase biases, which are held constant over a satellite pass unless cycle-slips occur. The kinematic orbit determination is appealing for the assessment of the orbit- and clock-product

performance, since the resulting LEO orbit will be more directly affected by errors in the satellite clock estimates.

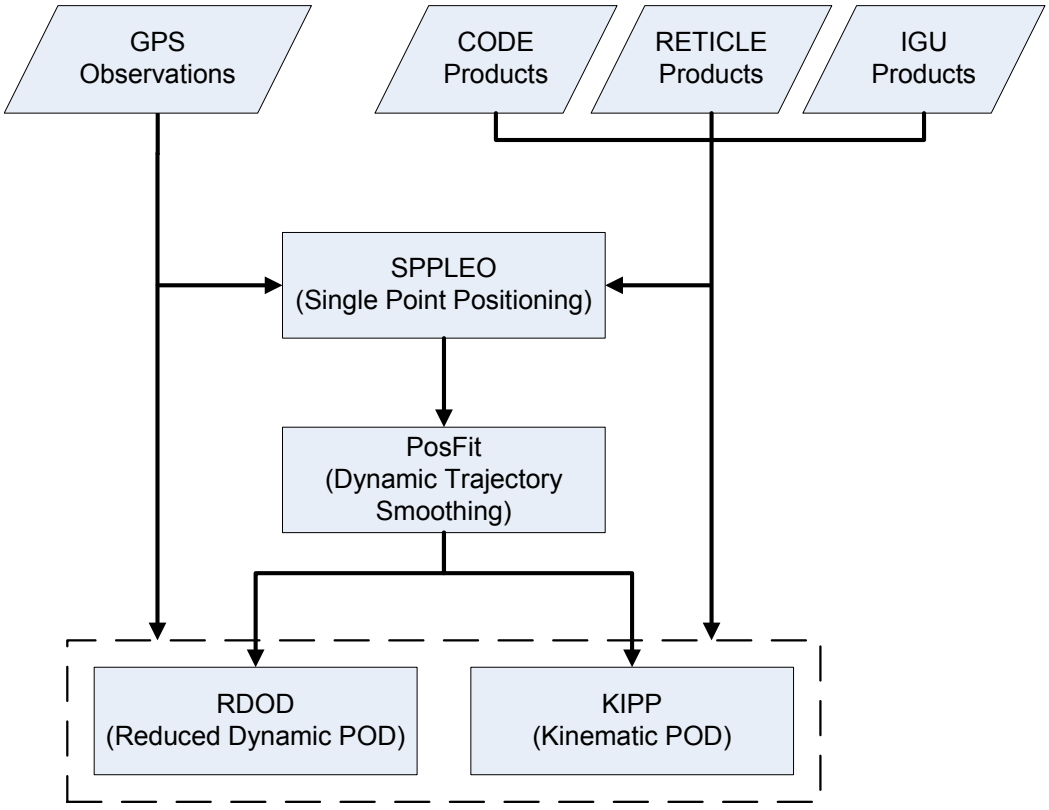

Fig. 5.4: Flowchart of the precise orbit determination process

The reference solution for the orbit comparisons in the next section has been computed with the aforementioned procedure using data arcs of 12 hours and CODE final orbit- and clock-products. The middle part of these orbits serves as a reference solution. Near real-time processing simulations have been performed with the RETICLE products and the IGU predicted products. The POD process was started at 90 minute-intervals, resulting in 16 POD-runs per day, with a data-arc length of 12 hours. This corresponds to the typical repetition rate of a LEO-satellite on a polar orbit and a single ground-station at high latitudes. The processing time of the POD-chain is on the order of 3-4 minutes, thus it would be possible to deliver the derived products with a sufficiently short latency. The final 90-minutes of the RETICLE-based orbits are then compared to the middle part of the CODE-based reference orbit. This is to ensure that the best possible solution is selected as a reference, which is not affected by a possible degration at the beginning and the end of the Least-Squares solution. Besides the RETICLE-product, the IGU predicted products are also used for near-real-time simulations to show the improvement gained by GPS clock offset estimation rather than prediction.

5.3 POD Results and Comparisons

5.3.1 Reduced Dynamics Orbit Determination

The results for the TerraSAR-X orbit derived with RETICLE orbits are depicted in Fig. 5.5. The plot show the 3-D RMS of the orbit errors for each POD run of the selected test period. The plot reveals that the RETICLE-derived orbits agree to better than 10 cm for the entire test period. The typical errors are between 1 cm and 5 cm. A single POD-run on day 313 exhibits a comparably high position error of 9.8 cm. Nevertheless, it can be seen that the RETICLE clock product enables a repeatable orbit determination with high accuracy.

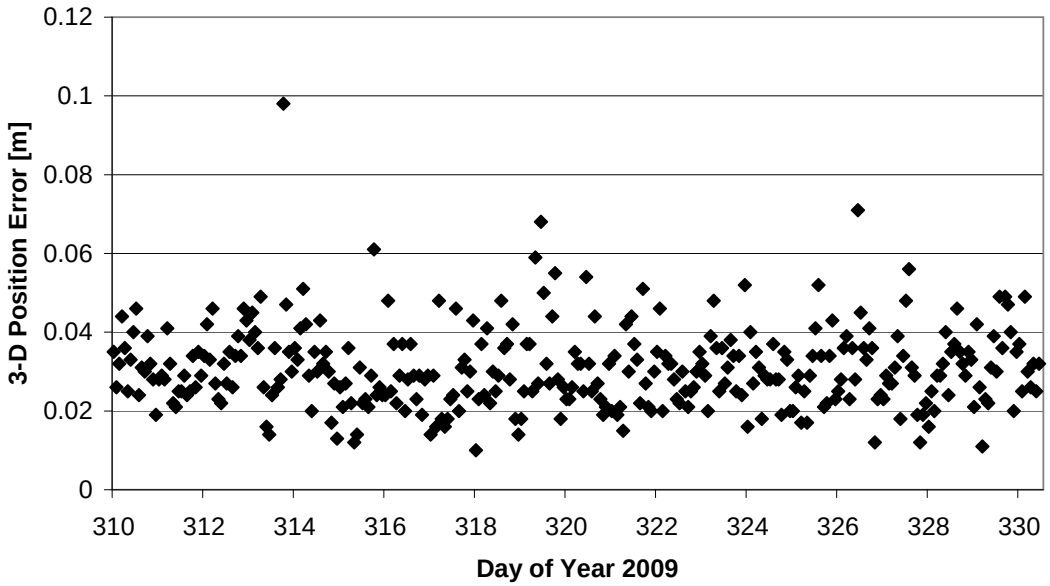

Fig. 5.5: 3-D RMS position errors of near-real-time TerraSAR-X orbits with RETICLE products. The final 90-minutes are compared to the reference solution.

For comparison, Fig. 5.6 depicts the 3-D RMS orbit errors for the TerraSAR-X orbits derived with IGU predicted products. Note that the scale is different from Fig. 5.5. It becomes obvious that the position errors vary between 8 cm and 55 cm over the complete period. It must be kept in mind that the RETICLE orbit product uses exactly the same orbit as the IGU predictions. Therefore, the performance increase is entirely caused by an accuracy improvement of the satellite clock offset.

It becomes obvious that the reduced dynamics orbit determination exceeds the performance expectation derived with the SISRE computed in Sec. 5.2, which vary between 6-10 cm. This can mainly be attributed to the dynamic model and the use of carrier-phase observations. The spacecraft positions are not independently estimated, but coupled via the dynamic model. Therefore, errors in the GPS satellites' clock offsets, which affect the positioning solution, have a less pronounced effect. Furthermore, the carrier-phase float ambiguities allow the compensation of biased GPS clock estimates. The precise orbit determination benefits extensively from the high precision of the carrier-phase measurements, which are weighted higher than the pseudorange observations. The effect of GPS clock offset biases can be eliminated by the ambiguity

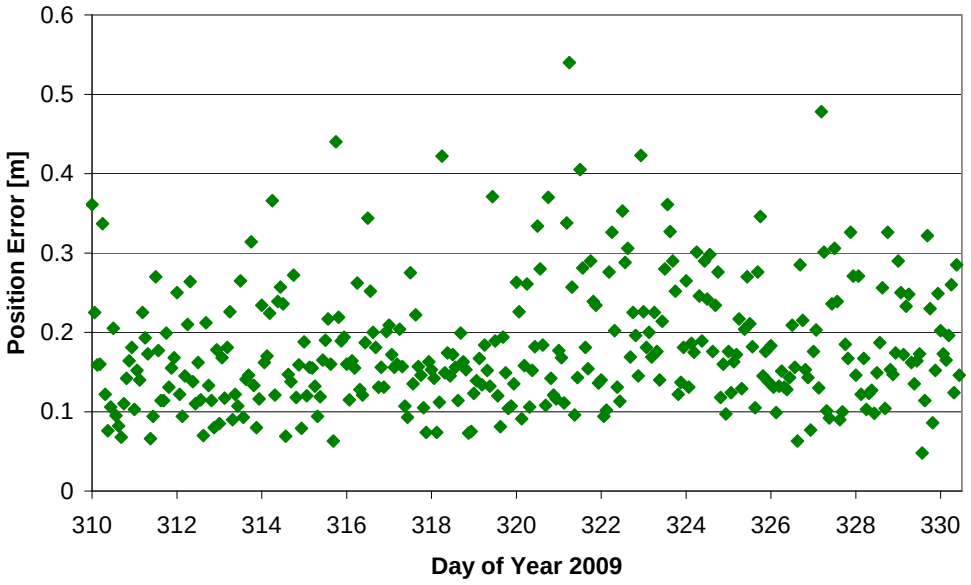

Fig. 5.6: 3-D RMS position errors of near-real-time TerraSAR-X orbits with IGU predicted products. The final 90-minutes are compared to the reference solution. Note the different scale on the ordinate compared to Fig. 5.5.

estimation, as long as the biases are constant over the duration of the pass, which is usually on the order of 10-40 minutes.

An example for the latter effect has been demonstrated by Hauschild and Montenbruck [2009]. Here, the POD performances of several (near) real-time orbit and clock products have been compared directly. Some results are summarized in Tab. 5.1. The first product in Tab. 5.1 is a near real-time product from the Astronomical Institute of the University Berne (AIUB), which was computed from 90-minute batches of GNSS observations [Bock et al., 2009]. The DLR product originated from an offline Kalman filter, which has been developed as a demonstrator for the later real-time system RETICLE. ESOC produces a dedicated orbit/clock-product for the MetOP mission, which is created in batch-mode. This product is different from ESOC's contribution to the real-time pilot project. The fifth product stems from JPL's GDGPS. Finally, the IGU predicted orbits have also been used.

Tab. 5.1: SISRE and MetOp-A POD results for different (near) real-time orbit/clock products, 24h POD on 2006/12/26 [Hauschild and Montenbruck, 2009].

Product	SISRE	3D RMS Pos. Error	RMS CP Resid.	Passes
AIUB	13.5 cm	2.6 cm	7.5 mm	426
DLR	6.5 cm	4.6 cm	14.0 mm	385
ESOC	8.9 cm	6.3 cm	18.0 mm	377
JPL	9.0 cm	7.8 cm	24.0 mm	393
IGU	72.0 cm	24.0 cm	50.0 mm	470

Tab. 5.1 shows the SISRE and the 3D RMS errors of the derived orbits for the MetOp-A satellite. Furthermore the GPS satellite passes are listed, which denote the number of un-interrupted carrier-phase tracking periods. Obviously, the AIUB product exhibits the largest SISRE with 13.5 cm, but it has the best orbit determination perfor-

mance of all products. The reason for this unexpected behavior is, that the individual batches of GPS clock-offset estimates have been produced without overlap. As a result, the clock estimates exhibit significant discontinuities every 90 minutes on the order of several decimeters. This caused the orbit determination algorithm to detect a cycle-slip of the carrier-phase observations and re-initialize their ambiguity. The newly estimated ambiguities would then compensate the new GPS clock offset bias. The notably increased number of passes, which are obtained with the AIUB-product compared to the other real-time products, confirms this observation.

Though being affected by biases and discontinuities of the GPS clock estimate, the AIUB product still enables the best performance in a 24 hour POD. Therefore, the relative evolution of the GPS clocks over time seems to be best represented by this product. This assumption is supported by the low RMS residuals of the carrier-phase observations. For the AIUB product, the residuals are only 7.5 mm and significantly lower than the residuals of all other products. They come close to the residuals of the CODE final reference product, which amount to 6 mm. The small difference is not surprising, however, since the CODE final product as well as the AIUB near real-time product have both been generated with the Bernese high precision GNSS processing software [Hauschild and Montenbruck, 2009]. Obviously, the short-arc GPS clock products derived with Bernese reach a comparable accuracy for the short-term clock behavior as the products from daily batches of observations. The accuracy of the clock's short-term behavior appears to be the key requirement for precise orbit determination with float-ambiguity estimation.

The consideration of the residuals for pseudorange and carrier-phase measurements can also help to gain more insight into the quality of the TerraSAR-X orbit determination. Fig. 5.7 depicts the residuals for the pseudorange observations of every POD for the entire test period. The residuals have been computed with respect to the trajectory obtained from RDOD. Measurements, which have been rejected during the data editing, are not included in the statistics. The plot shows the residuals of the RETICLE-based and IGU-based orbit determination as well as the residuals for the reference solution with CODE final products. It can be seen that the RETICLE-product and the CODE-product have nearly identical residuals on the order of 60 cm. The residuals for the IGU product have a mean value of about 1.1 m and show large variations between 85 cm and 1.4 m.

The carrier-phase residuals are shown in Fig. 5.8. The residuals obtained with the CODE-product are on the order of only 3-4 mm. These low residuals are close to the measurement precision of the IGOR receiver. This is an expected result, since empirical corrections for the antenna phase pattern based on in-flight data have been applied [Montenbruck et al., 2009a]. The residuals of the different POD runs exhibit a high repeatability with variations of typically less than a millimeter. The RETICLE-product yields residuals which are about 6-7 mm most of the time, but increase to 10 mm for certain periods. Assuming a constant quality of the receiver's carrier-phase observation, the increased residuals would indicate a lower quality of the RETICLE clock estimates during the time-interval of the affected POD. Finally, the IGU product exhibits the largest residuals, which vary between 40 mm and 80 mm.

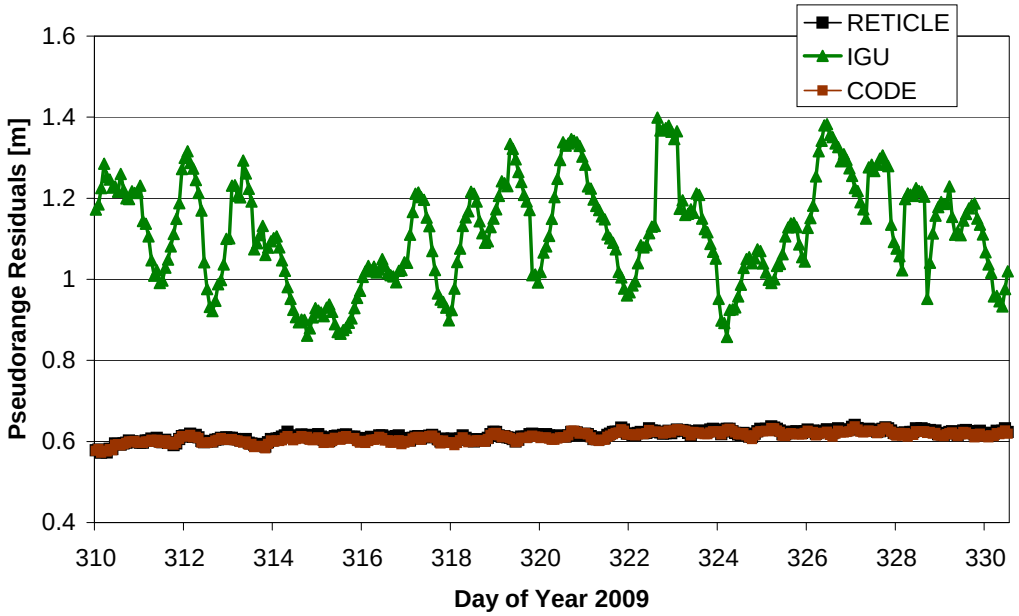

Fig. 5.7: Residuals of the pseudorange measurements from NRT-PODs with CODE-, RETICLE- and IGU-products.

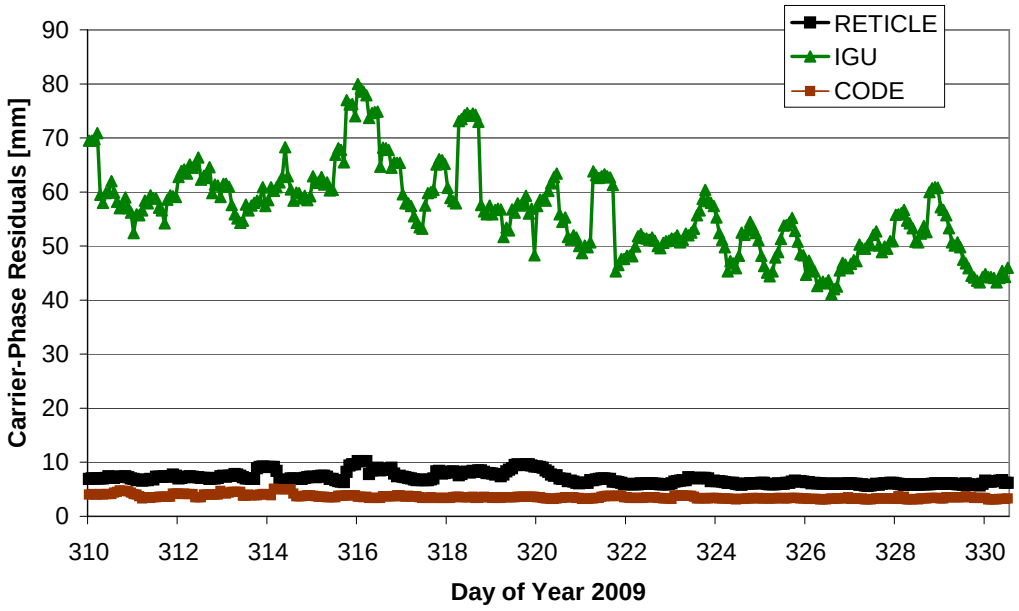

Fig. 5.8: Residuals of the carrier-phase measurements from NRT-PODs with CODE-, RETICLE- and IGU-products.

It has been shown that the carrier-phase residuals are suited not only to assess the accuracy of the observables, but also for an evaluation of the orbit- and clock-product used for the modeling of the observations. The three different products exhibit different levels of residuals, depending on the quality of the combined orbit- and clock-error. For the pseudorange, the CODE- and RETICLE-product showed nearly identical results, which indicates that the residuals are dominated by the receiver noise and that effects of clock-errors are not visible in the plot. The IGU product on the other hand is clearly distinct from the other two products. The residuals of approximately 1.1 m appear reasonable considering that the clock errors of the predictions are on the order of 5 ns (see Tab. 1.1).

For the carrier-phase residuals, the CODE-final product yields the smallest residuals. The RETICLE-product yields the second smallest residuals. The increase in the mean level compared to the CODE products is a manifestation of an increased noise on the real-time clock estimates. Finally, the IGU product yields significantly higher residuals caused by errors in the IGU clock solution. The predicted clocks are not able to follow the short-term behavior of the GPS clocks.

The accuracy of orbit determinations can also be assessed with independent measurements from satellite laser ranging (SLR) stations. For this measurement-technique, a pulsed laser-beam is sent through a telescope on the ground to a spacecraft orbiting the Earth. The laser-beam is reflected at the satellite's laser retro-reflector, which consists of specially shaped glass-prisms. These prisms return the received light in the exact same direction. The beam is received again at the laser ranging station. The two-way time of flight of the laser pulse is then measured and converted into range measurements. The measurements are completely independent of GNSS measurements and have a very high precision of a few centimeters. TerraSAR-X, like many other scientific satellite missions, is equipped with a laser retro-reflector and is routinely tracked by many SLR stations around the world.

Tab. 5.2 lists the mean and standard deviation of the RETICLE-based TerraSAR-X orbit from the near real-time simulations. For the computation of the residuals, the final 90-minutes of the consecutive RETICLE-based PODs have been concatenated. For comparison, the residuals of the TerraSAR-X reference orbit are listed as well. For the RETICLE-based orbit 5013 observations have been used for the statistics in total. For the reference product, 5014 observations are used. This negligible difference is due to the data editing, which rejects some additional observations as outliers for the RETICLE products, and does not affect the statistics. The data editing process sorts out all measurements with an elevation smaller than 10° and all residuals larger than 10 cm. Fig. 5.9 and Fig. 5.10 depict the residuals for both orbits. Note the different scales of the ordinate in both plots.

It becomes obvious that both orbits have negligible mean residuals of only -0.2 cm and -0.3 cm. The standard deviation of the observations is 2.8 cm for the RETICLE-based orbits. The reference product yields a lower mean of 1.7 cm. The direct comparison shows that both orbit-solutions have low and almost equal mean SLR residuals. The standard deviation of the residuals is larger for the RETICLE-based orbit solution. This is an expected result, however, based on the position errors depicted in Fig. 5.5, a higher standard deviation for the SLR residuals could have been expected.

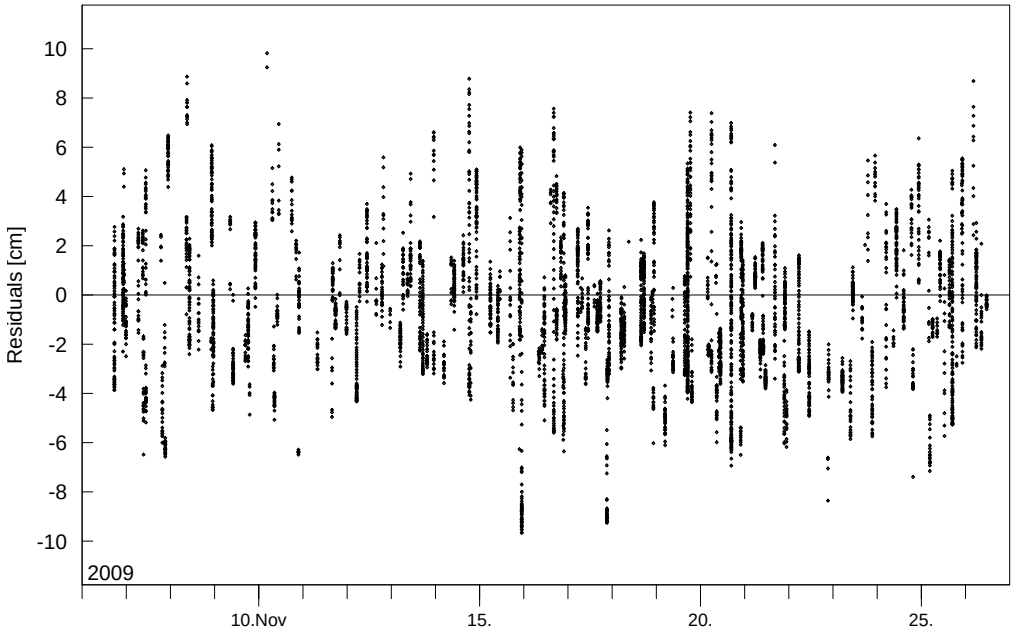

Fig. 5.9: Satellite-Laser-Ranging residuals for RETICLE-based TerraSAR-X orbit, units of the residuals are cm.

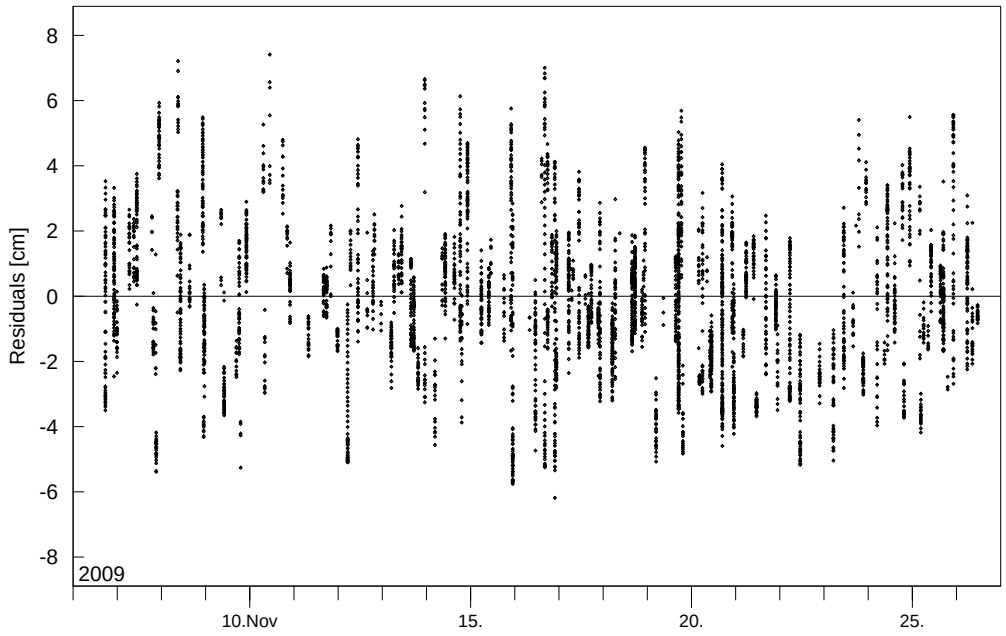

Fig. 5.10: Satellite-Laser-Ranging residuals for TerraSAR-X reference orbit, units of the residuals are cm.

Tab. 5.2: Satellite-Laser-Ranging Residuals for RETICLE-based and reference orbit of TerraSAR-X

	RETICLE		Reference	
Day of Year	Mean [cm]	Std-Dev [cm]	Mean [cm]	Std-Dev [cm]
310	0.6	1.9	0.0	1.1
311	1.2	2.7	0.6	1.4
312	0.2	2.0	0.0	2.0
313	-0.9	2.3	-0.8	1.6
314	0.9	2.5	1.6	1.7
315	0.1	1.6	-0.5	0.9
316	-0.6	2.3	0.1	1.6
317	-0.7	2.5	0.0	1.8
318	0.9	2.1	0.7	1.7
319	-0.5	3.2	0.3	1.2
320	-0.1	2.7	-0.5	1.4
321	0.0	2.2	-0.3	1.5
322	-0.1	1.5	-0.2	1.5
323	-0.4	2.8	-0.5	2.2
324	-1.4	2.1	-1.0	1.8
325	-0.4	1.7	-0.4	1.3
326	-2.1	1.9	-1.7	1.2
327	-0.8	2.4	-1.1	2.1
328	0.4	2.4	0.7	1.7
329	-0.1	2.3	-0.1	1.7
330	-0.7	2.5	-0.1	1.4
Total	-0.3	2.8	-0.2	1.7

In the following, a closer look shall be taken at the individual error components of the RETICLE-based trajectory. Fig. 5.11 depicts the radial, cross-track and along-track orbit RMS errors with respect to the reference orbit. The plot has again been generated from the comparison of the final 90 minutes of the RETICLE-based trajectory to the middle part of the reference orbit. It becomes obvious, that the radial orbit error stays close to 1 cm and rarely exceeds 3 cm during the complete test interval. The cross-track error is the second smallest error component and exhibits variations, which stay below 4 cm with one exception. The orbit determination solution for day 313 with exceptionally high errors, clearly visible in Fig. 5.5, can also be recognized in this plot, where all three error components exhibit increased errors for this particular solution. The along-track error clearly dominates the error budget, but never exceeds 7 cm and is less than 5 cm most of the time. The results depicted in Fig. 5.11 suggest the explanation for the comparably small difference of the standard deviation of the SLR residuals in Tab. 5.2. The along-track and cross-track errors obviously have the highest contribution to the 3-D orbit errors. However, due to the SLR-tracking geometry, only fractions of these components affect the SLR residuals.

The domination of the along-track errors is caused by the different strengths of the orbit model for the three orbit components. Uncertainties in the modeling of the atmospheric effects on the satellite, which mainly act in the tangential direction, require the estimation of a scaling factor for the atmospheric drag. As a result, the along-track direction is less constrained by the dynamical model compared to the cross-track and radial directions. It can furthermore be seen in Fig. 5.11 that the cross-track errors are

slightly increased between day 312 and day 314. A conclusive explanation for the cause of this effect could not be found, however.

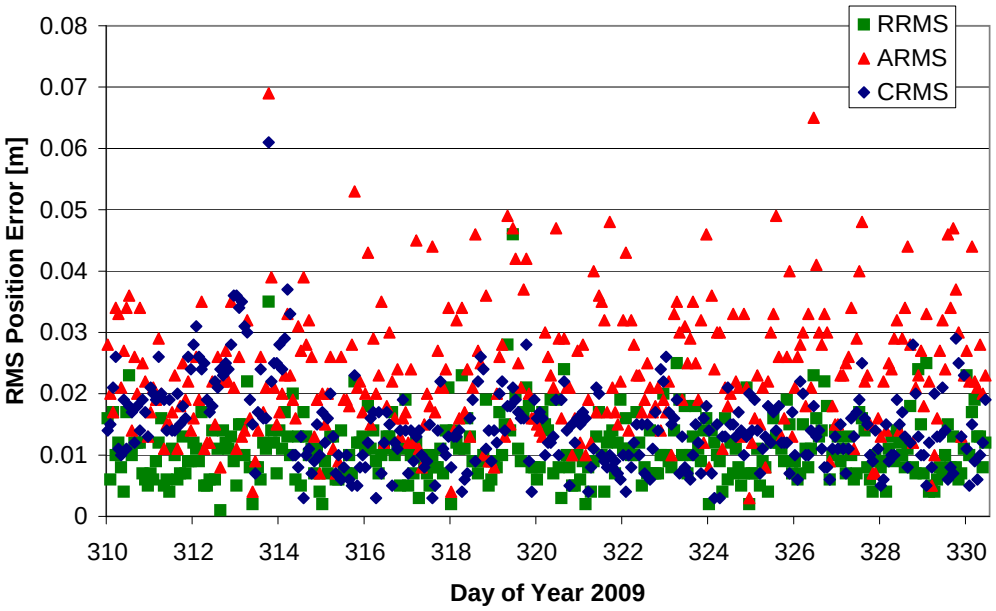

Fig. 5.11: Along-track (red), cross-track (blue) and radial (green) orbit errors for RETICLE-based TerraSAR-X orbits with respect to the reference orbit.

The previous analysis has shown that the near real-time orbits with the RETICLE products enable a rapid orbit reconstruction with high accuracy. The 3D orbit errors are well below 10 cm. The radial component has the smallest error. It is unbiased and stays at approximately 1-2 cm. This error budget is beneficial for altimetry applications in particular, since the radial orbit error directly affects the radar measurement. The near real-time POD requirement for the radial orbit error for radar missions was to be better than 10 cm (see Sec. 1.2). The analysis has shown that the RETICLE-products allow an orbit determination performance five to ten times better than the requirement!

The occultation missions have a similar positioning requirement, but more importantly a stringent requirement on the velocity-error of the LEO-spacecraft. For this mission type, the along-track velocity error is demanded to be less than 0.1 mm/s. The compliance of the requested positioning accuracy has already been demonstrated. In order to assess if the latter requirement can be fulfilled as well, the 3D RMS velocity error of the TerraSAR-X satellite has been computed and plotted in Fig. 5.12. It can be seen that the velocity error varies between 0.01 mm/s and 0.06 mm/s most of the time. Only four POD runs exhibit larger 3-D velocity errors between 0.07 mm/s and 0.09 mm/s. These instances correlate with increased position errors for the corresponding orbit determinations depicted in Fig. 5.11. Obviously, the velocity requirement can be fulfilled for the entire test period. It should furthermore be noted, that the plot shows the 3-D velocity error and the error component in the along-track direction is thus even smaller.

The analysis presented in this section demonstrated the performance of the RETICLE products for a reduced dynamic orbit determination. It could be shown, that the

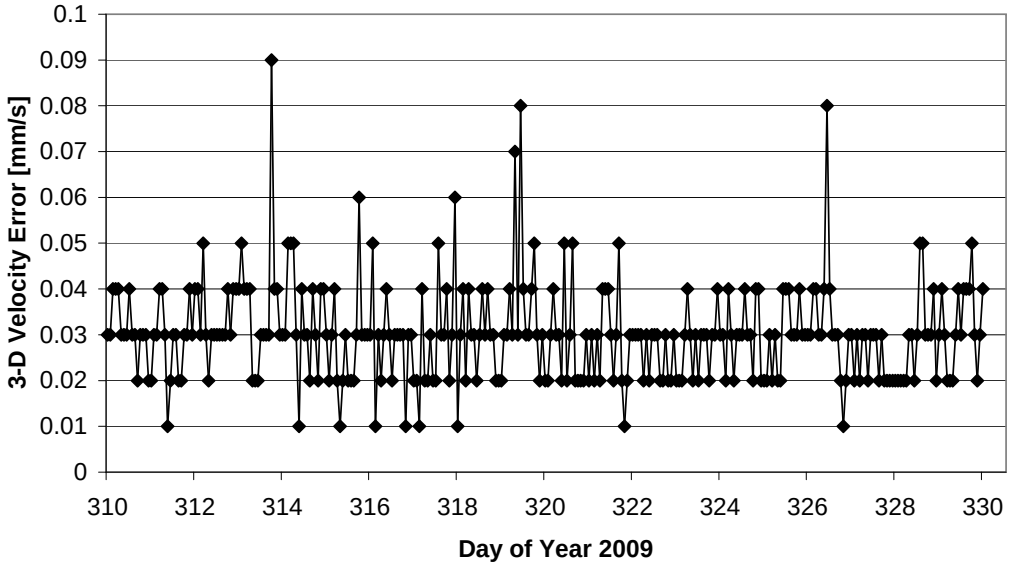

Fig. 5.12: 3D velocity error of near real-time TerraSAR-X orbits computed with RETICLE products.

accuracy requirements for near real-time precise orbit deterimation, which currently exist for radar altimetry and occulatation missions, can be fulfilled with a signifcant margin. This margin makes the POD procedure robust against potential degradations of the real-time clock estimation, which might be caused by an outage of stations in areas with low redundancy, for example.

5.3.2 Kinematic Point Positioning

In the previous section, the orbit determination performance with a reduced dynamic model has been demonstrated. The model helps to reduce positioning errors caused by corrupt measurements and also from errors in the GPS satellites' ephemerides. As a complementary analysis, a kinematic orbit determination "KIPP" has also been performed. The positioning results are expected to be more sensitive to measurement errors as well as clock errors in the clock products. The POD process has again been set up with 12 hour data-arcs and the start epoch was incremented in steps of 90 minutes. It should be noted, however, that the kinematic POD is not sensitive to the data arc-length, since no dynamic parameters for the orbit propagation are estimated. Similar to the previous analysis, the final 90 minutes of the kinematic trajectory have been compared to the same reference solution, which originates from a reduced dynamics POD with CODE final products.

The results for the 3D RMS position errors of the RETICLE-based TerraSAR-X orbit are depicted in Fig. 5.13. The figure reveals that a significant change in the quality of the orbit determination happens on day 320 in the middle of the test period. Prior to that date, the orbit errors are on the order of 10 cm with a few outliers exceeding 20 cm. After day 320, the position errors increase significantly with the maximum error being as large as 1.65 m. The variation of the position error between consecutive POD runs is also much higher compared to the first half of the test period. A degraded orbit determi-

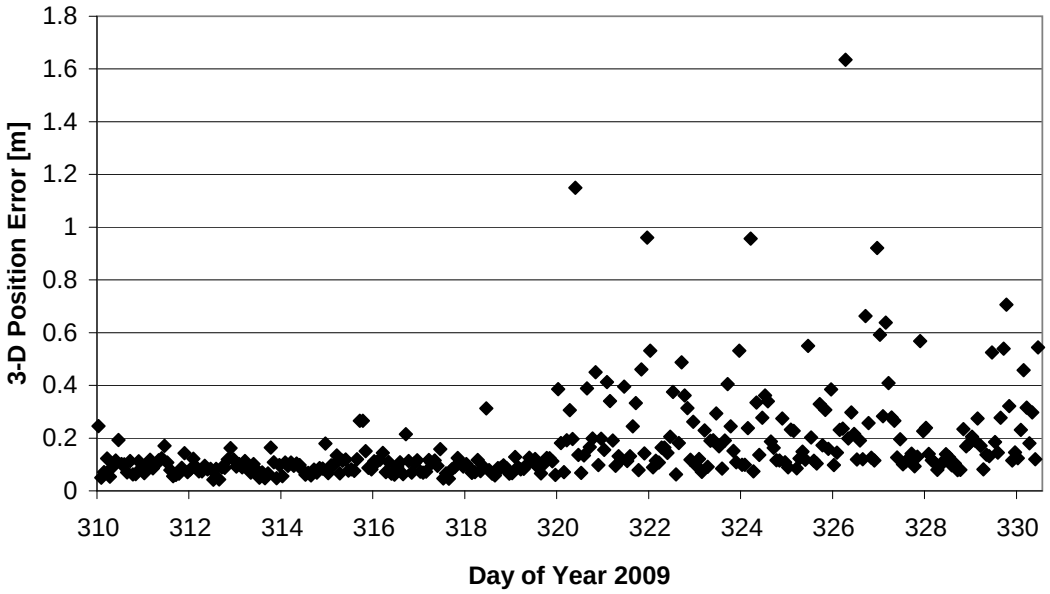

Fig. 5.13: Position errors of near-real-time kinematic TerraSAR-X orbits with RETICLE products. The final 90-minutes are compared to the reference solution.

nation performance has been anticipated, since contrary to the reduced-dynamics filter, the kinematic POD cannot benefit from a dynamical model, which helps to suppress the impact of outlying measurements. However, this strong degradation is still unexpected and has not been notable in the previous analysis. As already mentioned, the kinematic POD is more sensitive to degradations of the measurements and the orbit- and clock-product. Thus, the increased positioning errors are most likely explained from a degradation of the observations or the RETICLE-product. A reduced quality of the latter should manifest itself in the Signal-In-Space Range Error which is depicted in Fig. 5.1. The SISRE should be increased after day 320, which is obviously not the case. Therefore, the degradation must be related to the observations. It turns out that occultation measurements have been reactiveted for the IGOR receiver starting on day 320 (M. Wermuth and O. Montenbruck, private communications). As a result, the number of observed satellites per day drops from approximately 9 to 8.2 as depicted in Fig. 5.14. With fewer satellites available on average at each epoch, the effect of measurement errors on the positioning solution is higher. Due to the absence of a dynamical model, which helps to suppress the effect of measurement outliers in the dynamic filter, this effect is much more pronounced for the kinematic POD.

Finally, the individual orbit error components shall be regarded. Fig. 5.15 depicts the radial, cross-track and along-track errors of the RETICLE-based kinematic orbits. Until day 320, all three error components stay below 10 cm most of the time. The radial-component exhibits several outliers, which exceed up to 30 cm. After the activation of the occultation measurements on day 320, the along-track and cross-track errors are significantly larger, but in general still less than 30 cm. The radial-component, whose errors can amount to 90 cm, is obviously the main contributor to the position error. Contrary to the reduced-dynamic orbit determination, the radial orbit error dominates the error budget. This result could be expected, since the same behavior can also be found

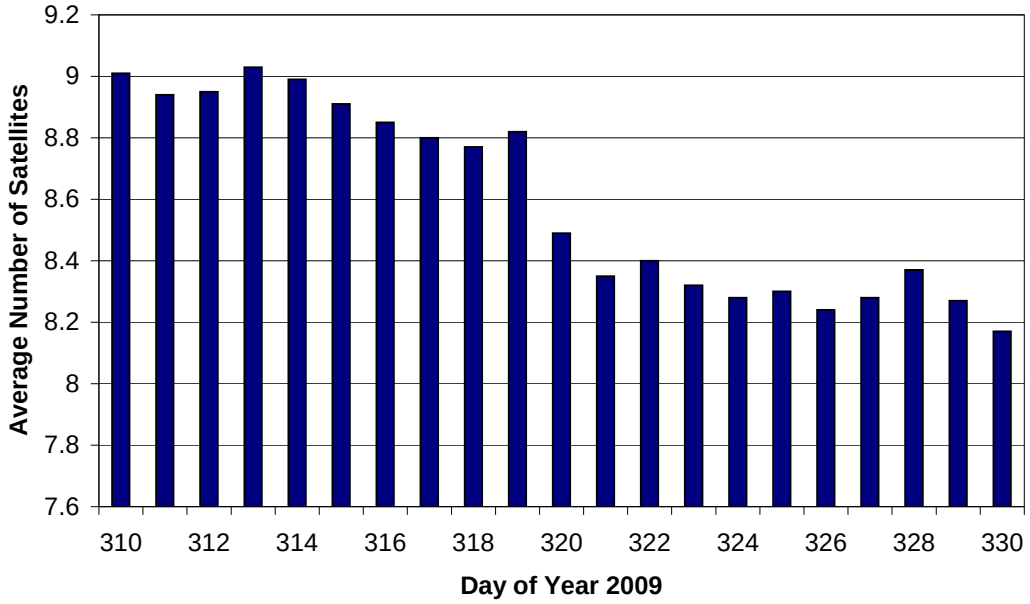

Fig. 5.14: Average number of satellites observed per day by the IGOR receiver on TerraSAR-X. The drop after day 320 is related to a reactivation of occultation measurements.

for kinematic positioning results on the ground. Since the satellites used for positioning are exclusively in the upper hemisphere, the vertical dilution of precision (DOP) is larger than the horizontal DOP. As a result, the standard deviation of the up-direction (or radial direction) is larger compared to the horizontal plane (which corresponds to the along-track and cross-track orbit errors) [Misra and Enge, 2001].

5.3.3 Kalman Filter based Real-Time Navigation

The previous sections have demonstrated the performance of the RETICLE products for near real-time POD of LEO satellites. The results have been achieved by processing batches of observations every 90 minutes, which corresponds to the approximate orbit period of a typical LEO mission. With a downlink station at high latitude, the measurements from the on-board GPS receiver can be downloaded only once per orbit. Therefore, the latency of the observations is currently the limiting factor in the orbit determination. The low latency of the GPS orbits and clocks from RETICLE would allow a process much closer to real-time. It would furthermore be a simple task to implement a prediction of the most recent estimated orbit and clock for the realization of true real-time positioning.

To overcome the limitation caused by the latency of the observations from LEO satellites, two different scenarios shall be discussed here. The first approach is the installation of additional downlink stations to ensure more frequent contacts to the satellite or even a global coverage. Obviously, the cost and effort for the installation, operation and maintenance of such a global downlink station network must be justified by the benefits of a quick access to the satellite data. The requirements for the current scientific mission can, however, be fullfilled with a near-real-time POD and therefore no significant push towards building a global downlink coverage exists. This situation may change in the

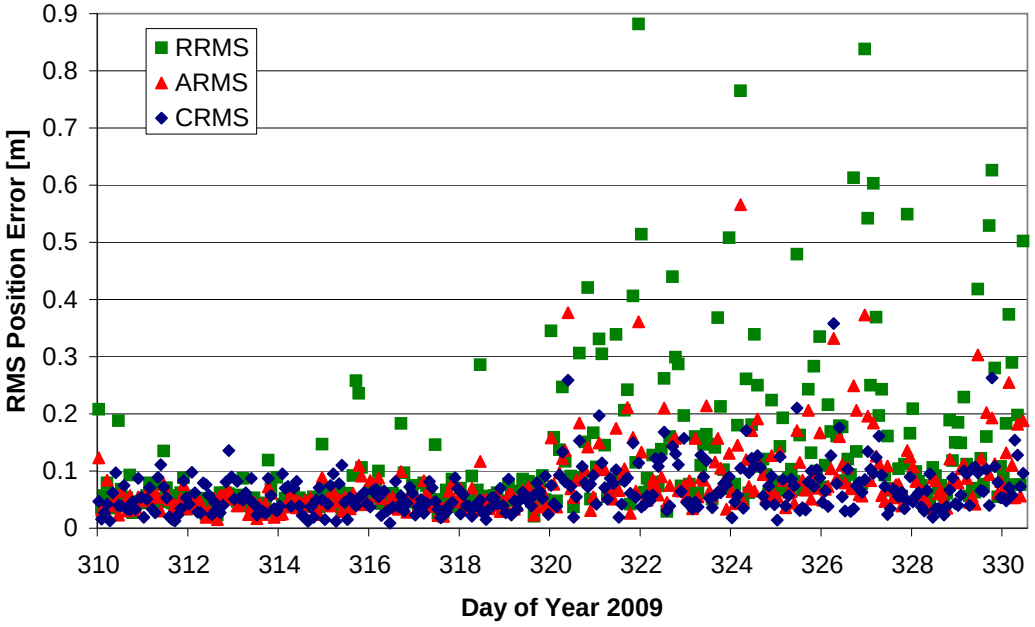

Fig. 5.15: Radial, along-track and cross track position errors of near-real-time kinematic TerraSAR-X orbits with RETICLE products. The final 90-minutes are compared to the reference solution.

future, however, when disaster monitoring or real-time weather prediction gain a higher importance. A second issue in establishing a global station network is simply due to the geographical or geo-political situation. The installation of downlink stations requires a fundamental infrastructure to be available at the prospective sites. Inappropriate features of the landscape or political instabilities may prevent the buildup of stations in otherwise desirable areas. Therefore, a global downlink capability is certainly unrealistic in the near future.

The second option for a real-time process basically inverts the data-access problem. Instead of downloading the GPS measurements to the ground and performing the POD there, the RETICLE products could as well be uploaded to the satellite, which could process the data in an on-board navigation system. Fig. 5.16 depicts such a scenario, which makes use of several geostationary relay satellites. An up-link station with permanent visibility to a single GEO-satellite uploads the product, which is then re-broadcasted and disseminated among the relay-satellites. The LEO satellite receives the re-broadcast of the relay satellites and uses the GPS orbits and clocks in its on-board navigation system for a precise orbit determination. NASA has proven the feasibility of this concept with the Global Differential GPS system, which offers their real-time orbit and clock corrections for space users via the Tracking and Data Relay Satellite System (TDRSS) [Bar-Sever et al., 2004].

After having introduced two possible options for true real-time navigation scenarios for LEO satellites, the performance of the RETICLE products shall be demonstrated. For the analysis TerraSAR-X data from November 6th until November 16th, 2009, has been selected. Though the data has been post-processed, the navigation algorithm used for the tests is real-time capable, which means that measurements are only processed in forward mode and data editing is exclusively performed using current and past data.

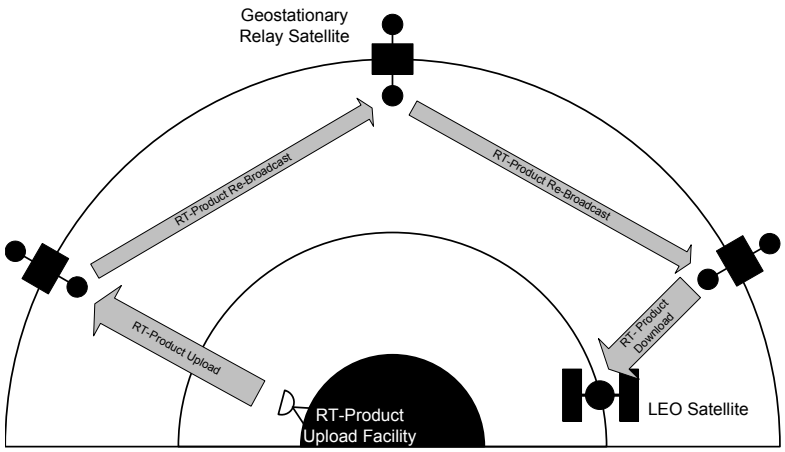

Fig. 5.16: Real-time dissemination of clock-products in space. The data is uploaded to a geostationary relay satellite constellation. The product is re-broadcasted and received by a LEO satellite without direct visibility to the upload station [Bar-Sever et al., 2004].

The employed algorithm is based on a Kalman filter, which is used as a real-time onboard navigation system for LEO satellites. It will be referred to as real-time navigation algorithm (RTNAV) in this section. Contrary to the reduced dynamic or kinematic POD, this algorithm uses an efficient formulation of the satellite's equations of motion in the Earth-fixed coordinate frame. The force model includes third-body perturbations of the Sun and the Moon, a Harris-Priester model for the atmospheric drag, solar radiation pressure and empirical acceleration in radial, tangential and normal directions, which account for the simplifications of the force models. The state vector comprises the satellite's position and velocity, scaling factors for the radiation pressue and drag coefficient, the empirical accelerations, the receiver clock offset and the carrier-phase ambiguities of all tracked GPS satellites. A detailed description is provided by Montenbruck and Ramos-Bosch [2008]. For this analysis, the ionosphere-free combinations of the L1 and L2 measurements of TerraSAR-X's IGOR receiver have been processed.

In order to set the benchmark for the RETICLE products in this analysis, the RTNAV-software has first been used with CODE final orbit- and clock products. The three plots in Fig. 5.17 depict the radial, along-track and cross-track errors of the satellite's orbit. The errors are computed with respect to the reference solution, which are the concatenated middle parts of the reduced-dynamics POD using CODE final products. The plot shows that the orbit errors over the entire ten days exhibit a constant offset of -5 cm, +5 cm and +4 cm in the radial, along-track and cross-track directions, respectively. The standard deviation of the errors is 5 cm for the radial and along-track components and 4 cm for the radial component. The overall 3-D RMS error is 11.9 cm.

A reduced performance of the real-time algorithm with respect to the reference solution, which has been obtained from a batch least-squares estimation, could of course be expected. The RTNAV-software processes the data in forward-mode only. Therefore the positioning results are affected by a larger noise compared to a smoothed solution obtained with forward/backwards-smoothing or a LSQ adjustment. Furthermore, ensuring real-time capabilities poses additional challenges for data editing. The editing limits

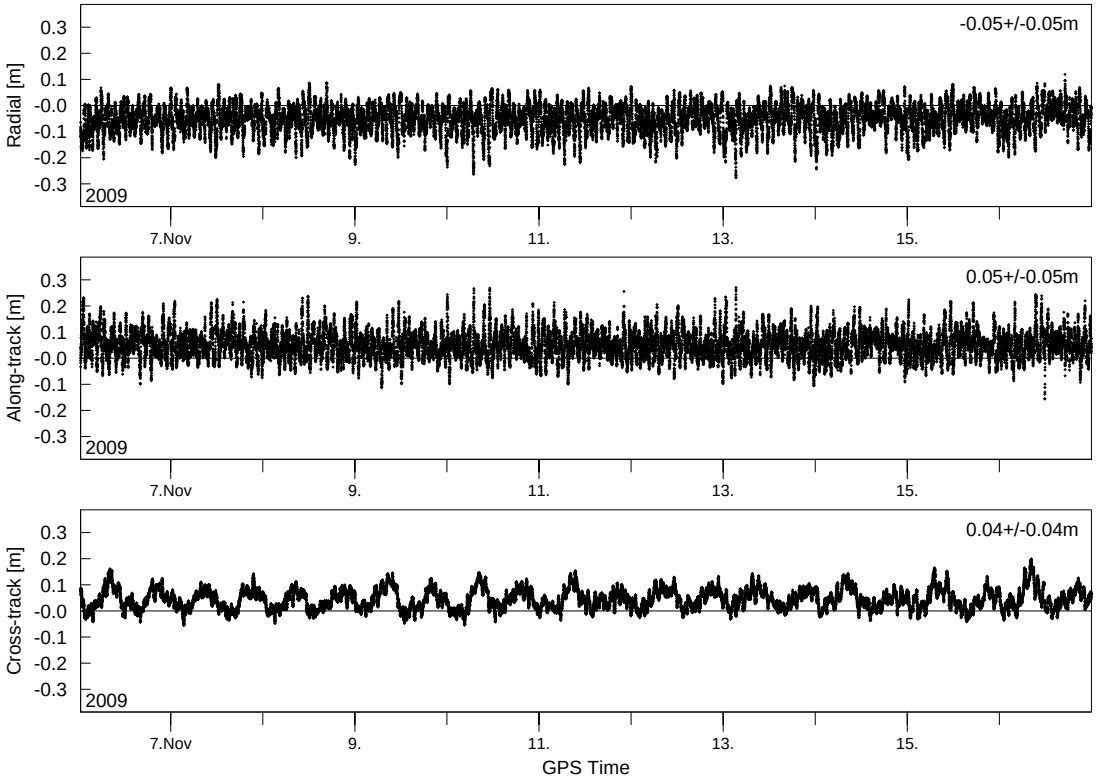

Fig. 5.17: Radial, along-track and cross track position errors of TerraSAR-X POD with real-time Kalman filter based on CODE products.

must be set tight enough to reject bad measurements, but at the same time a robust estimation must be ensured for periods with reduced satellite visibility.

As a side note, an additional feature of the RTNAV algorithm shall be mentioned. The TerraSAR-X satellite performed a maneuver on November 9th, 2009. The maneuver started at 09:41:47h UTC and lasted for 6.5 seconds, applying a delta-V in the tangential direction. Due to the maneuver handling implemented in the RTNAV algorithm, no degradation of the navigation performance is notable during this interval.

The three plots in Fig. 5.18 show the corresponding results for the RETICLE GPS orbits and clocks. Note that the scale of the axis of ordinates has changed. Except for the different GPS ephemerides no other changes have been applied to the POD process. It can be observed that the position biases for radial and along-track have increased compared to the previous analysis and are now at -5 cm and 5 cm, respectively. The mean of the cross-track error amounts to 3 cm. Interestingly, the sign of the biases is consistent in all cases. The standard deviations for the radial and along-track components have increased to 6 cm and the cross-track standard deviation is at 5 cm. The total 3D RMS error of 12.9 cm over the entire test period demonstrates only a slightly decreased performance compared to the CODE products.

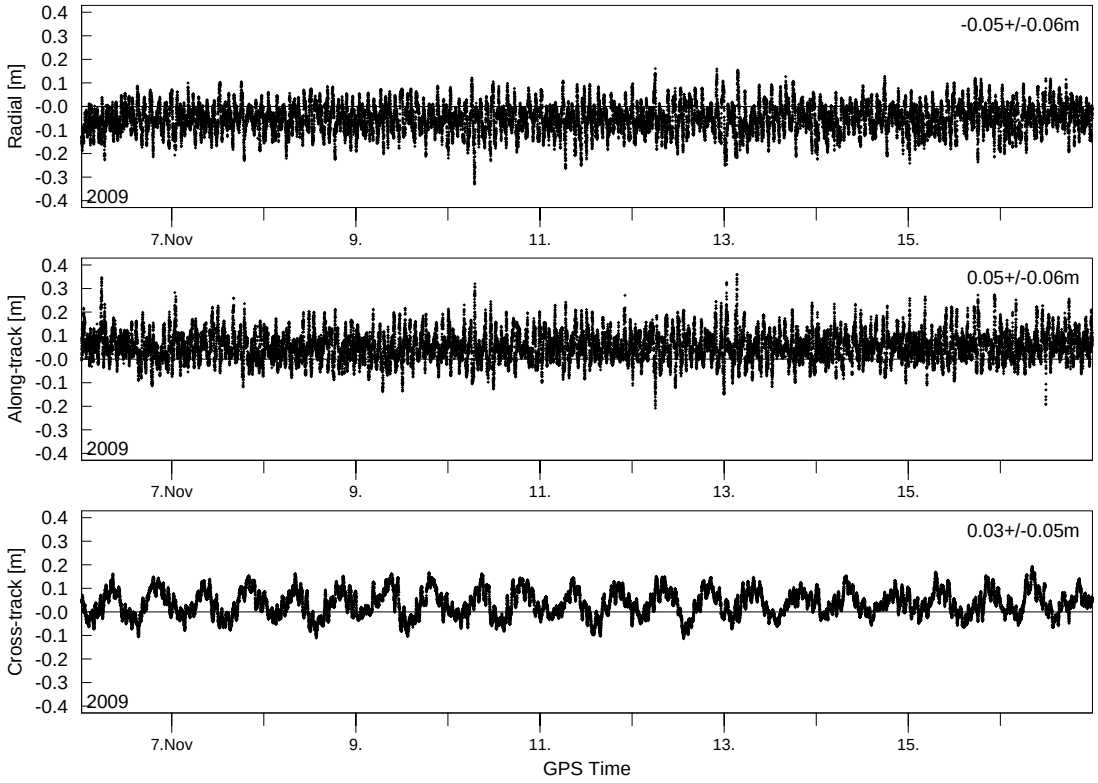

Fig. 5.18: Radial, along-track and cross track position errors of TerraSAR-X POD with real-time Kalman filter based on RETICLE products.

6. IGS Real-Time Pilot Project

6.1 Overview and Status

The Real-Time Pilot Project (RTPP) of the IGS has already briefly been introduced in Sec. 1. The project officially started in October 2007. One of its main objectives is the employment and maintenance of a global IGS real-time tracking network. Since the beginning of the project, the real-time network has been continuously extended by upgrading existing IGS reference stations with data transmission capabilities via NTRIP. Additionally, new stations, which are not part of the official IGS network, have been incorporated into the real-time network.

Besides the network extension, the investigation of data formats and technology for real-time GNSS-streams belongs to the tasks of the pilot project. Two different techniques coexist at the moment: One of them is the transmission via NTRIP, which has already been introduced in Chap. 3. The other technique is called UDPRelay, which is promoted by NRCan. Contrary to NTRIP, which uses TCP/IP connections, the UDPRelay technology uses UDP connections to transfer the data from the central distribution point at NRCan to authorized users. Another difference between NTRIP and UDPRelay is the access to the individual data streams. Whereas NTRIP requires a dedicated stream for each station, UDPRelay offers all stations in a single stream. Dedicated software at the user's end splits the data from the single stream into the contribution of each individual station. This coexistence of two different formats for real-time data transfer posed the problem, that one part of the network was available exclusively via NTRIP, while the other part could only be accessed with UDPRelay. As a result, analysis centers and users could not exploit the complete network, since they are confined to one of the two techniques. However, over the last two years, effort has been made to harmonize the network and make the majority of the stations available in both formats. Currently, more than 120 stations are available at BKG's caster www.igs-ip.net via NTRIP [BKG, 2009] and approximately 80 stations can be received via UDPRelay from NRCan [IGS Real Time Pilot Project, 2009]. Besides the streaming techniques, current and future data formats for transmitting GNSS measurement are discussed in the RTPP as well. The goal is to ensure that the needs of the IGS community are fulfilled. The main requirements are to maintain a sufficient resolution of the measurements for pseudorange and carrier-phase measurements, but at the same time realize a significant compression of the data stream. Equally important is the ability to transmit all signals of the current and future GNSS constellations, which is a limitation of many current data formats. Finally, standardized messages must be defined to disseminate corrections in real-time. As a result of these activities, the IGS became a member of the GNSS standardization

organization RTCM, in order to promote these needs and influence decisions for future formats.

One of the most important tasks of the real-time pilot project is of course the generation, monitoring and dissemination of real-time products. The fundamental product to start with is precise real-time orbit and clock information. Since September 2008, four real-time analysis centers participate in the generation of real-time orbits and clocks, namely, BKG, DLR/GSOC, ESA/ESOC and NRCan. These four analysis centers submit a daily file to ESOC, which serves as the analysis center coordinator. In the future, more analysis centers plan to join this activity. At ESOC, the different real-time products are compared to the IGS rapid orbits and clocks. Results from these comparisons will be presented in the following section. Since February 2008, the contributions of the individual analysis centers are combined into a combined solution and published as a clock-rinex file on the ESOC ftp-server [Dow et al., 2009]. This combined solution is currently generated as an offline product. However, an online combination of the individual products is planned to start in 2010. The combined product will be generated "on-the-fly" from the real-time data stream submitted by the individual analysis centers. The envisaged format for the combined solution are the new, recently proposed state-space-messages for the RTMC3 format [RTCM, 2009], which are already used by the RETICLE system as one option for disseminating the solution. The combined solution will contain precise orbit and clock corrections. The data stream with these corrections will be made publicly available on a caster.

Another activity of the RTPP is the production of global ionosphere maps (GIM) in real-time. The existing real-time network will be used to compute maps which show the ionospheric activity, expressed in TEC units, depending on the location on the globe. Having this information available with short latency is beneficial for topics like space weather surveillance and single-frequency PPP in real-time.

6.2 Real-Time Product Comparisons

As already mentioned, the production and monitoring of real-time products is one of the key objectives of the RTPP. The comparison and the combination of real-time products by ESA/ESOC is now ongoing for more than one year. The solutions of the individual ACs are compared to the orbits and the clocks of the IGS Rapid product and are therefore available with a latency of one day. Reports with the results of the comparison and a combined clock file in Rinex format are published on the IGS server and updated every day [Dow et al., 2009]. The plots in Fig. 6.1, Fig. 6.2 and Fig. 6.3, which show the results for each submitted real-time solution, have been compiled from these reports.

Fig. 6.1 shows the 3D RMS orbit errors over the period from September 2008 until March 2010. The RMS of the orbit errors is computed for each satellite individually for the entire day. Then the mean value of all available satellites is taken. This mean over the entire constellation of the daily RMS orbit errors is depicted in the plot. It should be noted that the orbits of the BKG and DLR products are based on the IGU predicted orbits. NRCan and ESOC on the other hand use independent GPS orbit information, which is produced from an offline batch process with a higher update rate and shorter latency than the Ultra rapid predictions. The orbit errors for the DLR contribution vary

between 20 mm and 80 mm. The errors exceed 80 mm in rare cases only. A variation of the orbit accuracy is expected, since the orbit estimation of the GNSS satellites cannot be performed with uniform accuracy over time. Due to the GPS constellation geometry, different satellites enter the so called "eclipse phase" at different times of the year. During eclipse season, a satellite's path crosses the Earth's shadow. The changing illumination leads to changes in the solar radiation pressure. The resulting changes in the acceleration of the satellite can in general be modeled, but numerical integrators are likely to suffer from the rapid changes in the force models, leading to a loss in accuracy. Additionally, the attitude modeling of the satellites is more challenging during this period. Therefore, the orbit accuracy of satellites being in the eclipse season is more likely to be degraded. Furthermore, the tracking coverage in the IGS network for unhealthy satellites is often reduced, since some receivers are configured to omit them. As a result, data arcs for a satellite, which has been set unhealthy for a certain fraction of this period, have in general fewer observations for this particular spacecraft leading to a reduced performance of the orbit determination.

Except for a short period in April 2009, the orbit errors of DLR and BKG show a comparable magnitude. This result should be expected since the same orbit product is used. Small differences in the orbit errors are still present and result most likely from differences in how and when orbit updates in the filter algorithms are performed. The other two analysis centers produce their own independent orbit solutions and are thus not bound to the 3h-latency and 6h update rate of the IGU product. The 3D orbit errors of ESOC are very consistently at a level of 6 cm and show only very little variation compared to the other solutions. The orbit errors of NRCan are in general between 20 mm and 60 mm. Though an improvement over the IGU predictions is notable at least for the orbits from NRCan, the effort to set up a production of independent GPS orbit products certainly exceeds the benefits for the clock estimation process. ESOC and NRCan, being IGS analysis centers which also contribute to the Ultra Rapid product, have the complete GPS orbit determination processing chain already set up. Besides being able to avoid the latency of the IGU product by directly using their contribution, ESOC and NRCan can also produce orbit updates at a shorter interval than currently realized for the IGU.

The plots in Fig. 6.2 and Fig. 6.3 show the results of the clock comparisons in terms of an RMS error and a standard deviation (σ), which are averaged over the individual RMS or standard deviation, respectively, of each satellite of the complete constellation. Prior to the computation of the clock errors, a mean constellation clock offset is removed at each epoch. Furthermore, the effect of the radial component of the orbit error is removed as well for the computation of the clock errors. The RMS clock error can be understood as a total clock error containing the mean clock offset and the short term variation. The standard deviation, on the other hand, characterizes the variation of the clock error and is not affected by the mean offset. The goal of the real-time pilot project is to achieve better than 0.3 ns in both RMS and the standard deviation of the daily clock-errors with respect to the IGS Rapid product.

The development of the clock errors over time reveals interesting insights into the evolution of DLR's RETICLE filter. At the beginning of the real-time pilot project, only ESOC, DLR and NRCan where submitting comparable solutions. BKG submitted

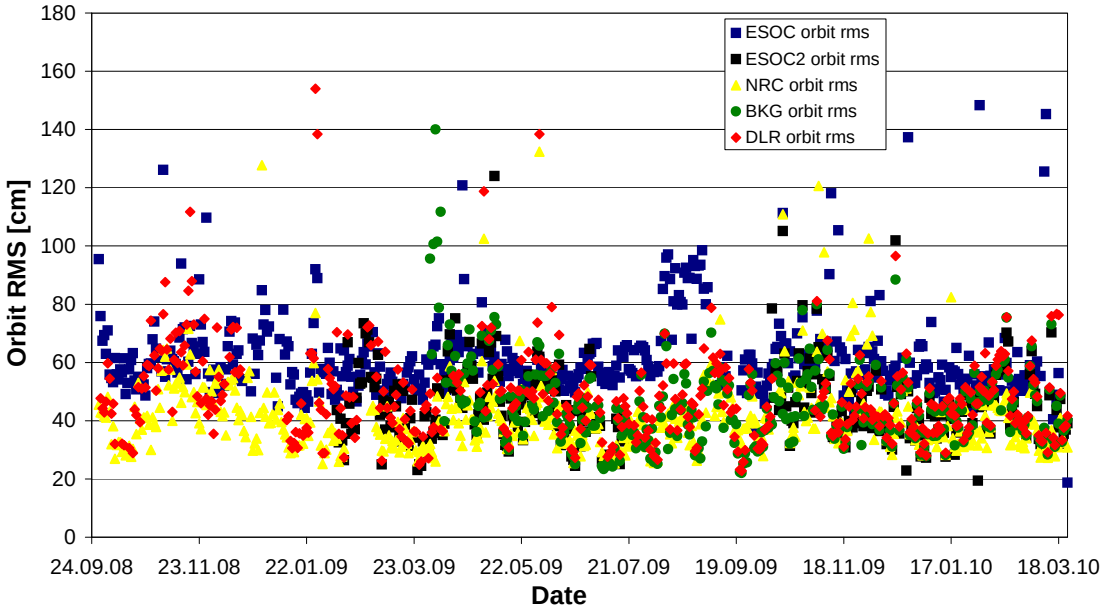

Fig. 6.1: Orbit error comparison from the IGS real-time pilot project based on Dow et al. [2009]. The plot shows the 3D RMS orbit errors of the real-time orbits compared to the IGS Ultra-Rapid orbits.

a solution as well, however, the clocks were based on time-differences of observations and thus not comparable to the absolute clocks of the other analysis centers. It becomes obvious that the RMS errors of all three analysis centers at the beginning of the project were at approximately 0.4 nanoseconds. The NRCan solution showed significant variations in the RMS value. This product was derived from the data of the UDPRelay real-time network, which consisted of only about 30 stations at that time. Therefore, the reduced depth of coverage made the solution sensitive to tracking errors and station outages. With the inclusion of more stations into the UDPRelay network since the end of March 2009, the solution of NRCan significantly improved. The large variations in the RMS errors vanished and the solution stabilized first at about 0.3 ns and later at 0.2 ns with some exceptions. Also, at the end of March 2009, BKG switched from submitting relative clocks to absolute clocks and the solution became directly comparable to the other three analysis centers. The RMS errors of this solution, however, shows the largest variations of all submitted solutions. The two solutions submitted by ESOC exhibit RMS errors of less than 0.3 ns with only very few exceptions.

The RMS of the RETICLE solution started at a comparable level with the other ACs. Continuous efforts were made to improve the system. To increase the availability of the internet connection and allow a more stable platform for a continuous filter operation, the system was moved from an office PC to a dedicated server beginning in May 2009. At the same time, a notable increase in the RMS of the RETICLE solution appeared in the solution. Two reasons could be identified, which have caused this effect. Firstly, more and more receivers in the real-time tracking network have been equipped with receivers, which report the L2C (or C2) observations in favor of P2. This undesirable situation is in general uncritical as long as L2C observations are correctly identified. In this case, the L2C observations are omitted for the sake of consistent

processing. However, problems occur as soon as they are erroneously declared as P2 observations. In this case, the receiver- and satellite-dependent P2C2-biases cause a difference between the modeled and the real measurements and lead to inconsistencies in the processing. Incorrect flagging of C2 observations could be identified for some stations and was caused by an incompatibility between a server software of a GNSS receiver and an NTRIP-caster implementation (see also Chap. 3). The receiver reported the measurements correctly as C2 in a proprietary format, however, the NTRIP caster re-broadcasted them as P2. After the exclusion of these stations from the filter in June 2009, the RMS values of the RETICLE product were significantly reduced. At approximately the same time, the input data rate of the RETICLE system was increased from 30 seconds to 10 seconds. However, shortly afterwards, the RMS errors started to raise again to approximately the same order of magnitude as before. In most cases, the RMS was held high by one or two satellites of the constellation, which exhibited slowly growing biases in the estimated real-time clocks. A closer look revealed a correlation between the orbit accuracy of the affected spacecraft and these biases in the clock values. This effect, which led to a growing bias in the estimated clock, has already been discussed in Sec. 4.5. With the beginning of November 2009, this problem has been fixed in the operational implementation of the RETICLE system with the inclusion of process noise on the carrier-phase ambiguities. It is obvious from the statistics in Fig. 6.2, that the RMS errors stabilized at approximately 0.25 ns.

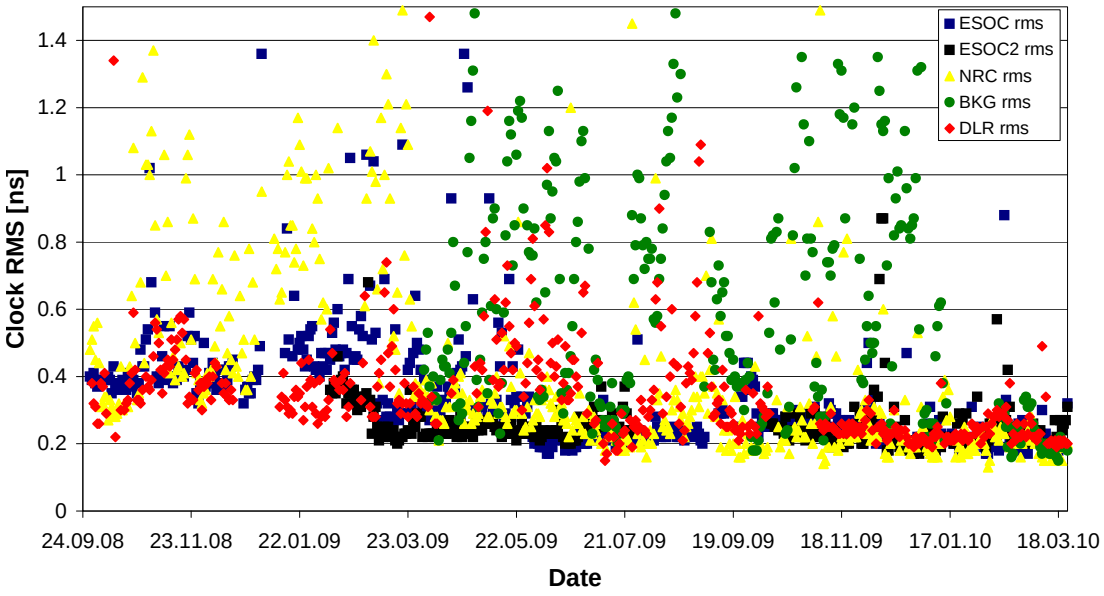

Fig. 6.2: Clock error comparison (RMS) from the IGS real-time pilot project based on Dow et al. [2009]. The plot shows the RMS clock errors of the real-time clocks compared to the IGS Ultra-Rapid clocks.

Fig. 6.3 show plots of the standard deviation of the clock errors for all analysis centers. The RETICLE clocks have a standard deviation between 0.15 ns and 0.25 ns, though several outliers are present. These outliers were often caused by interruptions of the internet connection and resulted in a re-initialization of the clock estimation in the Kalman filter. The necessary convergence time of the filter during which the clock

estimates have not reached their final accuracy manifests itself in increased RMS and standard deviations. As already mentioned, this was one of the main issues, which motivated the transition of the system to a dedicated server. After this transition in May 2009, the standard deviation for the DLR clock stayed below 0.2 ns most of the time and often reached 0.1 ns. The standard deviations of the estimated clocks of NRCan showed high variations similar to the RMS until the network was expanded in March 2009. Afterwards this value was improved first to the 0.2 ns level and then even further down to 0.1 ns and less. The solutions submitted by ESOC show a reliable day to day repeatability in the standard deviation. The first solution is at about 0.2 ns since April 2009. The second solution has reached an even better level of about 0.15 ns. The BKG solution, however, often has the lowest standard deviation of all clock products, achieving quite frequently levels of less than 0.1 ns. Since November 2009, the DLR clock solution has stabilized at a standard deviation of about 0.15 ns, which is slightly higher compared to the performace achieved in July of the same year. The difference is caused by the aforementioned inclusion of process noise on the carrier-phase ambiguities to avoid the effect of the along-track orbit errors on the clock estimation. Naturally, this process noise reduces the weight of the carrier-phase observations. However, this sacrifice seems justified regarding the improvement in the clock RMS. It is also interesting to note that during the phases when the RETICLE solution was affected by biases, which led to a high RMS value, the standard deviation is hardly affected.

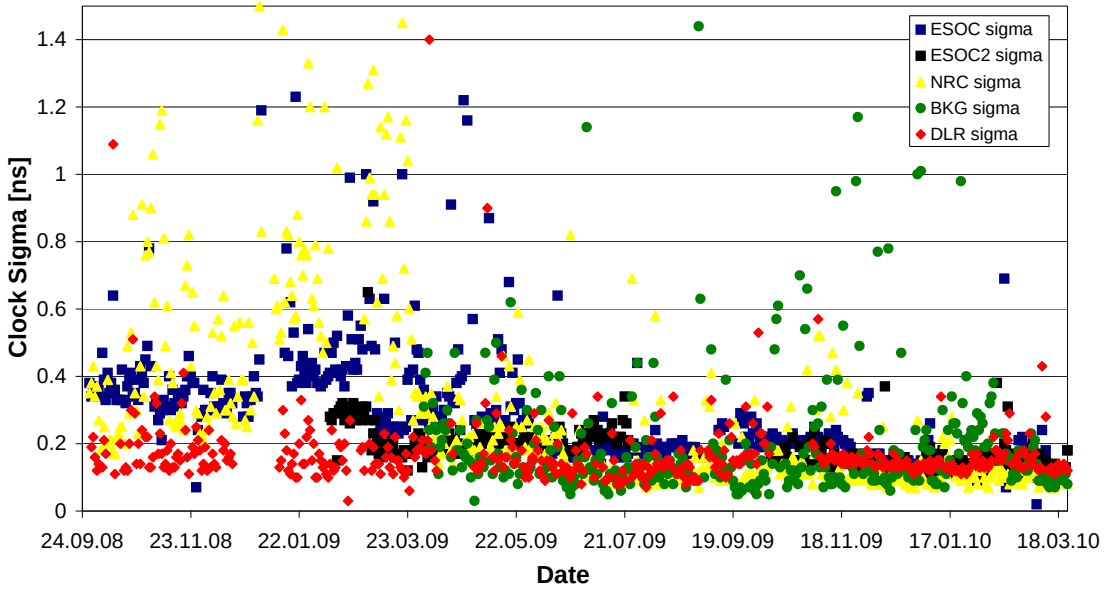

Fig. 6.3: Clock error comparison (sigma) from the IGS real-time pilot project based on Dow et al. [2009]. The plot shows the standard deviation clock errors of the real-time clocks compared to the IGS Ultra-Rapid clocks.

In summary it can be stated that the RETICLE system is highly competitive to other implementations of real-time clock estimation systems. Both the standard deviation and the RMS error stay well below the accuracy level defined by the IGS real-time pilot project. After the inclusion of process noise, the RMS value meets this target as well. As long as the quality of the orbit used for the clock estimation cannot be improved

beyond what is currently realized in the IGU predictions, this concept appears to be the most effective way to ensure a robust and precise clock estimation.

For the conclusion of this section, the results for the combined clock product shall be presented in Fig. 6.4. Though currently being produced as a post-processed product, the future real-time combination is expected to show the same level of performance. The plot shows the RMS and standard deviation of the combined real-time clock with respect to the Ultra Rapid clock from IGS. It turns out that the product has met its requirement of being better than 0.3 ns quickly after its launch in February 2008. At that time, all input products had reached a sufficient level of accuracy. Currently, the standard deviation varies between 0.1 ns and 0.2 ns. The RMS value is at the 0.2 ns level most of the time.

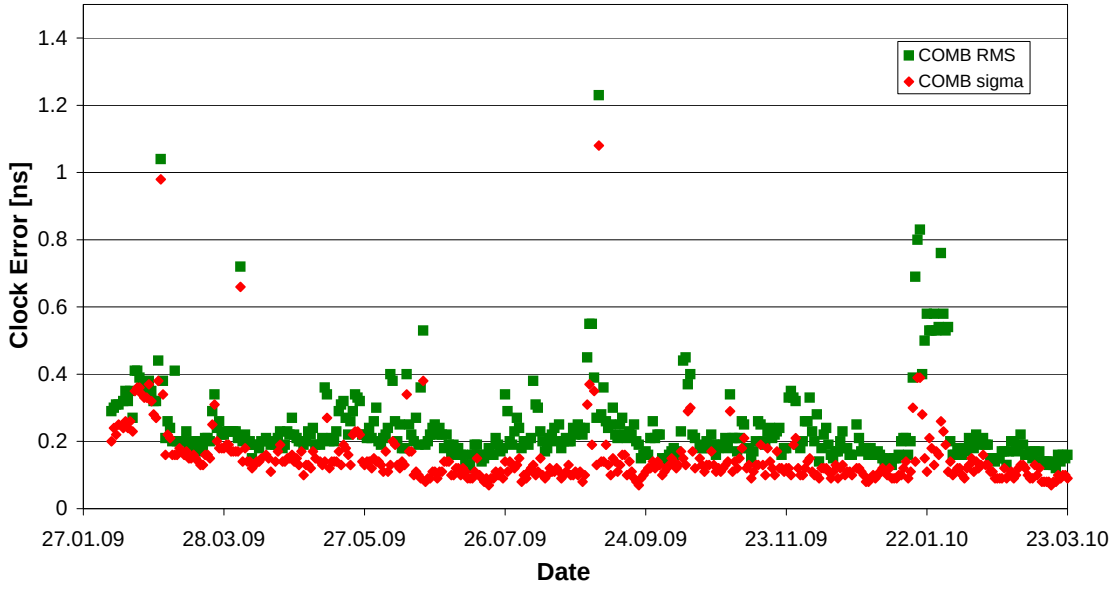

Fig. 6.4: RMS and standard deviation of the combined real-time clock product based on Dow et al. [2009]. The plot shows the comparison with the IGS Ultra-Rapid clocks.

Due to the low number of combined solutions, the combination is still sensitive to degraded accuracies and outliers in the input products. Especially if an individual solution is degraded due to a data-preprocessing problem, an undetected clock jump or due to disruptions in the internet connection, the combined product will be degraded as well. These effects are visible in Fig. 6.4 at several instances. Even though an outlier detection has been implemented to prevent these effects, more independent products are obviously required to further improve its robustness. Therefore, users of the combination should be aware, that the accuracy of the combination may change significantly.

Another not yet fully resolved issue is the orbit product to be used with the real-time clocks. Since the input orbits for the different products showed more or less pronounced differences as seen in Fig. 6.1, care must be taken when the combined clock is again merged with a trajectory. Whereas the orbits and clocks are guaranteed to be consistent for the products of the individual analysis centers, this may no longer be true after the recombination. An obvious advantage of the combined solution is the higher robustness towards outages of individual solutions. If an individual solution should be temporarily

unavailable due to a system crash or maintenance, the combination can still be made from the remaining solutions. On the user side, no dedicated switching to a backup real-time product would be required in this case. However, the combination does not offer protection against a caster-outage, which is currently a single-point-failure in the entire system. Currently, only very few casters exist, which are supplied with data by the real-time network. Ususally, the input streams are forwarded to other casters and a single caster is the central pick-up point for the majority of the streams. This dependency makes the real-time products sensitive to failures of this caster. Feasible redundancy concepts, which involve redundant data streams from the reference stations to back-up casters, are currently under discussion. Practical experience with the future real-time combination will show, whether the use of the combined solution or of individual solutions yields better results for different applications with different requirements in terms of availability and accuracy of the real-time orbit and clock product.

7. GIOVE Real-Time Clock Estimation

The previous chapters have demonstrated the real-time clock estimation capabilities of the RETICLE-system for the GPS constellation and the positioning results which can be obtained with the derived clock products. In the near future, several additional GNSSs will become operational. Besides the Russion GLONASS system, which currently undergoes a revival after the dramatic decrease in the number of active satellites after the break-up of the Soviet Union, the European Space Agency (ESA) has been appointed by the EU to manage the development and employment of a navigation system. The Galileo system will consist of 27 active navigation satellites plus 3 spare satellites, distributed in three orbital planes with an inclination of 56°. The orbit altitude of 23222 km will be higher compared to GPS and results in 1.7 revolutions per day. The Galileo system is planned to be interoperable with GPS and GLONASS, which means that two key prerequisites are fulfilled: Firstly, a degradation of the individual GNSS performance by mutual signal interference has been avoided through a sophisticated design of the navigation signals and, secondly, that multi-constellation receivers will be able to use the satellites of all three systems together for positioning. The Galileo system will transmit signals on three different frequencies, namely those in the E1[1]-, E5- and E6-bands.

The two Galileo test satellites, GIOVE-A and GIOVE-B, have already been introduced in Sec. 2.4. With the measurements obtained from the CONGO-network (see Sec. 3.3) it is possible to derive independent orbit and clock products for these satellites. Since all CONGO tracking stations are set up as real-time stations, the extension of RETICLE stands to reason to also produce real-time clock offset estimates for the GIOVE satellites based on orbit predictions. In this chapter, details about the GIOVE data processing strategy are presented, followed by an analysis section covering the use of the combined GPS/GIOVE real-time orbit and clock product for positioning applications. Beforehand, the data flow for the GIOVE processing chain shall be presented, which is depicted in Fig. 7.1. All CONGO stations transmit the raw measurements via NTRIP to a dedicated caster, which has been set up by BKG. The streams are accessed by the Institute of Astronomical and Physical Geodesy (Institut für Astronomische und Physikalische Geodäsie, IAPG) from Technical University Munich (Technische Universität München, TUM) and recorded to generate daily Rinex files. These data files are then used to generate GIOVE orbit and clock products in post-processing from a data arc of five days up to the most recent available day. A modified version of the Bernese GPS Software 5.0 [Dach et al., 2007] is used to determine GIOVE orbit and clock solutions using the GPS Rapid orbit and clock product [Montenbruck et al., 2009b]. The middle day of the five day solution is then saved as a precise orbit and clock solution.

[1] It should be noted that the Galileo frequency, which corresponds to L1, is generally denoted E1-L1-E2. For brevity, however, this frequency band is simply referred to here as E1.

This solution will be referred to as the final GIOVE product from now on. In order to provide orbits for the real-time clock estimation, the five day orbit solution is propagated for 48 hours. These predicted GIOVE orbits are stored on an ftp-server and downloaded by the RETICLE system. The latency of the orbit solution depends on the latency of the CODE Rapid products, which is ususally between 8-11 hours. Finally, as already mentioned in Sec. 4.2.6, an inter-system bias must be estimated for each CONGO-station. These biases are estimated as constant daily biases and provided as an input for the RETICLE system via an ftp-server. In the next section, the clock-estimation procedure for GIOVE is described and examples for the orbit and clock accuracy are provided.

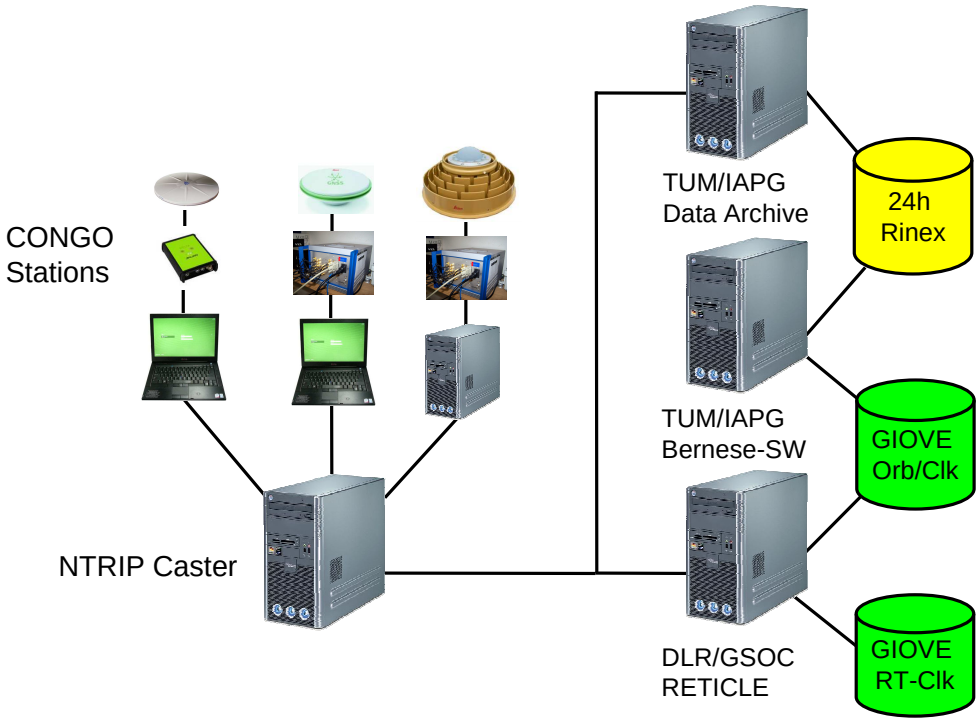

Fig. 7.1: Data flow diagram for GNSS processing of GIOVE observations from the CONGO network

7.1 Real-Time Clock Estimation Process for GIOVE

The real-time GIOVE clock estimation is based on the orbit predictions from IAPG. These predictions have a latency between 8-11 hours and are updated once a day. The orbit errors of the GIOVE-B satellite in radial-, along-track and cross-track components are depicted in Fig. 7.2. The final orbit from IAPG has been used as the reference. It becomes obvious that the radial and along-track components have comparably small errors with mean of 7 cm and 6 cm and a standard deviation of 4 cm and 5 cm, respectively. The along-track component on the other hand has a significantly larger error with -59 cm mean and a standard deviation of 23 cm. It becomes obvious that the along-track errors grow constantly over time until an updated orbit prediction is available, which happens at approximately 9:00h in this example. The orbit prediction of GIOVE-A has a similar performance with mean and standard deviations of -1 cm$\pm$7 cm, -73 cm$\pm$67 cm

and -7 cm±19 cm in radial, along-track and cross-track directions, respectively. It becomes obvious, that the orbit prediction accuracy is about a factor of ten worse compared to the IGU products for GPS. However, one has to bear in mind that the GIOVE orbits are computed from a network of only ten stations, compared to the orbit product for GPS, which is based on a much larger tracking network and furthermore a combination of several individual products. The larger tangential orbit error will most likely have an impact on the real-time clock estimation. Firstly, though only approximately 25% of the along-track error will affect the clock-estimation if the GIOVE satellite is tracked at a low elevation, the projected error will still reach decimeter level. Secondly, as demonstrated in Sec. 4.5.2, an along-track error leads to an accumulating bias in the clock estimate.

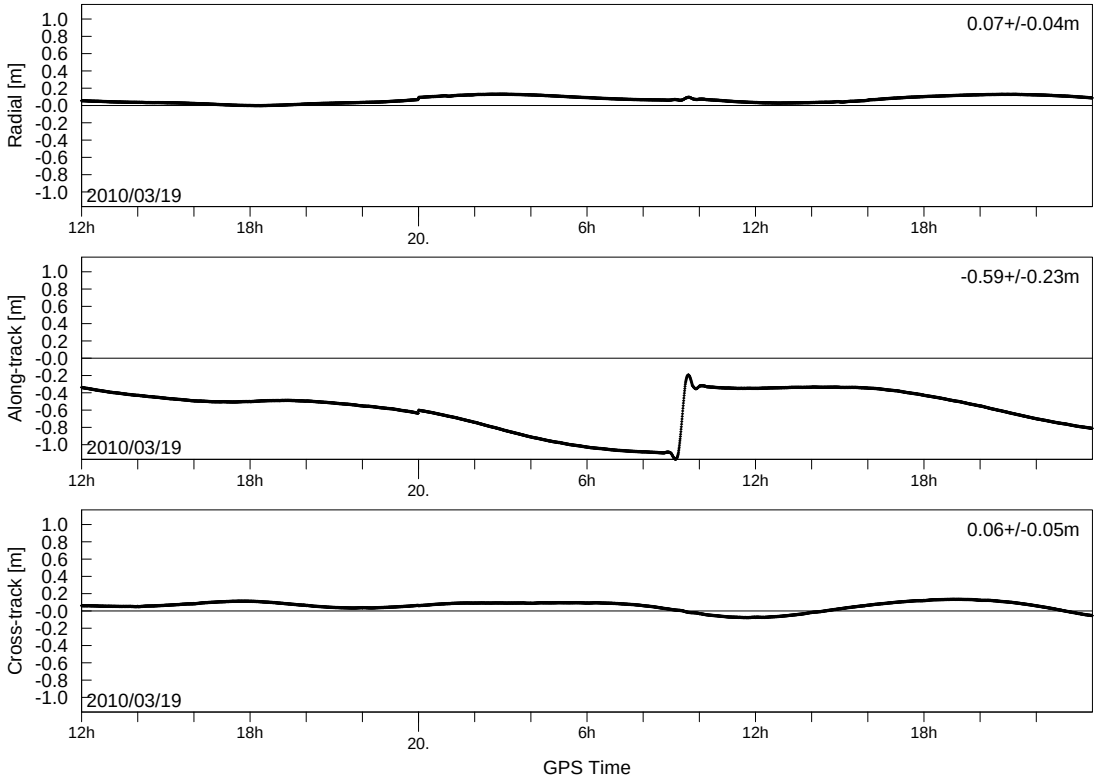

Fig. 7.2: Radial-, Tangential- and Normal-Errors of GIOVE-B orbit prediction over a 36 hour period starting at March 19th, 2010, 12h GPST. Reference trajectory is the final GIOVE orbit from IAPG.

Though the real-time clock estimation for GIOVE with RETICLE has many similarities with the GPS processing, some differences exist, which should be briefly mentioned in the following. First of all, the selected clock model for GIOVE-A and -B is identical to the model used for GPS, which is a linear clock model with process noise on the offset as well as on the drift term. It is interesting to note at this point that the clock drift for GIOVE-A is on the order of 13 cm/s, which is two orders of magnitude higher than typical drifts of GPS satellite clocks. For GIOVE-B a clock drift on the order of 2 cm/s is observed, which is still one order of magnitude higher compared to GPS. The process noise settings for both GIOVE satellites are identical to the values for GPS as provided in Tab. 4.1. This approach may penalize especially the Passive Hydrogen

Maser on GIOVE-B, which has been shown in Fig. 2.1 to have a lower Allen deviation than all GPS clocks (see also Waller et al. [2009]). However, the lower accuracy of the predicted GIOVE orbits and the low depth-of-coverage in the CONGO network will cause the real-time clock estimation to be sensitive to other errors and the deficiencies in the clock model will most likely not be notable. For the GIOVE clock estimation, the Kalman filter of RETICLE has been extended by two additional clock offset parameters. The filter processes the ionosphere-free combination based on the measurements from the E1- and the E5a-frequencies. For the Javad- and Leica-receivers, the combined data- and pilot-signal has been selected. For the GeNeRx-receivers, the data signals are used. It should be noted that the selection of signals differs from ESA, which uses the E1- and E5b-frequencies for operational processing [Píriz et al., 2006]. Data-editing and modeling of the GIOVE observations are to a large extent identical to GPS. The main difference is the inclusion of the inter-system bias in the model of the GIOVE pseudorange observations as already derived in Sec. 4.2.6. In the filter implementation, however, two simplifications are made. Firstly, the inter-system bias $b_{\mathrm{ISB,IF(E1X,E5X)-IF(P1,P2)}}$ and the receiver-dependent code bias $b_{\mathrm{rcv,IF(C,D)}}$ are combined into a single inter-system/inter-signal bias parameter b_{ISSB} for each station. The satellite-dependent bias is merged into the GIOVE satellite clock offset, since it is identical for each station. Therefore, the observation equation for pseudoranges of the GIOVE satellites can be written as:

$$\begin{aligned}\rho_n^{(s)} =& |\boldsymbol{r}^{(s)} - \boldsymbol{r}_n| + c\left(\delta t_n - \delta t^{(s)}\right) + c\delta t_{\mathrm{rel}} + T_n^{(s)} \\ &+ b_{\mathrm{ISSB}} + b_{\mathrm{PCO}} + b_{\mathrm{PCV}}\end{aligned} \tag{7.1}$$

The combined inter-system/inter-signal biases are not part of RETICLE's estimation parameters, but are instead obtained from IAPG/TUM as well. The biases are estimated in the course of the GIOVE processing and updated once every day. However, Eq. 7.1 yields an underdetermined system, since a common offset in all station-biases could be compensated for by a common offset (with opposite sign) in all GIOVE clock estimates. Therefore, the station-bias of one CONGO station is constrained to zero. The station UNBD in Canada has been selected as the reference station for the bias estimation and all station-biases are estimated as differential inter-system/inter-signal biases with respect to UNBD. The PCO-corrections in Eq. 7.1 are based on the antenna offset described by Zandbergen and Navarro [2008]. The z-offsets of GIOVE-A and -B for the E1 and E5a signals are listed in Tab. 7.1. It is important that users of the RETICLE products apply the same antenna z-offsets in their processing. The offsets in the x- and y-directions are only on the order of a few millimeters and can be neglected.

Tab. 7.1: Phase center offsets in z-direction for GIOVE-A and GIOVE-B as used in the RETICLE processing [Zandbergen and Navarro, 2008]

	E1 [mm]	E5a [mm]
GIOVE-A	874.0	869.0
GIOVE-B	1351.2	1350.1

The plot in Fig. 7.3 shows the clock errors of GIOVE-A and GIOVE-B for the selected test period. The clock error has been computed with respect to the final GIOVE clock solution from IAPG. Before discussing the clock results, a short remark concerning the effects of the clock constraint should be added. In the clock constraint applied

to the estimated clock, the mean of the estimated GPS clocks is constrained to the mean of the clock offsets in the IGU product. The constraint on the satellite clocks also constrains all ground station clocks. Though the GIOVE satellites are not explicitly included in the GPS clock constraint, it also acts indirectly on the GIOVE clocks via the receiver clocks. As a result, the GIOVE real-time clock estimates can only be used consistently with the corresponding GPS real-time clocks. The same reasoning also holds true for the final GIOVE products from IAPG, which are archived together with the corresponding CODE rapid orbits to allow consistent processing. For the plot in Fig. 7.3, the common offset of the GPS clocks in the RETICLE product and the reference product have been removed from the GIOVE clocks to show the real clock error, which affects the user's positioning solution.

The high variation of the clock estimates at the beginning of the plot is due to the initialization of the clock estimation, which took place at approximately 12:00h. After that the clocks exhibit a comparably smooth behavior, but a significant drift is notable, which leads to an accumulated error of approximately -0.8 m for GIOVE-A and -0.5 m for GIOVE-B. The maximum errors are reached at at approximately 9:30h for GIOVE-A and 10:30h for GIOVE-B. Afterwards, the clock errors quickly decrease to less than -0.2 cm. The reasons for the discontinuities of GIOVE-A at midnight between March 19th and 20th as well as the joint discontinuity of both satellites at approximately 12:00h on March 20th could not be identified.

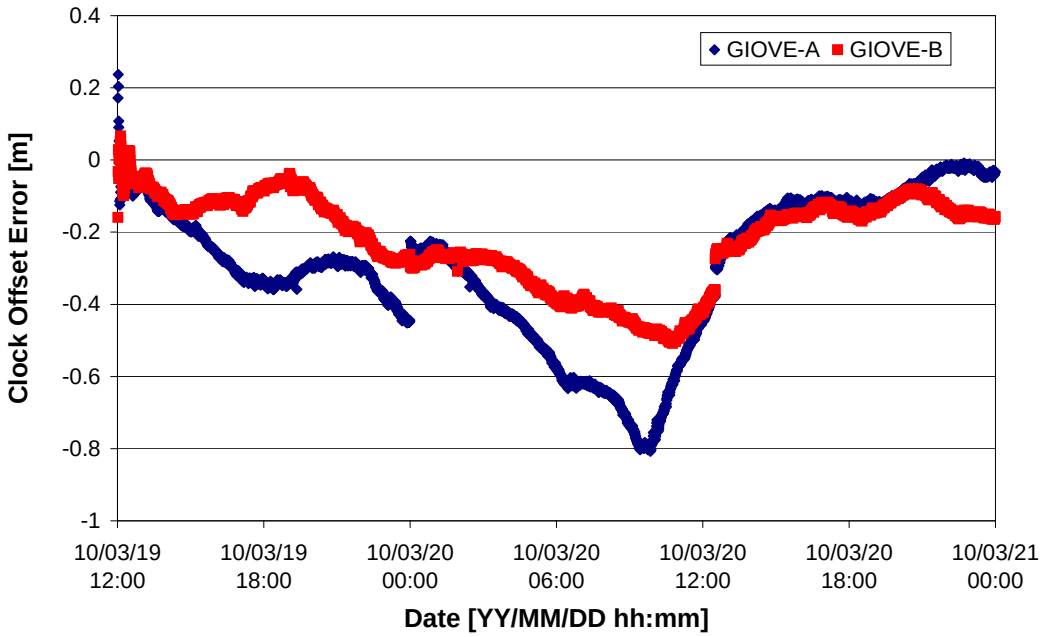

Fig. 7.3: Real-time clock estimation errors for GIOVE-A (blue) and GIOVE-B (red). The reference clock solution is obtained from the final GIOVE product from IAPG.

The errors in the real-time GIOVE clock estimation can be attributed to multiple causes. The orbit errors of the predicted product will have an effect on the real time clock estimation. As already mentioned, the projection of the along-track orbit errors on the line-of-sight vector has an effect on the clock estimate, which can reach decimeter level. Secondly, as shown in the previous analysis, an accumulating effect is caused

by this orbit error component. Both GIOVE satellites exhibit an increasing negative bias of the clock error and an orbit error in the anti-flight direction, which is sign-consistent with the derivations presented in Sec. 4.5.2 and suggests that the accumulation of the clock error is caused by the along-track orbit error. Though process noise has also been applied to the GIOVE carrier-phase ambiguities to mitigate this effect, the orbit errors are significantly larger than for GPS. The applied process-noise is obviously not sufficient to suppress the accumulation of the error, but only reduces the effect. Secondly, uncertainties in the estimation of the station-biases will also have an effect on the clock estimation. Due to the fact that the inter-system biases are estimated based on the measurements from only two satellites, local multipath errors or elevation-dependent pseudorange biases will affect the estimation. Since the observation geometry for the GIOVE satellites changes from day to day, the effect of systematic errors on the bias estimation also changes and causes a variation of the daily estimates [Montenbruck and Hauschild, 2010].

Fig. 7.4 depicts the variation of the inter-system/inter-signal bias for selected stations of the CONGO network over a time period of 80 days. Note that the absolute values have been shifted in order to increase the readability of the plot. The previously mentioned day-to-day variations on the nano-second level become obvious. Furthermore, several large discontinuities are present in the data. The first occurs on day 217, when the ISSB for MAHO experiences a 10 ns jump. Next, on day 229, the stations CHOF and HRAG exhibit discontinuities, which are of similar magnitude. Finally, on day 238, all four stations exhibit a discontinuity of the same magnitude and sign.

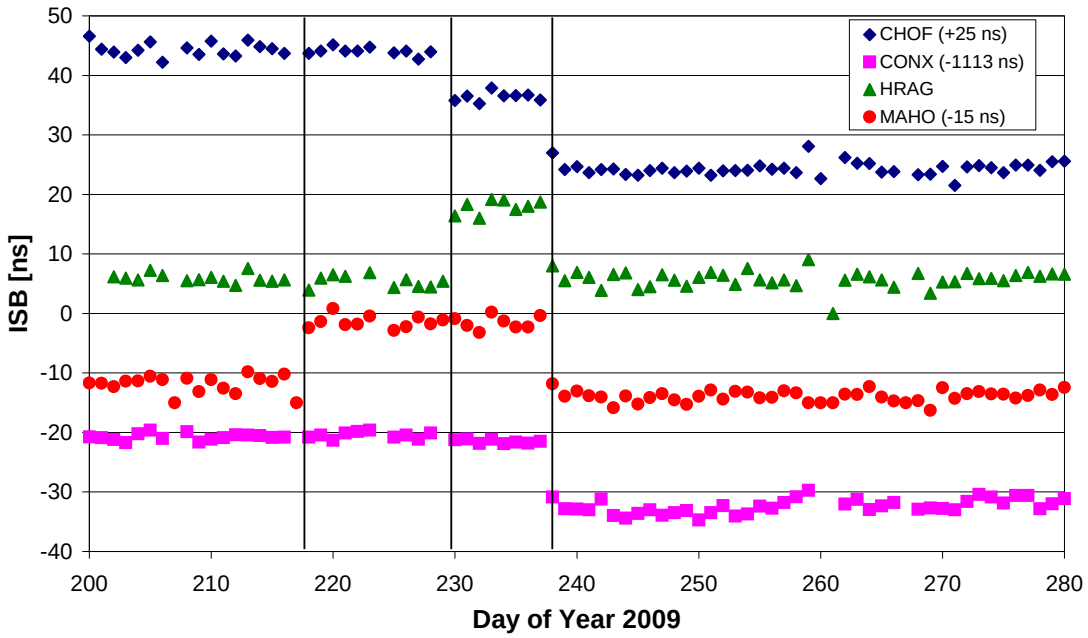

Fig. 7.4: Inter-system/inter-signal bias variations for selected CONGO stations estimated by IAPG. Note that the biases have been offset for better readability.

The explanation of this phenomenon is that on the corresponding days, the receiver firmware of the Javad-receivers has been updated. The new firmware release had modified tracking loop settings, which affected the signal tracking and therefore affected

the ISSB. On day 238, the firmware of the ISSB reference station UNBD was updated, which explains why a discontinuity is visible for all other stations in the network even though their firmware or hardware has not been modified. This information is important for the handling of ISSBs and has implications on the interoperability of different satellite systems. Obviously, hardware changes or manipulations of the receiver's tracking loops affect the bias. The latter can also happen unintentionally through the change in the firmware. As a consequence, the ISSB of the affected station must be re-calibrated or estimated on the fly to allow consistent processing of observations of different navigation systems.

7.2 Combined GPS/GIOVE Positioning

In order to evaluate the performance of the GIOVE clock offset estimation, a combined GPS and GIOVE positioning solution has been computed with two different techniques. The first is referred to as a Single-Point Positioning (SPP) solution and makes use of dual-frequency pseudorange measurements only, whereas, carrier-phase observations are not used. The second is a Precise Point Positioning (PPP) using pseudoranges and carrier-phases. The algorithms used for both tests will be introduced in further detail in the corresponding sections. In order to provide representative results, measurements from a station, which is not included in the real-time clock estimation, have been used. This station is operated at Technical University Darmstadt (Technische Universität Darmstadt, TUD). The receiver is a Leica GRX1200+GNSS with a Leica AX1203+GNSS antenna mounted to the roof of a building. The reference position of the antenna has been obtained from a GPS-only PPP using a data arc of 24 hours. The inter-system bias for this station has been determined from the mean residuals of the final GIOVE orbit and clock product from TUM and amounts to 3.79 m (12.6 ns). A test period with simultaneous visibility of GIOVE-A and GIOVE-B has been selected for the analysis, which starts at 2:30h GPST and ends at 9:30h GPST on March 20th, 2010. GIOVE-A has reached an elevation of 34° and GIOVE-B is at 46° at the beginning of the test period. Tracking of the GIOVE satellites ends at an elevation of about 10°, at approximately 9:00h GPST for GIOVE-A and approximately 8:30h GPST for GIOVE-B. A sky plot of the tracked GPS and GIOVE satellites is shown in Fig. 7.5.

7.2.1 Single Point Positioning

The single-point-positioning algorithm uses dual-frequency pseudorange measurements only. A positioning solution is computed at each single epoch (point) using a least-squares fit. The tropospheric delay is corrected using the UNB3-model [Collins et al., 1996]. Screening of residuals is used in the data editing process. If the RMS of the pseudorange residuals exceed a threshold, the position solution and the RMS residual is recomputed with a single satellite rejected. This procedure is repeated with each satellite tracked at this epoch to find the subset-solution which yields the lowest residual. The rejected satellite is then omitted from the navigation solution at this epoch. Observations with a SNR of less than 15 dB-Hz and an elevation of 10° are rejected from the processing. The standard deviation of the pseudorange measurements is set to 1.5 m.

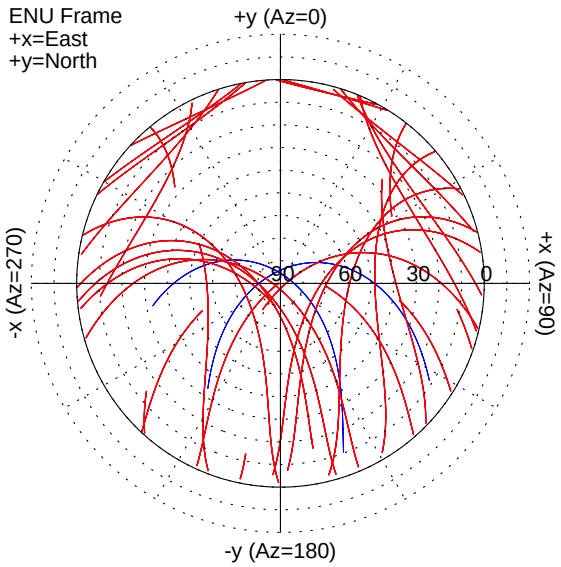

Fig. 7.5: Sky plot of visible GPS satellites (red) and GIOVE satellites (blue) during the test period

The results for the single point positioning are summarized in Tab. 7.2. The 3-D position error with respect to the reference position is 1.98 m for GPS-only processing and 1.86 m when GPS and GIOVE are processed. Obviously, the combined effect of the orbit and clock error of the GIOVE satellites, which have shown to be on the order of a few decimeters, does not adversely affect the single-point-positioning. It is interesting to note that the small improvement in the positioning solution is almost entirely gained in the up direction, whereas the horizontal position errors remain almost the same. Fig. 7.5 makes obvious, that GIOVE-A and -B both have high passes over the station location with maximum elevation of more than 80° . Including these two additional satellites obviously improves the observation geometry and leads to a better determination of the height component.

Tab. 7.2: RMS position errors for single point positioning with GPS-only and combined GPS/GIOVE processing

	East Error [m]	North Error [m]	Up Error [m]	3-D Error [m]
GPS	0.63	0.88	1.65	1.98
GPS/GIOVE	0.64	0.86	1.52	1.86

7.2.2 Precise Point Positioning

Complementary to the single-point-positioning analysis, an analysis using a precise-point-positioning software has been used. The PPP program uses dual-frequency pseudorange and carrier-phase measurements in a Kalman filter to compute a position solution in forward only mode. The Kalman filter state comprises the position vector, the receiver clock offset, the tropospheric delay and the carrier-phase ambiguities for all satellites included in the processing. The estimate of the tropospheric delay is a correction for the non-hydrostatic component to the modeled tropospheric delay from the UNB3 model. The Kalman filter assumes a static position with only a low amount

of processing noise. Data editing for the pseudorange measurements is performed in the same way as in the single-point-positioning algorithm. Additionally, a RMS-based editing is also performed on time-differences of the carrier-phase observations. The processing options for the PPP are summarized in Tab. 7.3. The initial position in the filter state is initialized with an offset of 1 m with respect to the true antenna position. Identical settings have been used for the GPS-only and the mixed processing.

Tab. 7.3: Filter settings for PPP Kalman filter

Edit Limits:			
Elevation	11.0°		
SNR	15.0 dB-Hz		
Code-Carrier-Difference	10.0 m		
Pseudorange RMS	2.0 m		
Carrier-Phase RMS	0.05 m		
Process Noise:	σ_0	σ	τ
Position	5 m	0.001 m	600 s
Tropospheric zenith delay	0.1 m	0.001 m	3600 s
Ambiguities	5 m		
Measurement Noise:			
Pseudorange		1.0 m	
Carrier Phase		5 mm	

The 3-D positioning errors are summarized in Tab. 7.4. GPS-only processing yields RMS position errors of 4.9 cm, 3.2 cm and 3.4 cm for the East-, North- and Up-components, respectively. The 3-D position error is 6.8 cm. The inclusion of the GIOVE satellites leads to a significant increase in the position error. The 3-D RMS error is now approximately 12 cm. Obviously, adverse effects due to the increased clock estimation errors of the GIOVE satellites compared to the GPS satellites become notable in the combined PPP. It should be noted that the first five minutes have been omitted for both solutions to take the convergence time of the Kalman filter out of the statistics. During the convergence time, the position errors are significantly larger.

Tab. 7.4: RMS position errors for precise point positioning with GPS-only and combined GPS/GIOVE processing without the convergence period of 5 min

	East Error [cm]	North Error [cm]	Up Error [cm]	3-D Error [cm]
GPS	4.9	3.2	3.4	6.8
GPS/GIOVE	7.6	4.9	7.3	11.6

To further illustrate this effect, a time series of the position errors for GPS and mixed GPS/GIOVE processing is plotted in Fig. 7.6 and Fig. 7.7, respectively. Fig. 7.6 shows that the position errors rapidly converge to less than a decimeter and remain there for the entire test period for the GPS-only processing.

In comparison, Fig. 7.7 for the mixed processing shows significant deviations especially of the East- and Up-components. It becomes obvious though, that the convergence of the PPP solution with the additional GIOVE satellites seems to be quicker than for the GPS-only solution. Direct comparison of the first data points of Fig. 7.6

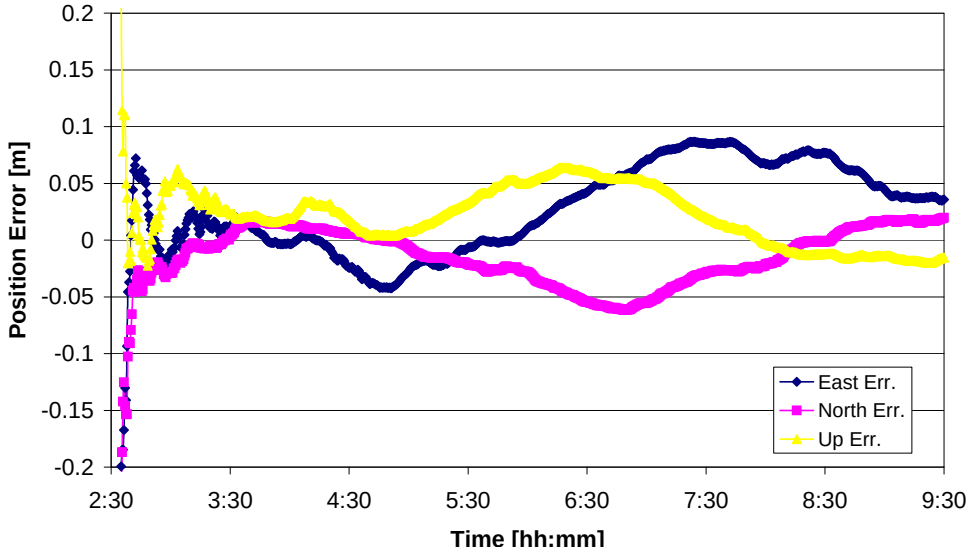

Fig. 7.6: Time series of North-, East- and Up-position errors for GPS-only PPP. First five minutes with filter convergence are omitted.

and Fig. 7.7 reveals, that the combined GPS/GIOVE position solution reaches lower position errors more quickly than the GPS-only solution. This can also be seen when computing the RMS position errors for the first 10 min after the start of the PPP. During the convergence time, the 3-D RMS position error is 44 cm for the GPS-only processing and 39 cm for the combined processing. Obviously, the additional GIOVE observations assist during the convergence phase. However, despite the more rapid convergence, the combined solution cannot reach the high position accuracy as obtained without the use of GIOVE.

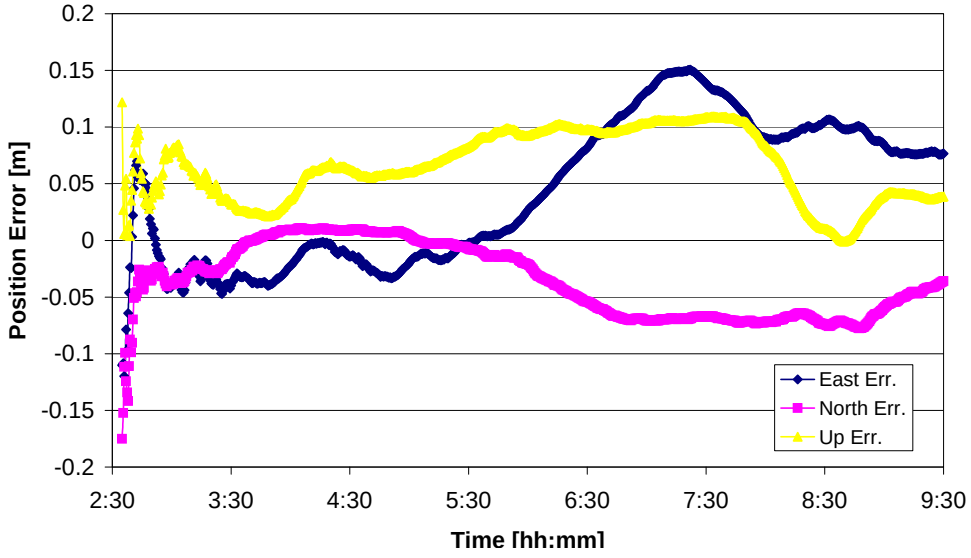

Fig. 7.7: Time series of North-, East- and Up-position errors for mixed GPS/GIOVE PPP. First five minutes with filter convergence are omitted.

The degradation of the position solution obvious in Fig. 7.7 can be attributed to two main causes: Firstly, a bias in the estimated GIOVE real-time clock offsets and, secondly, a reduced stability of the clock estimate over time compared to the GPS satellites. Indications can be found when regarding the pseudorange and carrier-phase residuals from the PPP, which are summarized in Tab. 7.5. It becomes obvious that for the GPS-only processing, the residuals of the carrier-phase have zero mean and a standard deviation of approximately 1 cm. The pseudoranges have a negligible bias of 2.8 cm and a standard deviation of 86 cm. The pseudorange observations of GIOVE on the other hand exhibit a bias of -32.5 cm. This bias is again consistent with the magnitude of the clock errors for GIOVE-A and GIOVE-B shown in Fig. 7.3. The GPS pseudrange residuals exhibit a significantly increased bias in the mixed positioning, which is due to the fact that all GPS and GIOVE observations are assigned with identical weights irrespective of their true modeling accuracy. De-weighting the GIOVE observations with a higher measurement noise compared to GPS would reduce their impact. As a result, the GPS residuals would decrease and the GIOVE residuals would further increase [Cao et al., 2010]. The mean and the standard deviation of the carrier-phase residuals are also significantly larger compared to the GPS-only processing. This result could be expected since the clock errors of the GIOVE satellites are obviously not stable over the duration of the pass.

Tab. 7.5: Mean and standard deviation of pseudorange and carrier-phase residuals from GPS-only and mixed GPS/GIOVE PPP

	GPS		GIOVE	
	PR [cm]	CP [cm]	PR [cm]	CP [cm]
GPS	2.8±86.0	0.0±1.0	-	-
GPS/GIOVE	9.9±87.5	-0.5±1.4	-32.5±94.3	2.5±3.2

The analysis leads to the conclusion that contrary to the single-point-positioning solution, where a slight improvement is gained with the additional satellites, the PPP solution cannot benefit from the inclusion of GIOVE. These findings are consistent with the results obtained from earlier experiments [Cao et al., 2010].

Even though RETICLE's GIOVE real-time clock estimates based on data from the CONGO network may not yet reach up to the quality which is achieved for the GPS clocks, the availability of such products will open up many research opportunities for multi-GNSS real-time applications. With further upgrades of the CONGO station equipment and additional stations to be employed, the quality of the real-time clock estimates will be improved even further. Also, additional real-time PPP experiments with GPS and GIOVE should be conducted over a longer test period to gain long-term statistics of the achievable positioning accuracy.

8. Summary, Conclusions and Future Work

In the course of this thesis, a real-time GNSS clock estimation system has been developed. The clock prediction error is currently the limiting factor in (near) real-time precise positioning applications, like orbit determination for LEO satellites and ground based navigation. The clock estimation is based on the measurements of the global real-time tracking station network of the International GNSS Service. The implemented algorithm is based on a Kalman filter, which processes the ionosphere-free combination of dual-frequency measurements of GPS and the new GIOVE satellites and estimates precise clock corrections based on predicted orbits. The output is available to users with a low latency of a few seconds. The algorithms described in the thesis have also been implemented in the real-time clock estimation system RETICLE, which has been operated continuously at GSOC/DLR for more than a year. The modeling of the GNSS observations and the design of the filter are explicitly described. A clock discontinuity detection and mitigation method has been implemented in the filter, which eliminates the adverse effects of clock discontinuities on the estimation process. It is also a first step towards a global integrity monitoring of GNSS satellites, a topic which will gain more attention in the future, for example, in view of the demanding requirements of air-traffic applications. Furthermore, the different effects of orbit errors in radial, along-track and cross-track directions on the clock estimation have been studied. The investigation shows that along-track orbit errors lead to an accumulating clock error. This effect could also be observed in the real-time clock estimation system. A mitigation method to avoid the accumulated error is proposed and proven to improve the accuracy of the RETICLE clock estimates.

The performance assessment of the real-time clock estimates has been done with precise orbit determination estimation of a LEO satellite. Simulations of near real-time orbit determination have been performed with real flight data of the TerraSAR-X satellite in a realistic scenario. The results show, that an accuracy of typically less than 5 cm can be achieved with a reduced dynamic POD over the entire test period of 20 days. The 3-D velocity error is less than 0.1 mm/s. These accuracies fully satisfy the mission requirements of radar altimetry and occultation missions, for which near real-time POD is most relevant. In a complementary analysis, a kinematic POD has also been performed. The analysis showed that an accuracy on the order of a decimeter could be reached for the first ten days. During the second half of the test period, the processing of occultation measurements was activated on-board the satellite, which lead to a reduction in the number of tracked satellites per day. As a result, the orbit determination accuracy is significantly reduced during the second half of the test period. Finally, a simulation with a real-time capable navigation algorithm has been performed to demonstrate the

possible performance, if the real-time clock products were broadcast by a network of geostationary relay satellites for on-board use.

The clock solutions of the RETICLE system are submitted to the IGS real-time pilot project for inter-agency comparisons to the latest IGS Rapid products since more than a year. The statistics gained from the comparisons have been presented. It becomes obvious, that RETICLE is competitive to the solutions of the three other real-time analysis centers, which submit their clock products to the project.

Finally, the results of the first real-time clock estimation for the GIOVE satellites are presented. The measurements stem from the CONGO-network, a global tracking network set-up in a joint effort by BKG and DLR. The orbits for the real-time clock estimation are generated by IAPG/TUM. The orbit and clock accuracy of GIOVE is shown to be at the decimeter level. Using the combined real-time clock product in a positioning application shows that a slight improvement is gained in single-point-positioning. Precise point positioning, on the other hand, suffers from the lower accuracy of the GIOVE ephemerides compared to GPS. The selected test case demonstrates the ability of multi-GNSS positioning with real-time products, but does not provide sound statistics of the achievable performance. Therefore, additional experiments with mixed GIOVE and GPS positioning will be conducted in the future.

Besides these experiments, the RETICLE system offers a broad variety of possibilities for future studies in the field of real-time GNSS processing. The application of integrity-monitoring has already been mentioned. In the near future, the demand of the provision of a guaranteed service from global navigation systems will rise. In these scenarios, the users must be notified in a timely manner about the expected accuracy of the navigation service as well as anomalies in the system. The clock discontinuity detection of RETICLE is a first step towards a global integrity monitoring. It could be envisaged to include other performance measures into the monitoring, for example orbit error monitoring in case a maneuvering satellite has not been set unhealthy.

For this purpose, the state vector of the RETICLE filter could be extended to also include orbit corrections together with the clock offset estimates. This approach appears attractive, since it can potentially also eliminate or at least reduce the along-track orbit error, which has been shown to be responsible for accumulating clock errors. As a first approach, the filter could be extended by only a single state per satellite to compensate for the tangential error component, which is also the largest one in the orbit predictions for GPS as well as GIOVE. The high depth-of-coverage of the tracking network for GPS should allow for the estimation of another parameter per satellite without problems. The reduction of the along-track error by means of orbit corrections would also erase the need for the process noise to be applied on the carrier-phase ambiguities and would likely lead to an overall improvement of the clock estimation. It must be evaluated if the estimation of orbit corrections for GIOVE can be reliably done with the CONGO network in its current state of extension.

Besides the inclusion of orbit corrections, other refinements in the modeling of the estimation parameters of the Kalman filter could bring advantages. Firstly, more elaborated settings for the satellite clock noise may lead to a further improvement of the estimation accuracy. For simplicity, the process noise settings for all satellites in the RETICLE filter are currently identical. With the high accuracy which has now been

reached in the real-time clock estimation, the deficiencies of these simplified models may become visible. In the future, individual settings for each satellite could be adopted and updated based on the recent clock performance of the satellite. Secondly, the receiver clocks and the tropospheric zenith-delay corrections are modeled as integrated white noise processes with linear increase of the covariance over time. This approach brings the disadvantage, that station outages must be detected and handled in the filter to avoid an unlimited growth of the covariance. Modelling these parameters as exponentially correlated random variables (ECRV) would avoid this complication, since the state and covariance for ECRVs have an asymptotic behaviour [Neirinchx, 1992]. If a station exhibits a longer outage, the covariance of the receiver clock offset and the troposheric delay approaches a pre-defined covariance value and the states decrease to zero depending on an associated time constant. The covariance value can be chosen such that it corresponds to the conditions at re-initialization of the states for the corresponding station. To account for the different characteristics of the receiver clock and the tropospheric delay, a short time constant should be chosen for the clock offset to reflect the noise-like behaviour of this estimation parameter, whereas the slowly changing tropospheric correction can be assigned a longer time constant.

Another effect, which will become more important in the future, is the second-order error of the ionosphere. Whereas the first-order effects are eliminated via the linear data combination of dual frequencies, higher order effects are still present in the measurements and are currently not modeled. At the time of writing, the solar activity is at the end of a calm period and heading towards the next solar maximum. With the increasing activity in the ionosphere, the residual higher order errors will gain a higher impact on the measurements. In the near future, options for the implementation of higher order ionospheric corrections in RETICLE should be investigated.

Finally, the clock estimation can be extended to systems other than GPS and GIOVE. The Russian GLONASS system is being rapidly rebuilt and will most likely achieve the full constellation soon. The real-time estimation of GLONASS clocks is of high interest for the PPP users, since the availability of these clock correction would almost double the number of satellites available for positioning with most geodetic receivers. The Galileo system is also expected to start the launch of the first in-orbit-validation (IOV) satellites of the constellation. China is also undertaking efforts to build up a navigation system. Furthermore, new satellite-based augmentation systems are being developed, whose satellites broadcast integrity information for a certain coverage area and can be used in mixed GNSS positioning. One example is the future Japanese Quasi-Zenith-Satellite-System (QZSS), which will transmit on the L1, L2 and L5 frequencies and will be interoperable with GPS. The coverage area of this satellite will include Japan, Australia and Southeast Asia and will therefore be interesting for a significant user community [IS-QZSS, 2009]. The launch of the first QZSS satellite is currently planned for summer 2010. RETICLE can easily be extended to these new satellites, which will be interesting for the research community working on multi-GNSS real-time precise positioning.

Table of Symbols

$^{(s)}$	Superscript indicating satellite s
$_{n}$	Subscript indicating reference station n
$_{k}$	Subscript for epoch k
$^{-}$	Superscript state prior to measurement update
$^{+}$	Superscript state after measurement update
A	Float ambiguity
a	Projection of orbit error on line-of-sight vector
a_z	Satellite antenna offset in z-direction from COM
b_{DCB}	Differential code bias correction
b_{ISSB}	Inter-signal/inter-system bias
b_{PCO}	Phase center offset correction
b_{PCV}	Phase center variation correction
$\boldsymbol{b}_{PCO}$	Phase center offset vector
c	Speed of light
D_d	Dry tropospheric zenith delay
D_w	Wet tropospheric zenith delay
$\boldsymbol{D}$	Effective dipole of receiving antenna
$\boldsymbol{D}'$	Effective dipole of transmitting antenna
$\hat{\boldsymbol{e}}$	Unit line-of-sight vector from reference station to satellite
e	Orbit/clock error
f	Frequency
$\boldsymbol{h}$	Mapping function of state vector to modeled observtions
$\boldsymbol{H}$	Sensitivity matrix
$\boldsymbol{I}$	Identity matrix
$\boldsymbol{k}$	Unit vector pointing from transmitting to receiving antenna
$\boldsymbol{K}$	Kalman gain matrix
M_d	Dry mapping function
M_w	Wet mapping function
$\hat{\boldsymbol{m}}$	Unit vector poining to receiving antenna dipole element
$\hat{\boldsymbol{m}}'$	Unit vector poining to transmitting antenna dipole element
$\hat{\boldsymbol{n}}$	Unit vector poining to receiving antenna dipole element
$\hat{\boldsymbol{n}}'$	Unit vector poining to transmitting antenna dipole element
N	Integer ambiguity
$\boldsymbol{P}$	Covariance matrix of state vector
$\boldsymbol{Q}$	Process noise matrix

$\boldsymbol{r}$	Position vector
$\boldsymbol{R}$	Covariance matrix of measurements
T	Tropospheric delay
dT	Differential tropospheric delay
$\boldsymbol{v}$	Velocity vector
$\boldsymbol{x}$	Kalman filter state vector
$\boldsymbol{y}$	Measurement vector
$\tilde{\boldsymbol{y}}$	Modelled measurement vector
$\mathbf{0}$	Zero matrix
ζ	Auxiliary variable
$\Delta\boldsymbol{r}_{ecc}$	Eccentricity vector
$\Delta\boldsymbol{r}_{ET}$	Solid Earth tide displacement vector
$\Delta\boldsymbol{r}_{OL}$	Ocean loading displacement vector
$\Delta\boldsymbol{r}_{PT}$	Polar tides displacement vector
Δt	Time step
δt	Clock offset
δt_{rel}	Relativistic clock correction
ε	Residual errors (receiver noise + multipath)
λ	Wavelength
$\mu_{\oplus}$	Gravitational constant of the Earth
ρ	Pseudorange observable
σ	Standard deviation
τ	Time constant
$\boldsymbol{v}$	Noise vector of measurements
Φ	Carrier-phase observable
$\boldsymbol{\Phi}$	State transition matrix

Table of Abbreviations

AC	Analysis Center
ADEV	Allan Deviation
AFS	Atomic Frequency Standard
AIUB	Astronomical Institute of University Berne
APC	Antenna Phase Center
ARP	Antenna Reference Point
CAFS	Cesium Atomic Frequency Standard
BCE	Broadcast Ephemeris
BKG	Bundesamt für Kartographie und Geodäsie
CEST	Clock ESTimation (offline version of RETICLE)
CODE	Center for Orbit Determination in Europe
CONGO	COperative Network for Giove Observation
COM	Center Of Mass
DCB	Differential Code Bias
DLR	Deutsches Zentrum für Luft- und Raumfahrt
DOC	Depth-Of-Coverage
DOP	Dilution Of Precision
ECEF	Earth-Centered Earth-Fixed
ESA	European Space Agency
ESOC	European Space Operations Center
EOP	Earth Orientation Parameter
EU	European Union
FW	Firmware
GDGPS	Global Differential GPS
GIM	Global Ionosphere Map
GIOVE	Galileo In-Orbit Validation Element
GNSS	Global Navigation Satellite System
GPS	Global Positioning System
GPST	Global Positioning System Time
GSA	GNSS Supervisory Authority
GSOC	German Space Operations Center
HTTP	Hypertext Transfer Protocol
IAPG	Institut für Astronomische und Physikalische Geodäsie
IF	Ionosphere-Free linear combination
IGS	International GNSS Service
IGU	IGS ultra-rapid orbit and clock product

IODE	Issue Of Data, Ephemerides
IOV	In-Orbit-Validation
JPL	Jet Propulsion Laboratory
LEO	Low-Earth Orbit
MDEV	Modified Allan Deviation
NANU	Notice Advisory to Navstar Users
NOAA	National Oceanic and Atmospheric Administration
NGS	National Geodetic Survey
NRCan	Natural Resources Canada
NTRIP	Networked Transport of RTCM via Internet Protocol
PCO	Phase Center Offset
PCV	Phase Center Variation
PHM	Passive Hydrogen Maser
POD	Precise Orbit Determination
PPP	Precise Point Positioning
PWU	Carrier-phase Wind-Up
QZSS	Quasi-Zenith-Satellite-System
RAFS	Rubidium Atomic Frequency Standards
RETICLE	REal-TIme CLock Estimation
RETINA	REal-TIme NAvigation
Rinex	Receiver INdependent Exchange Format
RMS	Root-Mean-Square
RTCM	Radio Technical Commission for Maritime Services
RTIGS	Real-Time IGS
RTPP	Real-Time Pilot Project
Sinex	Solution (Software/technique) INdependent EXchange Format
SISRE	Signal-In-Space Range Error
SLR	Satellite Laser Ranging
SNR	Signal-to-Noise Ratio
SSP	Sub-Satellite-Point
SSR	State Space Representation
TCP	Transmission Control Protocol
TDRSS	Tracking and Data Relay Satellite System
TEC	Total Electron Content
TKS	Time Keeping System
TUD	Technische Universität Darmstadt
TUM	Technische Universität München
UDP	User Datagram Protocol
UERE	User Equivalent Range Error
USNO	United States Naval Observatory
VCXO	Voltage Controlled Crystal Oscillator

Bibliography

L. Agrotis. Minutes of IGS RTPP Telecon. October 2008.

L. Agrotis, J. Dow, C.-G. Martinez, A. Ballereau, and J. Pérez. Real Time GNSS Processing at ESOC: Infrastructure and Initial Results. presented at IGS Workshop 2008, Miami, FL, USA, 2008.

D. W. Allan. Clock Characterization Tutorial. In *Proceedings of the 15th Annual Precise Time and Time Interval (PTTI) Applications and Planning Meeting, December 06 - 08, 1983*, Washington, D.C., USA, 1983.

D. W. Allan. Time and Frequency (Time-Domain) Characterization, Estimation, and Prediction of Precision Clocks and Oscillators. In *IEEE Transactions on Ultrasonics, Ferroelectrics and Frequency Control, November 1987*, volume UFFC-34, Washington, D.C., USA, 1987.

Y. Andres, P.L. Righetti, and A. Soerensen. JASON-2 Near Real Time Precise Orbit Determination Based on GRAS GSN. In *Proceedings of the 21st International Symposium on Space Flight Dynamics, 28 Sep. - 2 Oct. 2009*, Toulouse, France, 2009.

C. Audoin and B. Guinot. *The Measurement of Time - Time, Frequency and the Atomic Clock*. University Press, Cambridge, 2001.

T. B. Bahder. Relativity of GPS Measurement. *Phys. Rev. D*, 68(6):063005, September 2003.

Y. Bar-Sever, L. Young, F. Stocklin, P. Heffernan, and J. Rush. The NASA Global Differential GPS System (GDGPS) And The TDRSS Augmentation Service for Satellites (TASS). In *Procedings of ESA's 2nd Workshop on navigation equipment*, Noordwijk, The Netherlands, December 2004.

S. Bassiri and G. A. Hajj. Higher-order Ionospheric Effects on the Global Positioning System Observables and Means of Modeling Them. *Manuscripta Geodaetica*, 18(6): 280–289, 1993.

W. I. Bertiger, Y. E. Bar-Sever, B. J. Haines, B. A. Iijima, S. M. Lichten, U. J. Lindqwister, A. J. Mannucci, R. J. Muellerschoen, T. N. Munson, A. W. Moore, L. J. Romans, B. D. Wilson, S. C. Wu, T. P. Yunck, G. Piesinger, and M. L. Whitehead. A Real-Time Wide Area Differential GPS System. *Journal of the Institute of Navigation*, 44 (4):433–447, 1998.

BKG. IGS-IP Ntrip Broadcaster. published online, 2009. URL www.igs-ip.net/home. last accessed November 2009.

H. Bock, R. Dach, Y. Yoon, and O. Montenbruck. GPS Clock Correction Estimation for Near Real-time Orbit Determination Applications. *Aerosp. Science and Technology*, 13(7):415–422, 2009. doi: DOI10.1016/j.ast.2009.08.003.

W. Cao, A. Hauschild, P. Steigenberger, R. B. Langley, L. Urquhart, Marcelo Santos, and Oliver Montenbruck. Performance Evaluation of Integrated GPS/GIOVE Precise Point Positioning. In *Proceedings of the ION ITM*, San Diego, CA, USA, 2010.

P. Collins, R. B. Langley, and J. LaMance. Limiting Factors in Tropospheric Propagation Delay Error Modelling for GPS Airborne Navigation. In *Proceedings of The Institute of Navigation 52nd Annual Meeting, June 19-21 1996*, pages 519–528, Cambridge, Massachusetts, 1996.

J. L. Crassidis and J. L. Junkins. *Optimal Estimation of Dynamical Systems*. Chapman & Hall/CRC, 2004.

R. Dach, U. Hugentobler, P. Fridez, and M. Meindl. *Bernese GPS Software Version 5.0*. Astronomical Institute, University of Bern, Bern, Switzerland, 2007.

T. Dass, G. Freed, J. Petzinger, and J. Rajan. GPS Clocks in Space: Current Performance and Plans for the Future. In *Proceedings of Precise Time and Time Interval Systems and Applications Meeting (PTTI), December 03 - 05, 2002*, Reston, VA, USA, 2002.

S. Datta-Barua, P. H. Doherty, S. H. Delay, T. Dehel, and J. A. Klobuchar. Ionospheric Scintillation Effects on Single and Dual Frequency GPS Positioning. In *Proceedings of the ION GPS, September 09 - 12, 2003*, Portland, Oregon, 2003.

G. L. Dieter and G. E. Hatten. Observations on the Reliability of Rubidium Frequency Standards on Block II/IIA GPS Satellites. In *Proceedings of Precise Time and Time Interval Systems and Applications Meeting (PTTI), November 29 - December 01, 1995*, San Diego, CA, USA, 1995.

J. Dow, L. Agrotis, and P. Alfaro. IGS RTPP daily clock report. published online, 2009. URL ftp://cddis.nasa.gov/gps/products/rtpp/. last accessed November 2009.

H. Dragert, T. S James, and A. Lambert. Ocean Loading Corrections for Continuous GPS: A Case Study at the Canadian Costal Site Holberg. *Geosphysical Research Letters*, 27(14):2045–2048, July 2000.

W. Emmer and E. Watts. Atomic Frequency Standards for the GPS IIF Satellites. In *Proceedings of Precise Time and Time Interval Systems and Applications Meeting (PTTI), December 02 - 04, 1997*, Long Beach, California, 1997.

P. Fang, G. Gendt, T. Springer, and T. Mannucci. IGS Near Real-Time Products and Their Applications. *GPS Solutions*, 4(4):2–8, 2001.

Y. Gao and K. Chen. Development of a Real-Time Single-Frequency Precise Point Positioning System and Test Results. In *Proceedings of the ION GNSS 2006*, Fort Worth, TX, USA, September 2005.

Y. Georgiadou and K. D. Doucet. The Issue of Selective Availability. *GPS World Magazine*, 1(5):53–56, 1990.

S. Gordon, K. Shallberga, S. Ericson, J. Grabowski, T. Morrissey, and F. Lorge. PRN-21 Carrier Phase Perturbations Observed by WAAS. In *Proceedings of the ION GNSS 2009*, Savannah, GA, USA, September 2009.

GPS-ICD-200c. *Interface Control Document: NAVSTAR GPS Space Segment. Navigation User Interface*. AIR Inc. Research Corporation, Fountain Valley, California, 1993.

A. Hauschild and O. Montenbruck. Kalman-Filter-based GPS Clock Estimation for Near Real-Time Positioning. *GPS Solutions*, 3(13):173–182, 2009.

U. Hugentobler, P. Steigenberger, O. Montenbruck, A. Hauschild, G. Weber, and U. Hessels. Evaluation of GIOVE Satellite Clocks using the CONGO Network. presented at 24th European Frequency and Time Forum 2010, ESTEC, Noordwijk, The Netherlands, April 2010.

S. Hutsell. Relating the Hadamard Variance to MCS Kalman Filter Clock Estimation. In *Proceedings of the 27th Annual Precise Time and Time Interval (PTTI) Applications and Planning Meeting*, pages 291–301, 1996.

IGS Real Time Pilot Project. IGS Real Time Pilot Project. published online, 2009. URL http://www.rtigs.net/pilot. last accessed November 2009.

IGS Real Time Working Group. IGS Real Time Working Group Message Protocol. published online, 2009. URL http://www.rtigs.net/protocol.php. last accessed August 2009.

International Earth Rotation and Reference Systems Service. SINEX - Solution (Software/technique) INdependent EXchange Format Version 2.02 (December 01, 2006). published online, 2009. URL http://www.iers.org/documents/ac/sinex/sinex_v202.pdf. last accessed July 2009.

International GNSS Service. IGS Products. published online, 2009. URL http://igscb.jpl.nasa.gov/components/prods.html. last accessed July 2009.

IS-QZSS. *Interface Specification for QZSS (IS-QZSS)*. Japan Aerospace Exploration Agency, version 1.1 edition, July 2009.

JPL. Orbiter and Radio Metric Systems Group: Real-Time GIPSY Software. published online, 2010. URL http://gipsy.jpl.nasa.gov/orms/rtg/index.html. last accessed February 2010.

E. D. Kaplan. *Understanding GPS, Principles and Applications (Second Edition)*. Artech House, Norwood, MA 02062, 2006.

M.O. Kechine, C.C.J.M Tiberius, and H. van der Marel. Real-time Kinematic Positioning with NASA's Global Differential GPS System. In *Proceedings of the GNSS Conference, St. Petersburg, Russia*, May 2004.

J. Kouba. Relativistic Time Transformations in GPS. *GPS Solutions*, 5(4):1–9, 2002.

J. Kouba. A Guide To Using International GNSS Service (IGS) Products. published online, May 2009. URL http://acc.igs.org/UsingIGSProdcutsVer21.pdf. last accessed January 2010.

R. B. Langley. Navstar GPS Constellation Status (09-11-11). published online, 2009. URL http://gge.unb.ca/Resources/GPSConstellationStatus.txt. last accessed December 2009.

R. F. Leandro, M. C. Santos, and R. B. Langley. UNB Neutral Atmospheric Models: Developement and Performance. In *Proceedings of the ION NTM 2006, the National Technical Meeting of The Institute of Navigation*, pages 564–573, Monterey, California, January 18th-20th 2006.

R. Lutwak, D. Emmons, R. M. Garvey, and P. Vlitas. Optically Pumped Cesium-beam Frequency Standard for GPSIII. In *Proceedings of the 33rd Annual Precise Time and Time Interval (PTTI) Applications and Planning Meeting*, 2002.

H. Martin. GPS Status and Modernization. presented at Munich Satellite Navigation Summmit 2008, Munich, Germany, 2008.

D. D. McCarthy and G. Petit. *IERS Technical Note No. 32 (2003)*. Verlag des Bundesamts für Kartographie und Geodäsie, Frankfurt am Main, 2004.

P. Misra and P. Enge. *Global Positioning System Signals, Measurements, and Performance*. Ganga-Jamuna Press, Lincoln, Massachussets 01773, 2001.

O. Montenbruck and A. Hauschild. Characterization of the CONGO Sensor Stations. Technical Note TN 10-05, DLR-GSOC, March 2010.

O. Montenbruck and P. Ramos-Bosch. Precision Real-Time Navigation of LEO Satellites using Global Positioning System Measurements. *GPS Solutions*, 12(3):187–198, 2008. doi: 10.1007/s10291-007-0080-x.

O. Montenbruck, E. Gill, and R. Kroes. Rapid orbit determination of LEO satellites using IGS clock and ephemeris products. *GPS Solutions*, (9):226–235, 2005a.

O. Montenbruck, T. van Helleputte, R. Kroes, and E. Gill. Reduced dynamic orbit determination using GPS code and carrier measurements. *Aerospace Science and Technology*, 9(3):261–271, 2005b. doi: 10.1016/j.ast.2005.01.003.

O. Montenbruck, Y. Yoon, E. Gill, and M. Garcia-Fernandez. Precise Orbit Determination for the TerraSAR-X Mission. In *Proceedings of the 19th International Symposium on Space Flight Dynamics*, Kanazawa, Japan, June 2006.

O. Montenbruck, M. Garcia-Fernandez, Y. Yoon, S. Schön, and A. Jäggi. Antenna phase center calibration for precise positioning of LEO satellites. *GPS Solutions*, 13 (1):23–34, 2009a. doi: 10.1007/s10291-008-0094-z.

O. Montenbruck, A. Hauschild, U. Hessels, P. Steigenberger, and U. Hugentobler. CONGO - First GPS/GIOVE Tracking Network for Science, Research. *GPS World*, pages 36–41, September 2009b.

S. Montenegro and J. Richardson. RODOS operating system for Network Centric Core Avionics. In *Proceedings of Conference on Advances in Satellite and Space Communications*, Colmar, France, July 2009.

R. J. Muellerschoen, W. I. Bertiger, M. F. Lough, D. Stowers, and D. Dong. An Internet-Based Global Differential GPS System, Initial Results. In *Proceedings of the ION National Technical Meeting*, Anaheim, CA, USA, January 2000.

P. J. Neirinchx. Autonomous Onboard Guidance and Navigation Performance for Earth to Mars Transfer Mission. Master's thesis, Department of Aeronoutics and Astronautics, Massachusetts Institute of Technology, 1992.

A. E. Niell. Global Mapping Functions for the Atmosphere Delay of Radio Wavelengths. In *Journal of Geophysical Research*, volume 101, pages 3227–3246, 1996.

J. Petzinger, R. Reith, and T. Dass. Enhancements to the GPS Block IIR Timekeeping System. In *Proceedings of the 34th Annual Precise Time and Time Interval (PTTI) Applications and Planning Meeting*, pages 291–301, 2002.

R. Píriz, M. Cueto, V. Fernández, P. Tavella, I. Sesia, G. Cerretto, and J. Hahn. GPS/GALILEO Interoperability: GGTO, Timing Biases and GIOVE-A Experience. In *Proceedings of the 38th Annual Precise Time and Time Interval (PTTI) Applications and Planning Meeting*, 2006.

J. Ray and J. Griffiths. Status of IGS Ultra-Rapid Products for Real-Time Applications. 2008.

G. J. Robertson, R. Kieffer, M. Malik, G. Gatti, V. Alpe, and M. Johansson. GIOVE-B Satellite Design and Performance Validation. In *Proceedings of the ION GNSS 2009*, Savannah, GA, USA, September 2009.

C. Rocken, Y.-H. Kuo, W. Schreiner, D. Hunt, S. Sokolovskiy, and C. McCormick. COSMIC System Description. *Special issue of Terrestrial, Atmospheric and Oceanic Science*, 11(1):21–52, 2000.

RTCM. *RTCM 10402.3 RECOMMENDED STANDARDS FOR DIFFERENTIAL GNSS (GLOBAL NAVIGATION SATELLITE SYSTEMS) SERVICE VERSION 2.3*. Radio Technical Commission For Maritime Services, 1800 Diagonal Road, Suite 600, Alexandria, Virginia 22314-2840 USA, August 20th 2001.

RTCM. *RTCM STANDARD 10403.1 FOR DIFFERENTIAL GNSS (GLOBAL NAVIGATION SATELLITE SYSTEMS) SERVICES VERSION 3*. Radio Technical Commission For Maritime Services, 1800 N. Kent St., Suite 1060, Arlington, Virginia 22209, USA, October 27th 2006.

RTCM. *Version 3 Proposed Messages Set 9*. Radio Technical Commission For Maritime Services, 1800 N. Kent St., Suite 1060, Arlington, Virginia 22209, USA, January 10th 2009.

S. Schaer and P. Steigenberger. Determination and Use of GPS Differential Code Bias Values. presented at IGS Workshop 2006, Darmstadt, Germany, 2006.

R. Schmid, P. Steigenberger, G. Gendt, M. Ge, and M. Rothacher. Generation of a consistent absolute phase center correction model for GPS receiver and satellite antennas. *Journal of Geodesy*, 81(12):781–798, 2007.

A. Simsky and J.-M. Sleewaegen. C/A pseudoranges anomaly in geodetic-grade receivers. In *Proceedings of the GNSS 2004*, Rotterdam, NL, May 16-19 2004.

W.L. Smith. Note on the relationship between total precipitable water and surface dew point. *Journal of Applied Meteorology*, 5:726–727, October 1966.

Surrey Satellite Technology Ltd. GIOVE-A In-Orbit Review and Status. presented at the ESTEC GIOVE Workshop 2008, 2008.

U.S. Coast Guard Navigation Center. GPS Constellation Active NANU Status. published online, 2009. URL www.navcen.uscg.gov/navinfo/Gps/ActiveNanu.aspx. last accessed January 2009.

USNO. CURRENT GPS CONSTELLATION. published online, 2009. URL http://tycho.usno.navy.mil/gpscurr.html. last accessed December 2009.

T. van Baak. Allan deviation and averaging. published online, August 2009. URL http://www.leapsecond.com/pages/adev-avg/.

P. Waller, F. Gonzalez, J. Hahn, S. Binda, R. Piriz, I. Hidalgo, G. Tobias, I. Sesia, and P. Tavella. In-Orbit Performance Assessment of GIOVE Clocks. In *Proceedings of the ION GNSS*, Savannah, GA, USA, September 2009.

R. Ware, M. Exner, D. Feng, M. Gorbunov, K. Hardy, B. Herman, Y. Kuo, T. Meehan, W. Melbourne, C. Rocken, W. Schreiner, S. Sokolovskiy, F. Solheim, X. Zou, R. Anthes, S. Businger, and K. Trenberth. GPS sounding of the atmosphere from low earth orbit: Preliminary results. *Bulletin of the American Meteorological Society*, 77: 19–40, January 1996.

D.L.M. Warren and J.F. Raquet. Broadcast vs. Precise GPS Ephemerides: A Historical Perspective. *GPS Solutions*, 7, 2003.

G. Weber, D. Dettmering, and H. Gebhard. Networked Transport of RTCM via Internet Protocol (NTRIP). In F. Sanso, editor, *A Window on the Future, Proceedings of the IAG General Assembly, Sapporo, Japan, 2003, Springer Verlag, Symposia Series*, volume 128, pages 60–64, 2005.

G. Weber, L. Mervart, and J. Dousa. Real-time Clock and Orbit Corrections for Improved Point Positioning via NTRIP. In *Proceedings of the ION GNSS*, Fort Worth, TX, USA, 2007.

M. Wermuth, A. Hauschild, O. Montenbruck, and A. Jggi. TerraSAR-X Rapid and Precise Orbit Determination. In *Proceedings of the 21st International Symposium on Space Flight Dynamics, 28 Sep. - 2 Oct. 2009*, Toulouse, France, 2009.

J. Wickert, G. Beyerle, C. Falck, S. Heise, R. Knig, G. Michalak, D. Pingel, M. Rothacher, T. Schmid, and C. Viehweg. GPS radio occultation with CHAMP, GRACE-A, TerraSAR-X and COSMIC: Brief review of results from GFZ. presented at 3rd International Workshop on Occultations for Probing Atmosphere and Climate September 17th-21st 2007, Graz, Austria, 2007.

A. Wu and B. Feess. Developement and Evaluation of GPS Space Clocks for GPSIII and Beyond. In *Proceedings of the 32th Annual Precise Time and Time Interval (PTTI) Applications and Planning Meeting*, 1999.

J.T. Wu, S.C. Wu, and G.A. Hajj. Effects of Antenna Orientation on GPS Carrier Phase. *Manuscripta Geodaetica*, 18:9198, 1993.

G. Wübbena. GNSS Network-RTK Today and in the Future, Concepts and RTCM Standards. In *Proceedings of the International Symposium on GNSS, Space-based and Ground-based Augmentation Systems and Applications*, Berlin, Germany, November 11-14 2008.

G. Xu and P. Knudsen. Earth Tide Effects on Kinematic/Static GPS Positioning in Denmark and Greenland. *Phys. Chem. Earth (A)*, 25(4):409–414, 2000. doi: 1464-1895/00/$.

T. P. Yunck, G. F. Lindal, and C. H. Liu. The Role of GPS in Precise Earth Observation. In *Proceedings of the IEEE Position Location and Navigation Symposium 1988*, pages 251–258, Orlando, Fl., USA, 1988.

R. Zandbergen and D. Navarro. Specification of Galileo and GIOVE Space Segment Properties Relevant for Satellite Laser Ranging. Technical Note ESA-EUING-TN/10206, Issue 3.2, Galileo Project Office, ESTEC, ESA, 2008.

R. Zandbergen, A. Ballereau, E. Rojo, Y. Andres, I. Romero, C. Garcia, and J. M. Dow. GRAS GSN near-real time data processing. presented at IGS Workshop 2006, Darmstadt, Germany, 2006.

Acknowledgments

This thesis would have not been possible without the support of many individuals. First of all, I would like to express my gratitude to Oliver Montenbruck, who provided the opportunity to pursue my Ph. D. studies at DLR/GSOC under his supervision. The support which I have received in so many ways over the entire time was beyond doubt outstanding. Furthermore, I would like to thank Urs Hugentobler for being the doctoral advisor at TUM and for providing valuable inputs for the thesis. Many thanks also to Richard B. Langley for serving as an examiner.

I am grateful to the IGS real-time pilot project for the access to the data-streams of the real-time network. I would especially like to thank Georg Weber from BKG for many fruitful discussions and for providing the caster for the real-time data streams from the CONGO network. John Dow, Loukis Agrotis and Pedro Alfaro from the analysis center coordination team at ESOC provided the data for the inter-agency comparisons of the real-time project, which is greatly appreciated.

I want to thank all station hosts of the CONGO network around the world for their support of our GIOVE tracking activities. Furthermore, I would like to thank Peter Steigenberger from TUM for the hard work that went into the GIOVE orbit determination and for providing his GIOVE orbit predictions as basis for the real-time clock estimation. I am also grateful to Martin Wermuth from DLR/GSOC for providing GPS measurements from the TerraSAR-X mission. The CODE analysis center and the ILRS provided precise GPS products and laser ranging measurements, respectivley.

Last but not least, I am grateful to my parents and my girlfriend Mareike for providing support and motivation, especially in the difficult phases.